

ULTRASONIC TOMOGRAPHY FOR DETECTING AND LOCATING DEFECTS IN  
CONCRETE STRUCTURES

A Thesis

by

JOSHUA BENJAMIN WHITE

Submitted to the Office of Graduate Studies of  
Texas A&M University  
in partial fulfillment of the requirements for the degree of  
MASTER OF SCIENCE

May 2012

Major Subject: Civil Engineering

ULTRASONIC TOMOGRAPHY FOR DETECTING AND LOCATING DEFECTS IN  
CONCRETE STRUCTURES

A Thesis

by

JOSHUA BENJAMIN WHITE

Submitted to the Office of Graduate Studies of  
Texas A&M University  
in partial fulfillment of the requirements for the degree of

MASTER OF SCIENCE

Approved by:

Chair of Committee,	Stefan Hurlbaas
Committee Members,	Dan Zollinger
	Gary Gaukler
Head of Department,	John Niedzwecki

May 2012

Major Subject: Civil Engineering

## ABSTRACT

Ultrasonic Tomography for Detecting and Locating Defects in Concrete Structures.

(May 2012)

Joshua Benjamin White, B.S., Abilene Christian University

Chair of Advisory Committee: Dr. Stefan Hurlebaus

This thesis evaluates a particular ultrasonic nondestructive testing (NDT) system in order to determine its capabilities and limitations in locating defects in concrete structures; specifically tunnel linings, bridge decks, and pavements. The device, a phased-array ultrasonic tomography (UST) system that utilizes shear waves, is a significant advancement in NDT systems. Consequently, there is a need in structural engineering to verify new technologies by assessing their flaw-detecting capabilities in a variety of structural applications.

The UST technique does not currently have a testing methodology that is field-ready. In order to develop a methodology, the system was evaluated based on its ability to detect simulated defects, then taken to the field to evaluate natural structural defects on public tunnels, pavements, and airport runways. Types of concrete defects the system is used to detect and localize include air- and water-filled voids, vertical cracks, horizontal delaminations, and abnormalities such as clay lumps. The device is also used to determine reinforcement depth and spacing as well as concrete thickness measurements.

This research concludes that the UST system is exceptional at locating horizontal delaminations ranging from 0.05-2.0 mm (0.002-0.079 in.), and is able to differentiate between fully debonded and partially-bonded areas. Vertical cracks could only be detected once they begin to form parallel to the testing surface; however, omission of surface details was found to be a strong indicator of crack presence. Backwall surfaces up to a depth of 762 mm (30 in.) were successfully and accurately determined. Air- and water-filled voids as well as reinforcement details such as layout and depth were also successfully determined and located. With the exception of some medium-sized clay lumps (with a diameter of approximately 102 mm, or 4 in.) surrounding reinforcement, all clay lumps tested were also highly successful.

DEDICATION

To my dear Grandma Ruth

## ACKNOWLEDGEMENTS

I would like to thank my committee chair, Dr. Stefan Hurlebaus, and my committee members, Dr. Dan Zollinger and Dr. Gary Gaukler, for their guidance and support throughout the course of this research.

I would also like to extend my gratitude to Dr. Monica Starnes and the Strategic Highway Research Program 2 (SHRP2) Project R06G for making this research possible. Special thanks to Dr. Andrew Wimsatt and the members of the SHRP2 R06G committee for their endless support and advice. Without the assistance of Dr. Wimsatt, Dr. Hurlebaus, and Dr. Zollinger, all evaluations performed across the U.S. could not have taken place. I would also like to thank Dr. Soheil Nazarian and the University of Texas at El Paso for allowing us to perform tests on their simulated bridge deck, as well as Mr. Tom Scullion for allowing us to evaluate some of his concrete specimens. Thanks also to my friends and colleagues and the department faculty and staff for making my time at Texas A&M University a great experience.

Finally, thanks to all of my family for their encouragement and to my darling wife, Amy, for her endless patience and love.

## TABLE OF CONTENTS

	Page
ABSTRACT .....	iii
DEDICATION .....	v
ACKNOWLEDGEMENTS .....	vi
TABLE OF CONTENTS .....	vii
LIST OF FIGURES.....	ix
LIST OF TABLES .....	xiii
1. INTRODUCTION .....	1
1.1 Problem Statement .....	1
1.2 Research Objectives .....	3
1.3 Thesis Organization.....	4
1.4 Summary of Findings.....	6
2. BACKGROUND.....	8
2.1 A Brief History of Ultrasonics in NDT .....	8
2.2 Development of Phased-Array UST with SAFT Algorithm.....	10
3. EVALUATION OF THE ULTRASONIC TOMOGRAPHY SYSTEM ON SIMULATED SPECIMENS.....	14
3.1 Fabrication, Testing, and Validation of Concrete/Shotcrete Specimens with Simulated Delaminations and Voids.....	14
3.2 Fabrication, Testing, and Validation of Concrete Specimens with Simulated Clay Lumps .....	20
3.3 Fabrication, Testing, and Validation of Concrete Bridge Deck with Simulated Defects .....	24
3.4 Reliability Assessment for Simulated Defect Evaluation using UST ..	35
3.5 Summary of Simulated Defect Evaluation using UST.....	36
4. EVALUATION OF THE ULTRASONIC TOMOGRAPHY SYSTEM IN THE FIELD.....	41

	Page
4.1 Eisenhower Memorial Tunnel, CO .....	41
4.2 Hanging Lake Tunnel, CO .....	47
4.3 Chesapeake Channel Tunnel, VA .....	54
4.4 Washburn Tunnel, TX.....	69
4.5 CRCP on Interstate 20 in Ft. Worth, TX.....	73
4.6 George Bush Intercontinental Airport, Houston, TX.....	78
5. DEVELOPMENT OF A METHODOLOGY FOR THE UST SYSTEM .....	83
5.1 Methodology Needs .....	83
5.2 Addressing the Needs for Operating in Map and Review Modes.....	85
5.3 General Testing Procedures .....	95
6. CONCLUSIONS AND RECOMMENDATIONS.....	99
6.1 Conclusions .....	99
6.2 Limitations of the UST System.....	99
6.3 Recommendations for Future Research .....	102
REFERENCES.....	105
APPENDIX A .....	108
APPENDIX B .....	117
VITA .....	174



## LIST OF FIGURES

	Page
Figure 1 The A1040 MIRA system and the transmission/reception of acoustic waves and corresponding echo intensity .....	11
Figure 2 B-scan, C-scan, and D-scan relative to the tomograph .....	12
Figure 3 Construction of slabs with simulated defects. ....	15
Figure 4 Scale of reflectivity .....	17
Figure 5 Typical C-scans for simulated defects in concrete slabs: Specimens Theta, Lambda, Kappa, and Gamma .....	18
Figure 6 Typical C-scans for simulated defects in shotcrete slabs: Specimens D, E, I, and M .....	19
Figure 7 Clay lump slab construction .....	22
Figure 8 Large clay lump slabs: without reinforcement and with reinforcement .	23
Figure 9 Medium clay lump slabs: without reinforcement and with reinforcement .....	24
Figure 10 Simulated bridge deck at UTEP in El Paso, TX .....	25
Figure 11 Layout of constructed bridge deck .....	26
Figure 12 C-scan at 2.5" depth: construction key and UST results .....	29
Figure 13 C-scan at 6" depth: construction key and UST results .....	30
Figure 14 B-scan showing CK 1: construction key and UST results .....	31
Figure 15 B-scan showing DL 1 and 4: construction key and UST results .....	31
Figure 16 B-scan showing DL 2: construction key and UST results .....	31
Figure 17 B-scan showing DL 7, 3, and 5: construction key and UST results .....	31

	Page
Figure 18 B-scan showing DL 6: construction key and UST results .....	32
Figure 19 B-scan showing DL 8: construction key and UST results .....	32
Figure 20 B-scan showing CR 1: construction key and UST results .....	32
Figure 21 Infrared collage and single image from camera of the simulated bridge deck. ....	33
Figure 22 GPR data indicating four areas of delamination within the top reinforcement .....	37
Figure 23 $R^2$ for various defect detection parameters in the concrete/shotcrete slabs.....	39
Figure 24 Eisenhower Memorial Tunnel, CO .....	41
Figure 25 Eisenhower Tunnel testing area within the plenum: the interior precast divider wall and the exterior tunnel lining .....	42
Figure 26 Scanned areas within Eisenhower Tunnel: “sound” concrete, surface cracking and crazing near joint, and surface cracking and crazing near joint and crack with stalactite formation .....	43
Figure 27 UST images of “sound” area: B-scan, C-scan, and Volume-scan.....	44
Figure 28 UST images of surface cracking/crazing area: B-scan, C-scans, and Volume-scan.....	45
Figure 29 UST images of surface cracking/crazing area near stalactite formation: B-scan and Volume-scan.....	45
Figure 30 B-scan of precast divider panel showing backwall reflection and reinforcement .....	46
Figure 31 Hanging Lake Tunnel: exterior and interior view .....	48
Figure 32 Images of areas tested at Hanging Lake Tunnel: severe vertical cracks, sound concrete, and lining joint .....	48
Figure 33 Image collage of extensive map with cracks.....	49

	Page
Figure 34 Image of tile surface that was evaluated .....	49
Figure 35 UST images showing surface cracks and delamination: B-scans and Volume-scan.....	50
Figure 36 UST images showing possible deep delamination: B-scans and Volume-scan.....	51
Figure 37 UST images showing significant deep delamination: Volume-scan, B-scan, and C-scans .....	53
Figure 38 UST images over lining joint: B-scan and Volume-scan .....	54
Figure 39 Chesapeake Channel Tunnel: exterior and interior view .....	55
Figure 40 Areas tested at Chesapeake Bay Tunnel.....	57
Figure 41 Comparison of steel layout differences .....	58
Figure 42 Typical spalling and corrosion .....	59
Figure 43 Area surrounding “live” crack.....	59
Figure 44 UST images at STA. 481+76 showing deep delamination .....	60
Figure 45 UST images surrounding circumferential crack.....	62
Figure 46 Images depicting Region I and Region II.....	64
Figure 47 Region I UST images .....	65
Figure 48 Region II UST images.....	65
Figure 49 Tile lining sections in Chesapeake Bay Tunnel .....	66
Figure 50 First tile lining area tested, discovered by SPACETEC scanning.....	67
Figure 51 Second tile lining area tested.....	68
Figure 52 Washburn Tunnel: exterior and interior view .....	69
Figure 53 Tile linings via UST paired with the associated C-scans .....	70

	Page
Figure 54 Area tested surrounding debonded tiled: B-scans, C-scans, and Volume-scans .....	72
Figure 55 Tile lining tested at Washburn Tunnel .....	73
Figure 56 I-20 in Ft. Worth, TX .....	74
Figure 57 Four areas tested on I-20 in Ft. Worth, TX .....	75
Figure 58 Typical UST results for I-20 scanning .....	75
Figure 59 UST C-scans overlaid on I-20 images: Section A, Section B, Section C, and Section D.....	76
Figure 60 Airport runway at IAH .....	79
Figure 61 First segment tested at IAH: B-scans, Volume-scan, and C-scan.....	80
Figure 62 Second segment tested at IAH: B-scans, Volume-scan, and C-scans.....	81
Figure 63 Gridlines using grid template .....	91

## LIST OF TABLES

	Page
Table 1 Summary of concrete/shotcrete slab specimens with simulated defects...	21
Table 2 Summary of simulated defects in the concrete bridge deck.....	27
Table 3 Section A, I-20 evaluations .....	77
Table 4 Section B, I-20 evaluations .....	77
Table 5 Section C, I-20 evaluations .....	78
Table 6 Section D, I-20 evaluations .....	78
Table 7 Recommended scanning directions and grid spacing.....	88
Table 8 Maximum and minimum detected features tested by the A1040 MIRA system.....	100

## 1. INTRODUCTION

### 1.1 Problem Statement

Systematic monitoring and assessment of concrete structures is imperative in order to maintain safe structures and keep costs of repair or replacement at a minimum. Structural evaluations, both destructive and nondestructive, are used for quality control and quality assurance purposes to locate defects or precursors to damage that will constrain the functionality of a structure. Unfortunately, defects are not typically noticed until they cause visible damage such as cracking and spalling. These observable “after-effects” are an indication that the structure has already possibly undergone significant loss of strength due to poor design, overload, or simply a result of other structural damage such as reinforcement corrosion (FHWA 2005). While the detection of these “after-effects” that are visible to the naked eye are critical for repair purposes and localization of damage, it falls on the NDT specialist to develop methods of inspection that can determine the beginning stages of such damage before it inhibits serviceability requirements, or worse, becomes a public safety issue (Elsener et al. 2003). When these early stages are identified before significant damage has taken place, preventive actions can be recommended that will arrest the development of further damage.

There are numerous methods for performing NDT analyses to structures. While

---

This thesis follows the style of the *Journal of Structural Engineering*.

the most predominant technique is visual inspection, studies show that inspection policies and practices can affect the reliability of visual inspections (FHWA 2001; IAEA 2002). Sustainable detection technologies that implement a reliability determination offer an enhancement to structural evaluations. It is therefore strongly encouraged that methodologies that are less subjective to interpretation be implemented from improved NDT systems. It is toward this end that researchers, engineers, and NDT specialists have attempted to design systems that make it easier for operators to discern problematic damage objectively and in a repeatable fashion. With this approach, reliability of inspection is less dependent on the subjective interpretation of the operator and more dependent on the accuracy and precision of the actual flaw-detection system. Development of such systems has led to the ultrasonic testing device used in this research.

With the advancements that have been made in ultrasonic measurement devices, numerous systems and methods have emerged. The ultrasonic technique, which encompasses all methods that employ the use of acoustic waves over 20 kHz, has shown a promising future for detecting internal defects. It has been shown to provide comprehensive detailing in concrete structures, including concrete thickness, internal duct locations, material layers, reinforcement presence, elastic modulus, cracks, voids, delamination, and corrosion (Krause et al. 1997; Schickert et al. 2003; Iyer et al. 2003; Im et al. 2010). Its primary disadvantage over other NDT methods has been the speed of data acquisition, due to the typical discrete point testing. However, with the developments of phased-array transducers, data acquisition has grown from single-point

evaluations to automated scanning of larger areas (Streicher et al. 2006; De La Haza et al. n.d.). The tomography system used in this proposed research belongs to this family of phased-array transducers, and represents an accumulation of the most recent developments in the ultrasonic NDT field.

Continual improvement of such NDT techniques and systems demands that newly developed technology be proven by field application. In particular, these systems must be evaluated by their performance on test specimens with controlled defects that accurately simulate realistic flaws, as well as real-life structural evaluations.

## **1.2 Research Objectives**

The first objective is to determine the capabilities and limitations of the phased-array ultrasonic tomography system. This is done by comprehensively evaluating specimens produced with known defects, as well as real-life structures, which include but are not limited to bridge decks, tunnel linings, and pavements. Where capable, the results are checked against data produced from other NDT techniques, including but not limited to ground penetrating radar (GPR), infrared thermography (IRT), and other acoustic sounding methods. After initial tests on specimens with simulated defects are performed, a reliability assessment of the device will be applied to the UST system. This will be done by determining the regression coefficient and standard errors of specific discontinuity qualities such as defect depth, width, and length. With this level of confidence established, the system will then be used on real-life structures and verified by ground truth data.



The second objective of this research is to develop a testing methodology for the ultrasonic tomography system. This includes methods for wave speed determination, device orientation, optimal grid alignment and spacing, scanning depth, creation of grids, establishment of boundary/origin and relationship to computer model, data processing, and validation with ground truth data.

The final objective is to provide recommendations for future study. This is done by taking into account the device's limitations, specifically addressing a potential breakthrough with the system: the speed of data acquisition.

### **1.3 Thesis Organization**

The following sections of this thesis work to answer the research objectives stated in the proposal. Section 2 briefly details the development of the ultrasonic technique and the recent breakthroughs leading up to the ultrasonic tomography system used in this research. Section 3 discusses the need to perform UST analyses on laboratory specimens with artificial flaws. This has two specific purposes: (1) to familiarize and develop critical interpretive skills for data collection techniques in field evaluations, and (2) to develop a reliability assessment of the system in its ability to detect simulated defects. The interpretive skills will be cultivated by incorporating blind testing; the researcher will collect data on a large number of specimens without knowledge of their contaminations. The specimens to be used in the blind evaluations will include 11 concrete slabs with simulated voids, air- and water-filled delaminations, natural cracks, and control specimens. Reinforcing steel will be placed in some of these slabs. Another specimen for blind testing will include a simulated concrete bridge deck

with a variety of delaminations (ranging from 0.3 mm [0.01 in.] to 2.0 mm [0.08 in.] thickness) at different heights (layered delaminations, above and below reinforcing steel), cracks (natural and simulated), and corroded reinforcement. After blind testing, comparisons with defect keys and consultation with personnel involved with the construction of the specimens will be used to evaluate the performance of the testing equipment. With the information gained from these evaluations, new specimens will be constructed with simulated voids and air- and water-filled delaminations. The specimens will be made from shotcrete construction, mimicking typical tunnel linings. The results of these evaluations will help solidify the ultrasonic tomography testing approach for the use in the interpretation of real-life structural evaluations. Other specimens with known defects that have been produced by researchers and engineers within the Texas A&M University System and Texas Transportation Institute are also available for evaluation, with defects such as clay lumps, voids, and various delaminations.

After all simulated specimens were tested, the UST system was used on real-life structures. Section 4 highlights the UST evaluations of these structural applications and compares the results with ground truth verification where able. This was done by performing ultrasonic tomography evaluations on many structures exhibiting typical damage. Specific structures that were available for the proposed research include but are not limited to: Washburn Tunnel in Pasadena, Texas; Eisenhower Memorial Tunnel near Dillon, Colorado; Hanging Lake Tunnel near Glenwood Springs, Colorado; Chesapeake Channel Tunnel near Norfolk, Virginia; select airport runways at George Bush Intercontinental Airport in Houston, Texas; and Interstate 20 pavement in Ft. Worth,

Texas. Evaluations at each of these locations are compared with ground truth data where available, as well as results from other NDT evaluations, including ground penetrating radar (GPR), infrared thermography (IRT), acoustic sounding methods (such as chain drag and hammer sounding), and automated versions of ultrasonic and electromagnetic radar.

Section 5 discusses the development of a testing methodology using the UST technique for concrete structure inspection, utilizing an efficient and strategic approach. This testing methodology capitalizes on all the information gained from the UST evaluations performed on specimens with simulated defects and real-life structures alike. Ultimately, this provides the scientific community with a promising methodology that emphasizes the advantages of the UST system, and provides awareness of the system's limitations.

Section 6 outlines the limitations of the UST system and makes recommendations for future study. This section will revisit the inefficiencies of the UST system and propose recommendations for future research based on those inefficiencies and the limited scope of this research.

#### **1.4 Summary of Findings**

The UST system was used to perform evaluations on over 30 concrete and shotcrete specimens containing simulated defects. These defects included air- and water-filled voids, vertical cracks, horizontal delaminations, and abnormalities such as clay lumps. The device was also used to determine specimen characteristics such as reinforcement depth and spacing, as well as concrete thickness measurements. The

system's capabilities were evaluated, and after establishing reliability for various types of defects, the system was used on over six existing public structures, including tunnels, highway pavements, and airport runways. Where able, ground truth verification was further used to determine the accuracy of the system.

This research concludes that the UST device is exceptional at locating horizontal delaminations; and is able to differentiate between fully debonded and partially bonded areas. Vertical cracks could only be detected once they begin to form parallel to the testing surface; however, omission of surface details was found to be a strong indicator of crack presence. Backwall surfaces, up to a depth of 762 mm (30 in.), were successfully and accurately determined. Air- and water-filled voids could be detected and were distinguishable by looking for "shadowing effects" under the defect. Reinforcement details such as layout and depth were also successfully determined, with the exception of some shotcrete applications. With the exception of some medium-sized clay lumps (with a diameter of approximately 102 mm, or 4 in.) surrounding reinforcement, all clay lumps tested were also highly successful.

## 2. BACKGROUND

### 2.1 A Brief History of Ultrasonics in NDT

All methods of noninvasive testing involve the excitation of some sort of wave and the reception of that wave after it has interfered with the object of its inspection. This is true for one of the oldest NDT techniques, the sounding inspection, as the human ear perceives the changes in intensity amplitude of reflected acoustic pulses excited by a point impact such as a coin; as well as the modern technological usages of thermal imaging in which temperature differentials due to the internal composition of a material, are discerned by sensors within the thermal camera that detect the emission of electromagnetic waves with different energy amplitudes. This oversimplification of hundreds of years of research is intended to direct thought to a particular point: the better scientists and engineers understand the complex characteristics and behavior of wave motion, be it acoustic or electromagnetic radiation, and its interaction with inspection mediums, systems can be developed and optimized that accurately evaluate structural components.

With this premise, Sergei Sokolov, a Soviet scientist often referred to as the father of ultrasonic testing, worked on the development of NDT inspection of steel structures using ultrasonic echograms. The proposal was a simple thought: if it were possible to generate ultrasonic pulses in a test subject and then capture the reflection of the pulse after it encountered physical properties within the material, then it would be possible to gain information on the integrity and physical characteristics of the tested

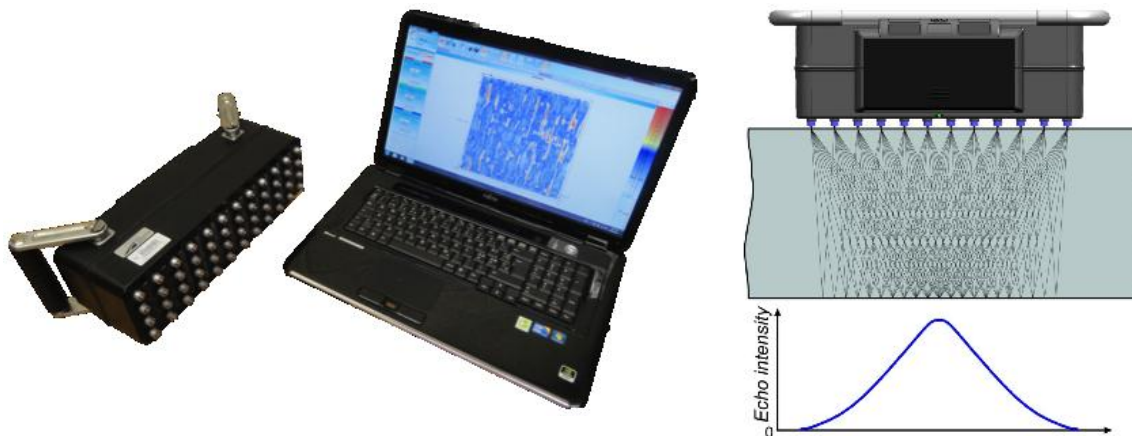
material. In 1928, Sokolov proposed that ultrasonic stress waves could be used to detect flaws and abnormalities in steel (Sokolov 1929), but it was not until the late 1920s and early 1930s that he could prove his theory with experimental devices. However, due to the lack of advanced ultrasonic transducers, his method was cumbersome and the resolution was poor. Sokolov, as well as other scientists mostly working independently of each other, continued to develop the ultrasonic technique for flaw-detection, with the greatest successes being made primarily in the medical fields (Brennan 2007). Firestone, recognized as the first to introduce pulse-echo technology to the United States, patented his “Reflectoscope” in 1941 (Firestone 1946; Firestone 1942). The reflectoscope used a single source for emitting and receiving ultrasonic waves at 2.25 MHz. Utilizing a time-domain analysis, pulse reflections were used to determine discontinuities. During the same time, Donald Sproule in England developed a similar device that utilized two transducers, one for emitting the pulse and the other for receiving the reflection (Desch et al. 1946). Comparable to Sproule’s device, Adolf Trost in Germany invented the “Trost-Tonge”, which also used two transducers, located on opposite sides of the object in question, with continuously flowing water used as a coupling agent (Woo 2006). This through-transmission technique permitted discontinuities and material degradation to be investigated.

The ever-improving ultrasonic techniques that were developed by researchers interested in structural inspection were primarily used for steel members. Around the 1950s, researchers began to turn their attention to the inspection of concrete structures, which posed a new set of problems. Unlike steel, concrete is a heterogeneous material,

as it is comprised of non-uniform and randomly-oriented bulky aggregates bound together by cement paste. Stress waves introduced into concrete quickly attenuate due to inconsistencies within the material, making the reception of these waves difficult. Two changes in ultrasonic testing helped to overcome signal loss in concrete: the use of lower ultrasonic frequencies which are less prone to attenuation, and the use of shear waves (*Secondary waves*, or S-waves) rather than the traditional use of longitudinal waves (*Primary waves*, or P-waves). S-waves, also called transverse waves, travel at approximately 62% the speed of P-waves in concrete, and as their name implies, have a transverse waveform that makes them less susceptible to structural noise.

## **2.2 Development of Phased-Array UST with SAFT Algorithm**

Until the 1980s, all ultrasonic transducers required a couplant for transmitting stress waves into the object of inspection. The application of a coupling agent, typically a jelly, grease, or even water, makes the inspection process more tedious by elongating the time for transducer setup and data collection. In the 1980s, Acoustic Control Systems (ACS) in Moscow, Russia developed the dry point contact (DPC) transducer which consists of a piezoelectric crystal with a wear-proof ceramic tip that eliminates the use of a coupling agent. By the end of the 1990s, ACS had implemented this new technology in devices that could evaluate structures from only one side. Nearly a decade later, researchers at ACS working in collaboration with the Federal Institute of Materials Research and Testing in Berlin, Germany (BAM), developed the first ultrasonic tomography system that required no coupling agent (Acoustic Control Systems n.d.). The tomograph, a phased-array system shown in Fig. 1 (left), uses a 4 x 12 grid of

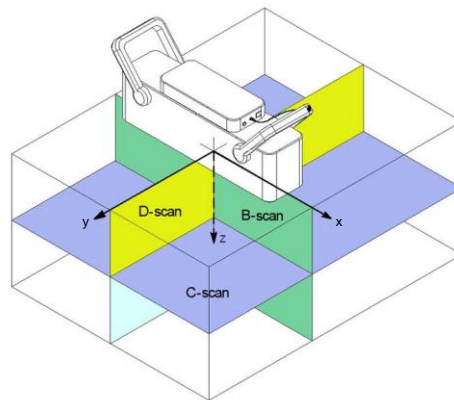


**Fig. 1. The A1040 M IRA system (left) and the transmission/reception of acoustic waves and corresponding echo intensity (right, from <http://www.pcte.com.au/concrete-non-destructive-testing-products/Defect-Location-Testing/MIRA--Pule-Echo-Ultrasonics.aspx>)**

mechanically isolated and dampened transducers that can fit the profile of a rough concrete testing surface with a variance of approximately 10 mm (0.4 in.). Each row of four transducers transmits stress waves sequentially while the remaining rows act as receivers. In this manner, there is a wide coverage of shear wave pulses that reflect at internal interfaces where the material impedance changes (Fig. 1, right). With the help of a digitally focused algorithm (an alteration of the Synthetic Aperture Focusing Technique, or *SAFT* [Schickert 1995]), a 3D volume is presented with each point of possible reflection in half-space represented by a color scheme, scaled according to reflecting power. This 3D image can also be dissected into each of the three planes representing its volume: the B-scan, C-scan, and D-scan (Fig. 2). The B-scan is an image slice showing the depth of the specimen on the vertical (or z) axis versus the width of scan on the horizontal (or x) axis. This slice is a plane perpendicular to the scanning surface and parallel with the length of the device. The C-scan is an image slice showing



the plan view of the tested area, with the vertical (or y) axis of the scan depicting width parallel to the scanning direction and the horizontal (or x) axis of the scan representing the length perpendicular to the scanning direction. Note that the scanning direction is always defined as the y-axis as seen in Fig. 2. The D-scan is like the B-scan in that it images a plane perpendicular to the testing surface, but it is oriented parallel to the



**Fig. 2. B-scan, C-scan, and D-scan relative to the tomograph**  
(<http://acsys.ru/eng/production>)

scanning direction. On each of the scans, the various intensities reported by the returned waves are color-coded from light blue to deep red, representing low reflectivity (typically sound concrete) and high reflectivity (any type of impedance), respectively. With this intensity scaling, it is easy to see any discontinuities with distinctly different wave speeds, such as voids, delaminations, cracks, and other abnormalities.

The UST system explored here has had limited exposure to industrial applications, but is fast in becoming recognized as a powerful NDT method. The

ultrasonic technique in general has been used in concrete structures to identify concrete thickness and elastic modulus, as well as detecting grouting conditions of internal ducts in prestressed structures (Im et al. 2010; De La Haza et al. n.d.). Previous uses of the ultrasonic tomograph technique have largely been conducted by BAM in Germany. BAM collaborated with ACS in the development of the MIRA system, and has shown successful detection of deep delamination at 203 mm, or 8 in., below the surface (Shokouhi et al. 2011). This study was conducted on a demolished bridge deck, and was limited to delaminations ranging from 76-203 mm (3-8 in.) in depth. This study also used a previous version of the UST device (with a 4 x 10 transducer array). Another study conducted by BAM indicated the UST technique could detect grouting conditions in post-tensioned concrete elements (Krause et al. 2009). Overall, the studies conducted by BAM have raised awareness of the abilities of the UST device and encourage more research discovering its capabilities and limitations.

### 3. EVALUATION OF THE ULTRASONIC TOMOGRAPHY SYSTEM ON SIMULATED SPECIMENS

A variety of testing conditions to validate this new technology is presented in this research. It is necessary to instill confidence in the engineer and owner of a structure of the ability of the UST technique to accurately detect and localize cracks, voids, delaminations, and other unwanted damage. Therefore, testing is carried out on a variety of structural applications including bridge decks, pavements, and tunnel linings. Types of targeted defects include air- and water-filled voids, vertical cracks, horizontal delaminations in various configurations, and abnormalities such as clay lumps. For the sake of completeness and a robust research approach, concrete depth and steel reinforcement is also evaluated.

The process used for the following evaluations was experimentally determined. It was necessary to experiment with scanning increments, grid locations, device orientations, and other types of configurations to help develop a reliable methodology. The evaluation procedure discussed in Section 6 reflects the insights gained from scanning the following simulated specimens.

#### **3.1 Fabrication, Testing, and Validation of Concrete/Shotcrete Specimens with Simulated Delaminations and Voids**

Eleven normal-weight concrete slabs and thirteen shotcrete slabs were constructed to mock various defects. The concrete slabs were used to mimic typical concrete pavements, bridge decks, and tunnel linings with and without reinforcing steel. The shotcrete slabs were constructed to mimic applications in which shotcrete is sprayed

on as a finished layer, as typically found in tunnel linings. A specially designed lattice girder, also typical in tunnel wall construction, was used as reinforcement in the shotcrete slabs (Fig. 3, bottom right).

The simulated delaminations in these slabs were constructed from three types of material. Delaminations were imitated by using 0.05 mm (0.002 in.) plastic square sheets and 0.25 mm (0.01 in.) cloth squares (Fig. 3, top right). Air-filled voids (Fig. 3, top left) were constructed by inserting 13 mm (0.5 in.) thick foam squares in vacuum-sealed plastic bags. Water-filled voids (Fig. 3, bottom left) were constructed in a similar manner by placing water-filled Ziploc bags within vacuum-sealed plastic bags and carefully padding the defect with concrete/shotcrete during construction so as not to puncture the plastic.

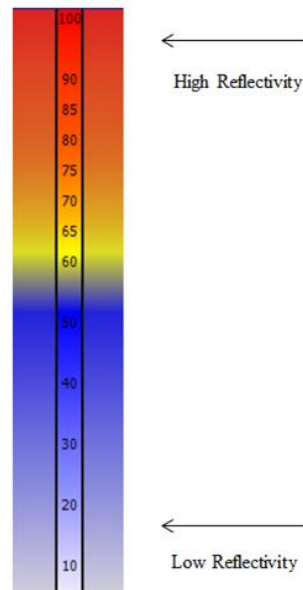


**Fig. 3. Construction of slabs with simulated defects**

The simulated specimens were tested by first placing a 50 mm x 150 mm (2 in. x 6 in. in  $y$ -increment vs.  $x$ -increment) grid on the surface. This grid increment was determined experimentally and is shown to provide optimal resolution for the types of defects under inspection in these slabs. After constructing the grid, the UST device is manually placed along each marked increment, taking 3-5 seconds per increment to automatically scan and store the gathered data. At the 50 mm x 150 mm (2 in. x 6 in.) spacing, this process takes approximately 13.5 minutes per square meter (1.25 minutes per square foot).

Some of these specimens were fully measured twice in opposing directions. This was done for two reasons. First, it is necessary to show the reproducibility of the ultrasonic tomography technique. Second, since the device is “polarized” in the sense that the shear waves are transmitted and received in one direction only (the  $x$ -axis), scanning in two orthogonal directions allows objects to be more accurately dimensioned.

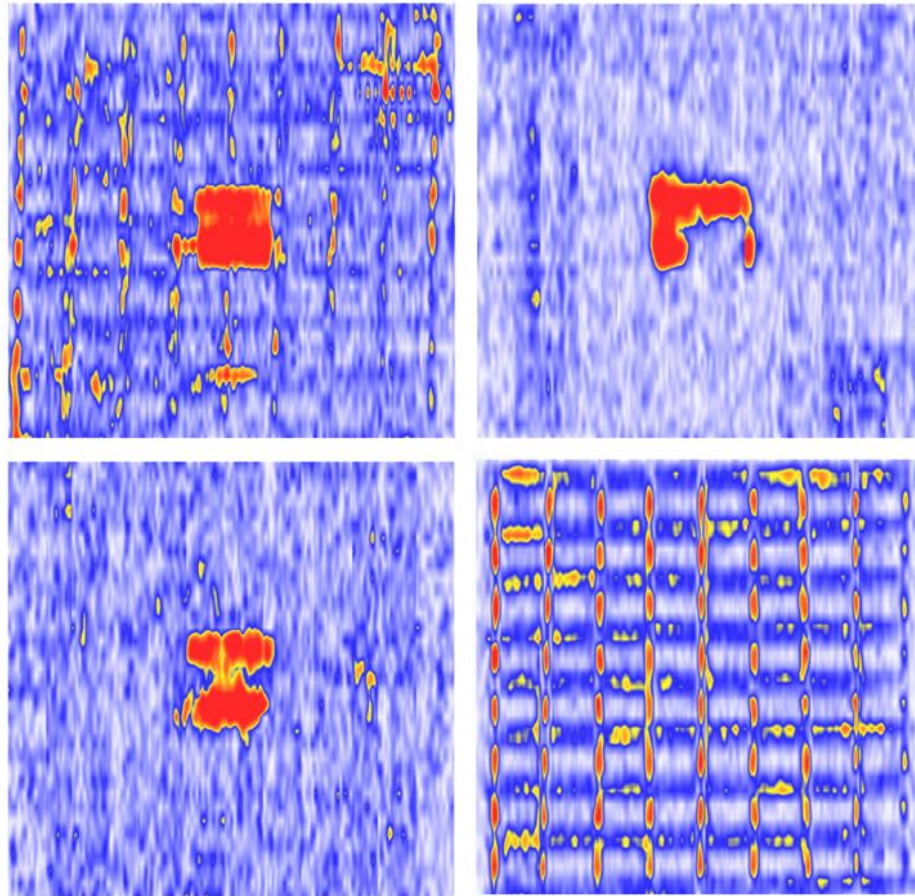
After constructing a grid on the specimens and gathering the data, the images produced by the A1040 MIRA proprietary software were analyzed for regions of high reflectivity, which are denoted by the red regions in the UST images. Since the software output is a color scheme that depicts intensity of reflectivity (low reflectivity or impedance is coded as light blue, while high reflectivity or impedance is coded as red, as shown in Fig. 4), great care has to be taken when determining the type of discontinuity under inspection. The software used in this research does not display a waveform in the time domain; therefore phase changes, which would be directly related to the density of the discontinuity, cannot be noticed. Also, since for these specimens the grid increment



**Fig. 4. Scale of reflectivity (or acoustic impedance)**

in the direction normal to the B-scans was 50 mm (2 in.), the B-scans in the inspection software are in 50 mm (2 in.) increments. This is because the ultrasonic system produces a B-scan image that is averaged between the four rows of transducers. The C- and D-scans, on the other hand, can be viewed in very small increments (on the order of 1-2 mm, or 0.04 – 0.08 in.) that are associated with the geometry of the transducer spacing and depth of scan.

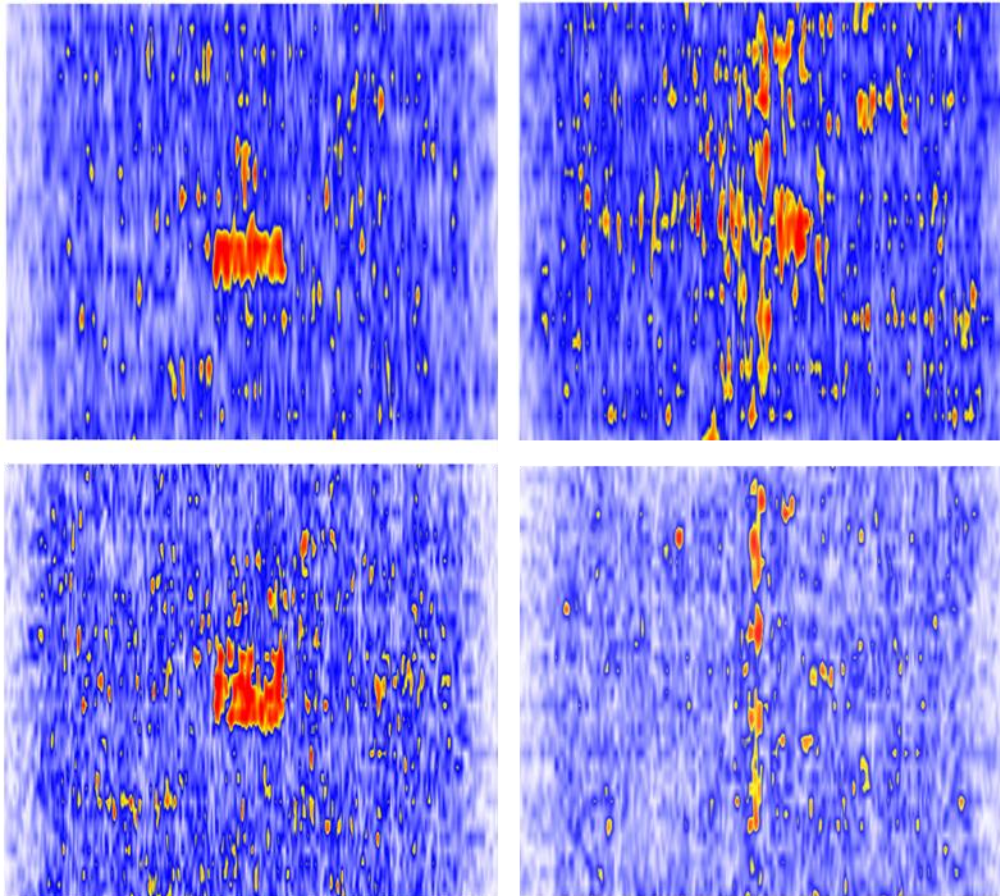
For most concrete structures, a backwall reflection is the first discontinuity that is expected to be readily visible, since backwall surfaces are usually exposed to air, causing almost complete reflection of the sound waves. This is not the case in instances where there is full bonding of a layer to a sublayer (see George Bush Intercontinental Airport results in Section 4.6). When a visible backwall reflection readily correlates with the expected concrete depth, inspection of the area between the testing surface and backwall



**Fig. 5. Typical C-scans for simulated defects in concrete slabs: Specimens Theta (top left), Lambda (top right), Kappa (bottom left), and Gamma (bottom right)**

reflection can take place. As each B-, C-, and D-scan is fully investigated, regions of high reflectivity that appear to be damage are catalogued by the judgment of the operator. If details such as concrete cover and reinforcement direction and spacing are desired, these can be catalogued as well.

C-scans, which offer the most comprehensive visual dimensioning of the simulated delaminations, are shown in Figs. 5 and 6. The images in these figures are representative of defect visualization for the simulated concrete and shotcrete slabs. Figs. 5 and 6 depict typical C-scans showing a simulated delamination (top left), an air-filled void (top



**Fig. 6. Typical C-scans for simulated defects in shotcrete slabs: Specimens D (top left), E (top right), I (bottom left), and M (bottom right)**

right), a water-filled void (bottom left), and a slab with only reinforcement (bottom right). A summary of all simulated defects and specimen characteristics for the concrete/shotcrete slabs with simulated defects (in addition to the simulated concrete specimens with clay lumps discussed in 3.2) is provided in Table 1. These images demonstrate that the discontinuities in normal-strength concrete are more clearly detectable than in the shotcrete specimens. One explanation is that the shotcrete application, perhaps when misapplied, can be more porous than typical concrete; within the shotcrete are numerous micro voids that more quickly attenuate the acoustic waves.



Even so, delaminations can still be detected. As will be seen in Section 4, when the system is applied in the field on shotcrete applications, the images are not significantly different than typical cast concrete.

### **3.2 Fabrication, Testing, and Validation of Concrete Specimens with Simulated Clay Lumps**

In addition to the concrete and shotcrete slabs, six concrete slabs were tested that were constructed in the 1990s by the Texas Transportation Institute as part of a previous research project. These slabs contain manufactured clay lumps of different diameters. The clay lumps are a high-plasticity clay, classified as Burleson Clay CH (AASHTO A-7-6) with a PI range of 35-45. The slabs and lumps are shown in Fig. 7, and are summarized in Table 1 (Specimens A2-F2). These six specimens consist of two sets of three slabs; one set with steel reinforcement and one set without. In each set, one slab was designated as the control with no clay lump contaminations. The remaining two had various levels of lumps of documented sizes corresponding to three regions of interest: 1) lumps below the reinforcement that represent typical lumps dense enough not to be quickly displaced towards the surface via vibration, 2) those that are caught in the reinforcing steel layer on their path towards the surface, and 3) those that are dispersed between the reinforcement and the top surface. The depth of the slabs is nominally 305 mm (12 in.), but all measurements are taken as approximate since no ground truth data was retrieved nor any accurate pictures taken to confidently support documented placement.

**Table 1. Summary of concrete/shotcrete slab specimens with simulated defects (Note: All slab specimens are nominally 1.83 m x 1.83 m)**

<b>SPECIMEN NAME</b>	<b>SPECIMEN DEPTH (mm)</b>	<b>MATERIAL</b>	<b>REINF. DETAIL</b>	<b>DEFECTS</b>	<b>TRUE DEPTH OF DEFECTS (mm)</b>	<b>UST DEPTH OF DEFECTS (mm)</b>
Alpha	305	Concrete	None	None	N/A	N/A
Beta	457	Concrete	* d= 127 mm	Natural crack	N/A	N/A
Gamma	305	Concrete	* d= 127 mm	None	N/A	N/A
Delta	610	Concrete	None	None	N/A	N/A
Epsilon	610	Concrete	* d= 127 mm	None	N/A	N/A
Zeta	381	Concrete	* d= 127 mm	None	N/A	N/A
Eta	381	Concrete	* d= 127 mm	0.05 mm thin plastic	51 from top	58 from top
Theta	381	Concrete	* d= 127 mm	0.05 mm thin plastic	76 from top	89 from top
Iota	381	Concrete	* d= 127 mm	0.05 mm thin plastic	25 from top	43 from top
Kappa	381	Concrete	* d= 127 mm	Air-filled void (13 mm foam)	203 from top	203 from top
Lambda	381	Concrete	* d= 127 mm	Water-filled void (Ziploc bag)	203 from top	196 from top
A	102	Shotcrete	None	None	N/A	N/A
B	152	Shotcrete	None	None	N/A	N/A
C	203	Shotcrete	None	None	N/A	N/A
D	305	Shotcrete	**	Air-filled void (13 mm foam)	193 from top	193 from top
E	305	Shotcrete	**	Water-filled void (Ziploc bag)	191 from top	193 from top
F	305	Shotcrete	**	Air-filled void (13 mm foam)	76 from top	89 from top
G	305	Shotcrete	**	Water-filled void (Ziploc bag)	76 from top	107 from top
H	305	Shotcrete	**	0.25 mm thin cloth	203 from top	183 from top
I	305	Shotcrete	**	0.25 mm thin cloth	102 from top	99 from top
J	305	Shotcrete	**	0.25 mm thin cloth	76 from top	74 from top
K	305	Shotcrete	**	0.25 mm thin cloth	51 from top	79 from top
L	305	Shotcrete	**	0.25 mm thin cloth	25 from top	<i>only shadow</i>
M	305	Shotcrete	**	None	N/A	N/A
A2	305	Concrete	* d= 152 mm	None	N/A	N/A
B2	305	Concrete	* d= 152 mm	Large (152 mm $\varnothing$ ) clay lumps	152 from top	160 from top
C2	305	Concrete	* d= 152 mm	Med. (102 mm $\varnothing$ ) clay lumps	76, 152, 229 from top	69, 137, 216 from top
D2	305	Concrete	* d= 152 mm	None	N/A	N/A
E2	305	Concrete	* d= 152 mm	Large (152 mm $\varnothing$ ) clay lumps	152 from top	107 from top
F2	305	Concrete	* d= 152 mm	Med. (102 mm $\varnothing$ ) clay lumps	76, 152, 229 from top	61, 137, 198 from top

\* Two mats of No. 5 Rebar, at depth “d” from top and bottom, 203 mm o.c.

\*\* One lattice girder in center of slab, sitting on bottom form

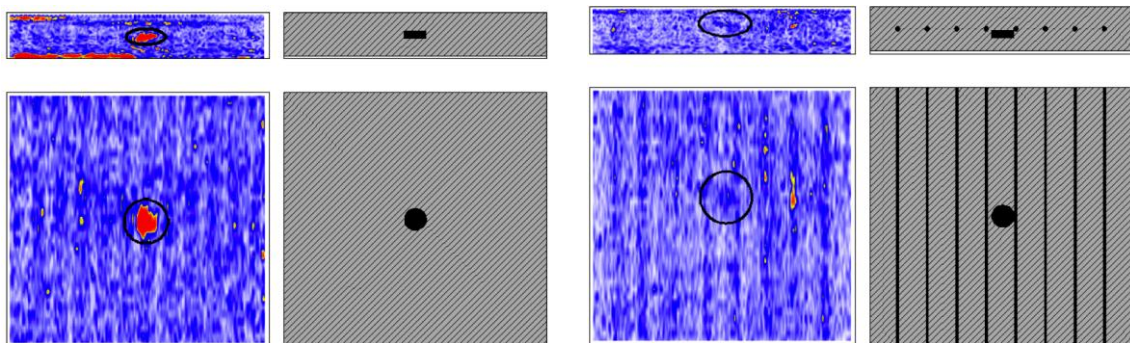


**Fig. 7. Clay lump slab construction**

Similar to the concrete and shotcrete slabs from Section 3.1, the simulated specimens were tested using a 50 mm x 150 mm (2 in. x 6 in.) scanning grid. Since the type of discontinuity under inspection was known beforehand, scanning only took place in one direction, although all of these specimens were fully scanned twice to judge repeatability. The scans took place in only one direction because the objects under inspection have a cross-sectional surface area (parallel to the scanning surface) greater than 50 mm (2 in.) in the  $y$ -scanning direction (more on the topic of device polarity and increment sizes can be found in Section 5). Repeatability was necessary in order to confirm the detection of each lump. In both sets of measurements taken for repeatability, the clay lumps found in all slabs were precisely in the same location, indicating remarkable repeatability.

It is important to note that the depths of the clay lumps were easily determined from either a single scanned image on the device screen, or a more detailed analysis on the computer model. This indicates that it is possible to assess the general condition of the structure both in the field and in the laboratory. Measurements to the centroid of high

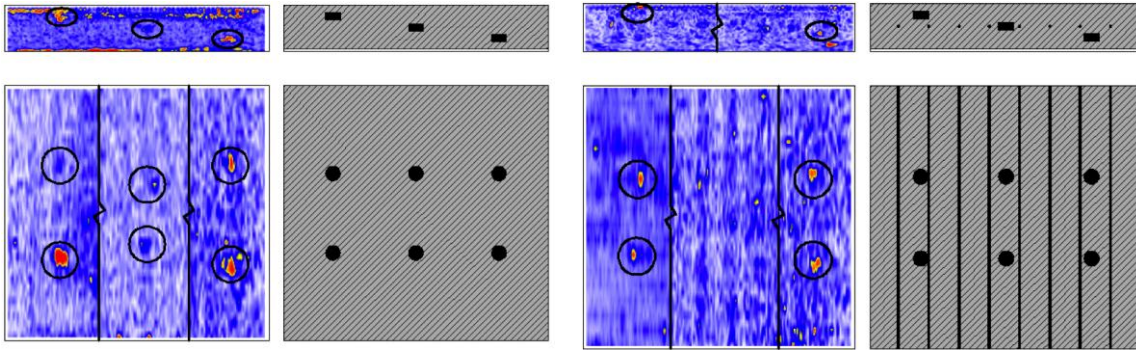
reflectivity regions, which denote any sort of discontinuity, represent the depth of these anomalies. Keys are provided alongside each ultrasonic image, Figs. 8 and 9, detailing the *intended* location of the lumps. It should be understood that during concrete pouring and vibrating, the lumps will inevitably be displaced from side to side (e.g., the inward movement of the two center lumps in Fig. 9, left) and upwards (e.g., the upward displacement of the lump in Fig. 8, right). The C- and B-scans from Figs. 8 and 9 show both the large and medium lumps were highly detectable both in slabs with no reinforcement and in slabs that include reinforcement. However, with lumps that are exactly at the layer of reinforcement (Fig. 8, right, and the middle set of lumps in Fig. 9, right), it is clear that lumps surrounding reinforcement are highly improbable



**Fig. 8. Large clay lump slabs: (a) without reinforcement, and (b) with reinforcement**

of detection. It would be difficult or highly improbable to know these areas had clay lumps if the system were to be applied in a field application with lumps caught in the reinforcement. At these levels within a specimen, it may be inferred that a lump is

present, but the clarity is not as persuasive as in the detection of lumps located farther from the reinforcement.



**Fig. 9. Medium clay lump slabs: (a) without reinforcement, and (b) with reinforcement**

### **3.3 Fabrication, Testing, and Validation of Concrete Bridge Deck with Simulated Defects**

In addition to the above-mentioned slabs, a bridge deck constructed by the University of Texas at El Paso (UTEP) was available for blind testing. The bridge deck was constructed with known artificial delaminations, cracks, and corroded reinforcement. Several parameters were considered in the construction of the artificial delaminations including stacked delaminations, delaminations of various thicknesses (ranging from 0.3 mm [0.01 in.] to 2.0 mm [0.08 in.] thickness), sizes (ranging from 305 mm x 305 mm–610 mm x 1220 mm [12 in. x 12 in.-24 in. x 48 in.]), depths (above reinforcing steel at 64 mm [2.5 in.] below surface, and below two layers of reinforcing steel at 152 mm [6 in.]), with some located above prestressed girders supporting the slab.

The deck, pictured in Figs. 10 and 11, measures 2.4 m x 6.1 m x 0.2 m (8 ft x 20 ft x 8-3/4 in.), and rests on three prestressed concrete girders. Simulated defects constructed in the deck consist of nine artificial delaminations, five cracks, and two corroded

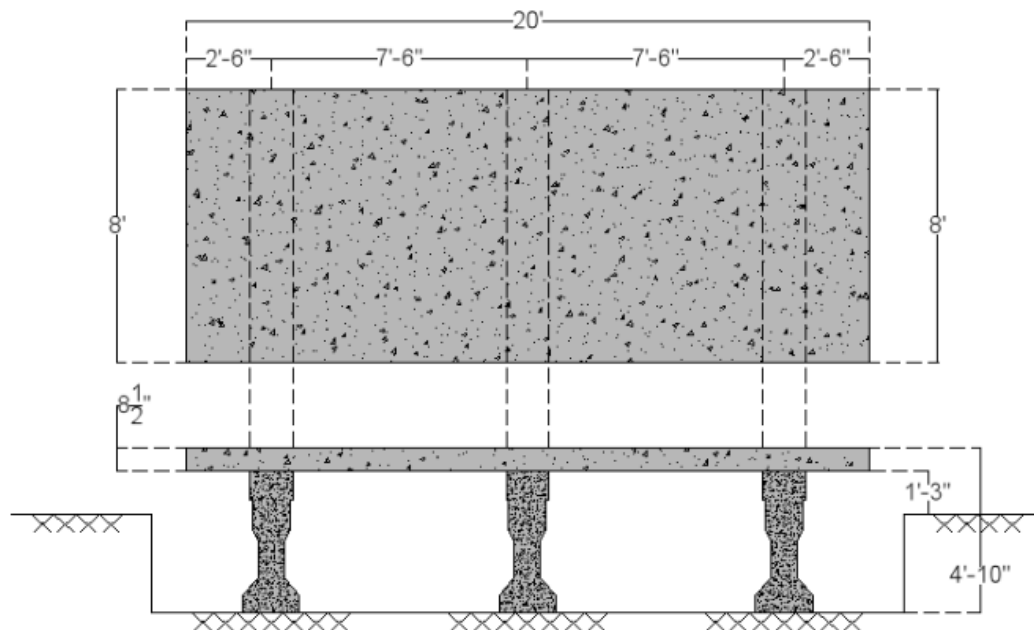


**Fig. 10. Simulated bridge deck at UTEP in El Paso, TX**

reinforcement mats, which are all summarized in Table 2.

In constructing the deck, 27.6 MPa (4000 psi) concrete was used, and two layers of No. 5 longitudinal and transverse steel were placed at 254 mm and 203 mm (10 in. and 8 in.) o.c., respectively, at centroid depths of 3.25 in. and 7.25 in. (83-184 mm) from the surface. The 28-day strength and modulus exceeded 34.5 MPa (5000 psi) and 27.6 MPa (4000 ksi), respectively. A 0.25 mm (0.01 in.) polyester fabric was used to mock an ultra-thin horizontal delamination. The vertical cracks were constructed from both thick

and thin cardboard sheets. The No. 5 corroded steel mats were electrically merged and attached to the normal reinforcement. The corrosion depth was measured to be 1-2 mm (0.04–0.08 in.) prior to pouring the concrete.








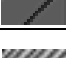








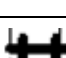
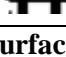
**Fig. 11. Layout of constructed bridge deck**

In addition to UST testing, ground penetrating radar (GPR) and infrared thermography (IRT) was used to compare additional NDT methods to the UST method. All three techniques and their findings are described below.

### ***3.3.1 Ultrasonic Tomography Analysis***

For the UST analysis, the grid increment used on the bridge deck (100 mm x 100 mm, or 4 in. x 4 in.) was greater in the *y*-scanning direction than the previously evaluated specimens, since this deck was actually the first specimen to be tested and an

**Table 2. Summary of simulated defects in the concrete bridge deck**

<b>Simulated Defect</b>	<b>Defect Material</b>	<b>Key Legend</b>	<b>Actual Dimension (mm)</b>	<b>Actual Depth (mm)</b>	<b>UST Measured Dimension (mm)</b>	<b>UST Measured Depth (mm)</b>
Delamination (DL 1)	Soft, high strength 1 mm foam		305 x 305	64	301 x 341	65
Delamination (DL 2)	-		610 x 610	-	578 x 642	71
Delamination (DL 3)	-		-	-	603 x 651	81
Delamination (DL 4)	Soft, high strength 2 mm foam		305 x 305	-	333 x 390	69
Delamination (DL 5)	-		610 x 610	-	587 x 650	81
Delamination (DL 6)	-		-	-		54 - 116
Delamination (DL 7)	Soft, high strength 1 mm foam		-	152	562 x 667	136
Delamination (DL 8)	-		610 x 1219	-	667 x 1197	150 - 177
Delamination (DL 9)	Soft, 0.25 mm polyester fabric		305 x 610	64	N/A*	N/A*
Vertical Crack (CK 1)	Soft, thin cardboard		305 long	-	N/A**	N/A**
Vertical Crack (CK 2)	-		-	-		
Vertical Crack (CK 3)	Soft, thick cardboard		-	76		
Vertical Crack (CK 4)	-		-	152		
Vertical Crack (CK 5)	Natural crack (observed after construction)		330 long	64		
Corroded Reinforcement (CR 1)	1 – 2 mm deep corrosion, #5 bars		762 x 762	76	Identified ***	Identified ***
Corroded Reinforcement (CR 2)	-		-	165	-	-

\* Indiscernible due to surface noise and upper transverse reinforcement

\*\* Unable to analyze crack details

\*\*\* The corroded steel mats were identified, but the map taken did not completely cover the end of the slab, so dimensions could not be verified



optimal increment was not yet established. In retrospect, this is a contributing factor for the defects in this specimen to be less defined than in the previous cases. Fig. 12 shows the defects present at 64 mm (2.5 in.) deep, and Fig. 13 shows the defects present at 152 mm (6 in.) deep. As can be seen from the UST results, six of the seven defects are detected. The one defect undetected was the 0.25 mm (0.01 in.) thin polyester fabric at 64 mm (2.5 in.) below the surface (DL 9), as well as details of the various cracks. This scan was not particularly useful for examining cracks, as the data set for the entire scan was too massive for careful evaluations via D-scans, and the B-scans were spaced too far apart for careful analysis. Nevertheless, a sample crack (CK1) is shown in Fig. 14 below. More on crack analysis and methods for mapping them can be found in Section 5.2 and 5.3. The following B-scans with their associated end-view keys are shown in Figs. 14-20 below.

### ***3.3.2 Infrared Thermography Technique and Analysis***

IRT has continued to develop over the past few decades, becoming a highly useful technique well known for its capability of detecting superficial (51-76 mm, or 2-3 in. below the surface) delaminations in concrete structures. Its use varies from being fixed on a vehicle for 360-degree tunnel inspections to handheld cameras. IRT technology is based on capturing thermal energy emissions that escape all surfaces. The images produced give information concerning the temperature gradients observed. This is extremely convenient for NDT as delaminations and voids act as thermal barriers for heat released from concrete. However, it can be highly difficult to perform this testing, as IRT devices are extremely dependent on environmental conditions. Optimal results

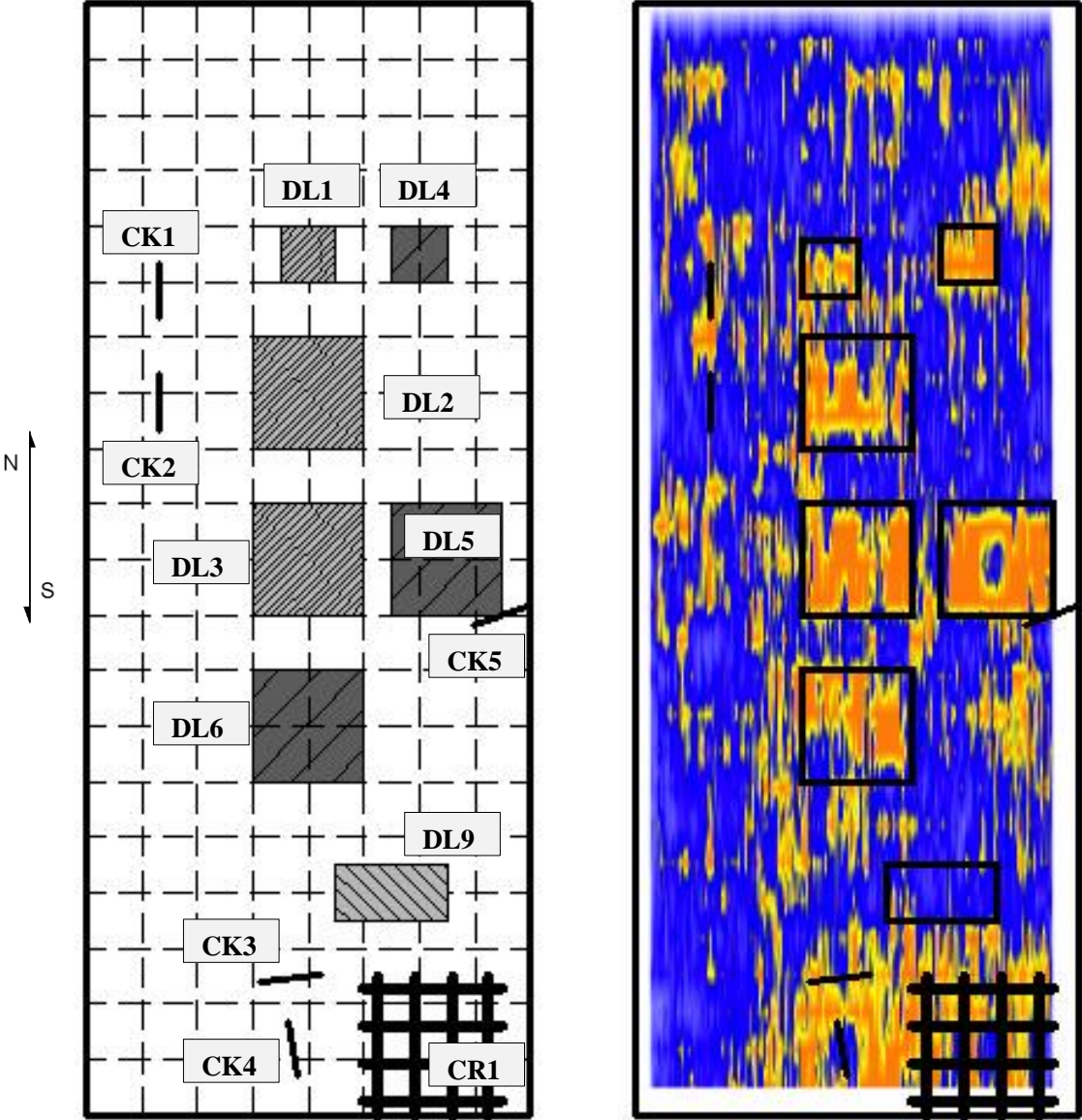


Fig. 12. C-scan at 2.5" depth: construction key (left) and UST results (right)

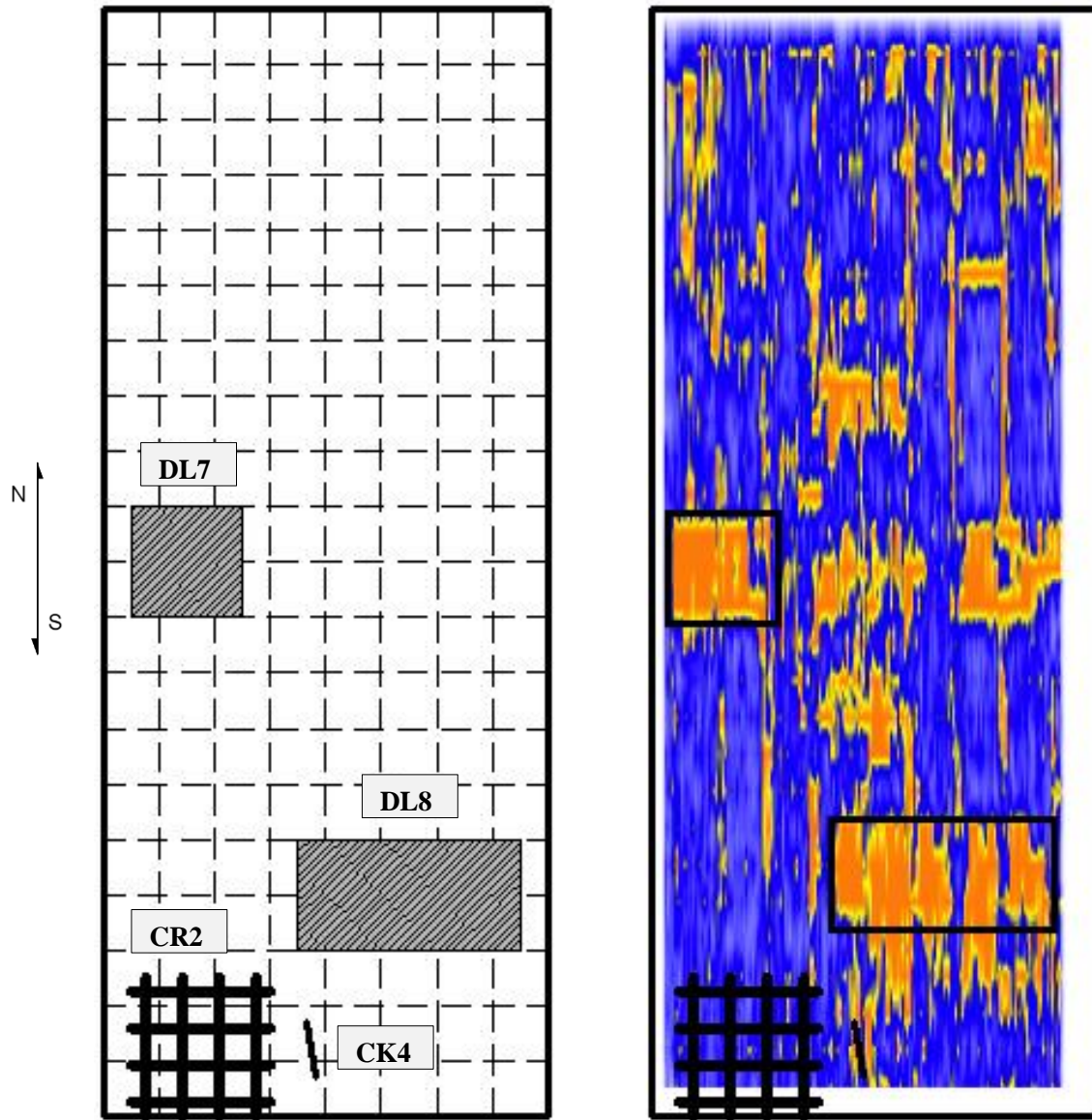


Fig. 13. C-scan at 6" depth: construction key (left) and UST results (right)

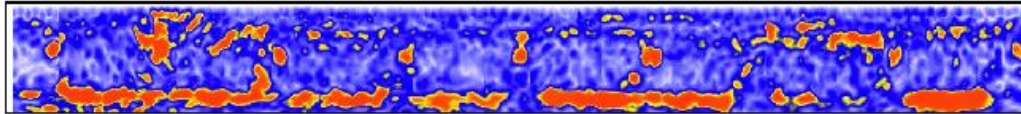
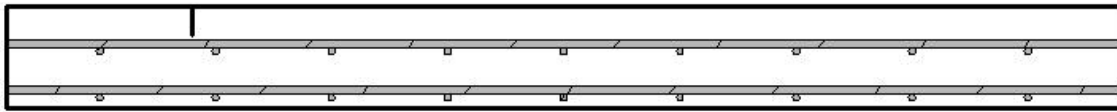


Fig. 14. B-scan showing CK 1: construction key (above) and UST results (below)

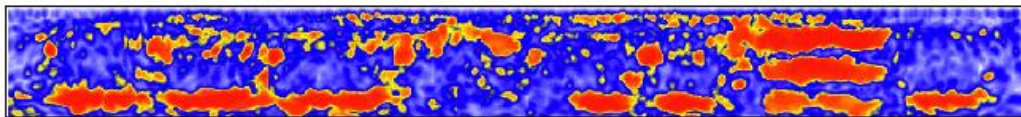
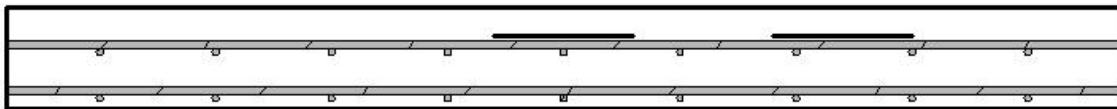


Fig. 15. B-scan showing DL 1 and 4 (l-r): construction key (above) and UST results (below)

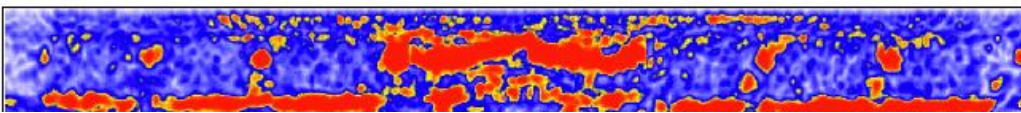
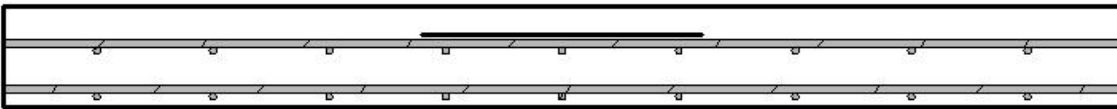


Fig. 16. B-scan showing DL 2: construction key (above) and UST results (below)

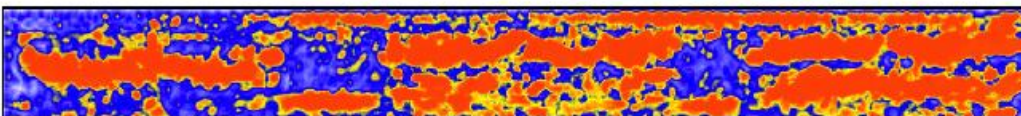
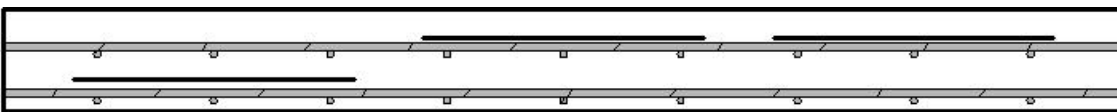
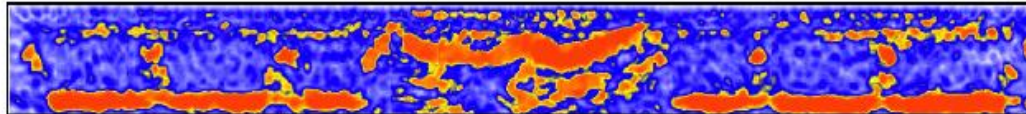
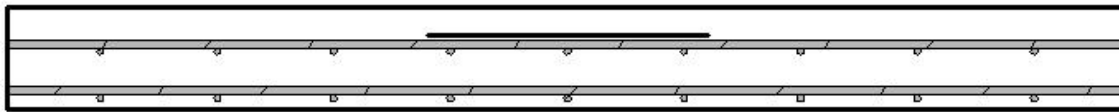
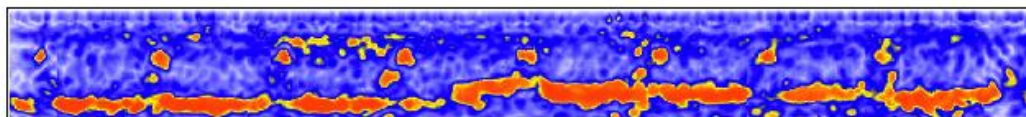
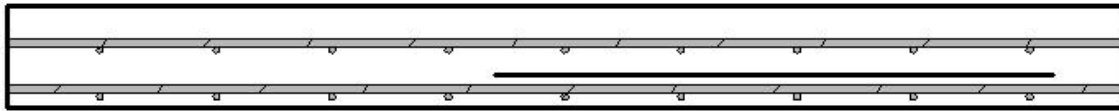


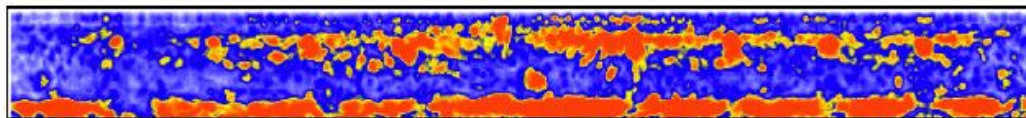
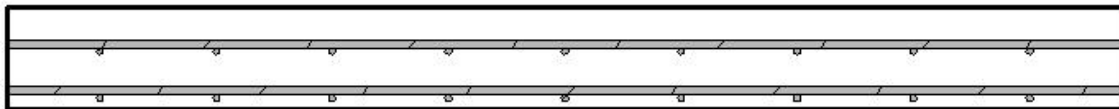
Fig. 17. B-scan showing DL 7, 3, and 5 (l-r): construction key (above) and UST results (below)



**Fig. 18. B-scan showing DL 6: construction key (above) and UST results (below)**



**Fig. 19. B-scan showing DL 8: construction key (above) and UST results (below)**



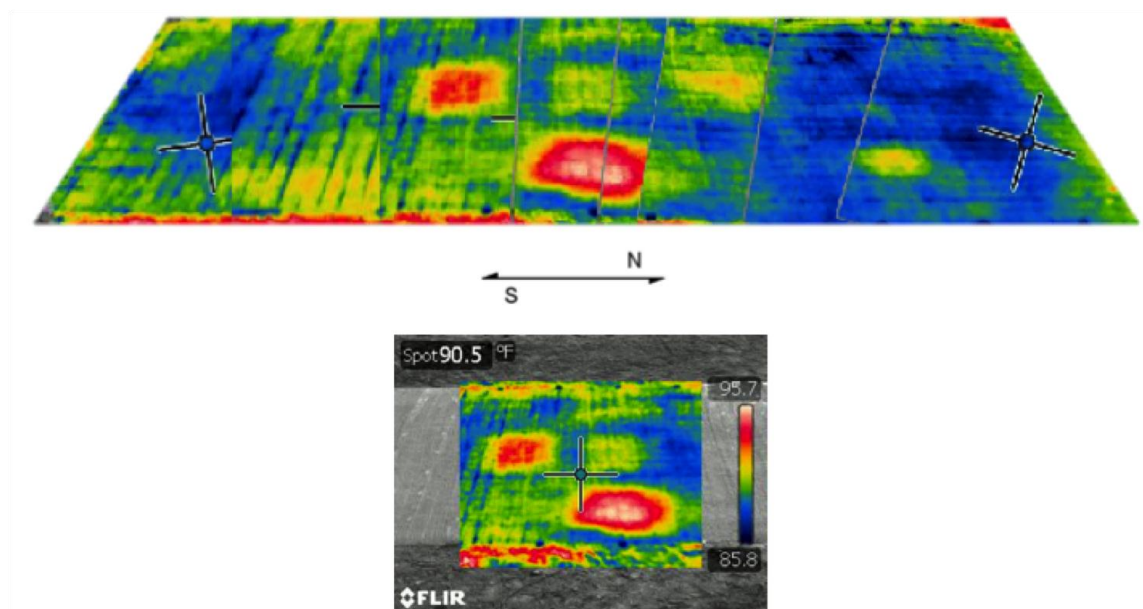
**Fig. 20. B-scan showing CR 1: construction key (above) and UST results (below)**

are obtained during the time of day when the temperature changes are more rapid.

The device used in this case study, the FLIR (Forward Looking Infrared) T300 with a 76,800 pixel resolution, operates with a  $0.05^{\circ}$  C thermal sensitivity (FLIR n.d). Since the camera is operated from a tripod and aerial photos were not accessible, single pictures were taken of the entire specimen (Fig. 21) and pieced together as a collage for

the purpose of visual representation. Because IRT is based on surface temperature, depth or defect dimensions cannot be obtained with this type of instrument.

As can be seen from Fig. 21, the device revealed the more easily detectable delaminations but could not detect corrosion, cracks, or the deep foam delaminations (152 mm, or 6 in. deep) and shallow polyester delaminations (64 mm, or 2.5 in. deep). The lack of detection with these defects is due to the defect being too deep to locate temperature differences and too thin to produce a noticeable insulating effect. DL 5 and DL 6 (see Table 2) display higher thermal emissions than the thinner (1.0 mm, or 0.04 in. thick) defects DL 2 and DL 3, which have the same area and are located at the same depth as DL 5 and DL 6. This is consistent with the fact that DL 5 and DL 6 are constructed of 2 mm, or 0.08 in. thick material, allowing these delaminations to decrease



**Fig. 21. Infrared collage (above) and single image from camera (below) of the simulated bridge deck**

the rate of heat conduction. The same can be seen for the equally sized delaminations DL 1 and DL 4, which are also located at the same depth from the surface. While DL 1 is only vaguely discernible, DL 4 is substantially warmer. Comparisons should also be made between DL 8 and DL 7, which are discernible, but whose shape cannot be well defined. DL 9, the 0.25 mm (0.01 in.) polyester fabric, cannot be seen making a substantial change in surface temperature.

### ***3.3.3 Ground Penetrating Radar Technique***

GPR is a geophysical method that utilizes electromagnetic waves (typically in the VHF/UHF frequency spectrum) emitted and received from an antenna that is moved along a testing surface. As the incident wave transverses material of differing dielectric properties, the reflected pulse displays a related change in amplitude. The amplitude of the reflected wave and the time lapse between structural interfaces (including layers, delaminations, flaws, or other discontinuities) are used to determine characteristics of the structure, including detail depth. GPR has proven to be a highly efficient method for evaluating HMA overlays (Celaya et al. 2010). However, due to the amount of electromagnetic noise, GPR data interpretation can be extremely difficult to analyze.

For the bridge deck, an air-coupled unit with a center frequency of 1 GHz was mounted to a cart and manually pushed over the specimens in question at 6 in. marked increments. The results from the GPR accurately depict the top reinforcing steel located at approximately 89 mm (3.5 in.) below the surface, and the bottom reinforcing steel at approximately 191-216 mm (7.5–8.5 in.) below the surface. Fig. 22 indicates a GPR B-scan along Section D of the bridge deck. Above the plan view showing the defects in the

bridge deck, four areas consistent with the delaminations shown along Section D are circled (defects DL1, DL2, DL3, and DL8). Defects DL4 and DL7 are seen in a similar fashion. The only other defects detected by the GPR scans are the areas of possible corrosion indicated by the increase in dielectric (shown as a black line plot in the bottom of the GPR B-scan).

Overall, the GPR technique showed success at locating steel and structure depth, as well as faint indications of delamination existing in six locations. Since GPR data acquisition is extremely efficient (data can be taken at highway speeds) this indicates the GPR technique can be favorably coupled with UST to highlight regions of interest that can then be studied via the more time-consuming UST technique.

#### **3.4 Reliability Assessment for Simulated Defect Evaluation using UST**

A summary of all simulated defects and specimen characteristics for all specimens tested can be found in Tables 1 and 2. After scanning each of the concrete/shotcrete slabs, the measurements indicated by UST inspection versus the actual measurement from ground truth data were plotted. A linear regression model was fitted to the data (Fig. 23). The types of discontinuities plotted in this manner were:

- defect depth
- defect length (parallel to B-scans, or the  $x$ -scanning direction)
- defect width (parallel to D-scans, or the  $y$ -scanning direction)
- shotcrete specimen thickness
- concrete specimen thickness
- reinforcement cover



As will be discussed in Section 3.4, coefficient of determination shows strong agreement between actual discontinuity measurements and measurements taken by ultrasonic tomography. It should be noted that defect width and length are characteristics that should be determined after scanning the region in more than one scanning direction. This is due to the fact that the phased-array tomograph is “polarized”, in the sense that shear waves are emitted and received in one direction, the  $x$ -scanning direction (or direction normal to the D-scans, as shown in Fig. 2). Objects (such as reinforcement) can therefore appear wider (measured in the  $y$ -scanning direction) than they are in reality since the B-scan is an average over a row of four transducers. In Sections 6.2 and 6.3, more of this issue with polarity is discussed, along with suggestions for future work.

### **3.5 Summary of Simulated Defect Evaluation using UST**

Ultrasonic tomography was used on a total of 31 specimens with various types of defects consisting of horizontal delaminations, vertical cracks, air- and water-filled voids, and foreign objects such as clay lumps. The UST images were then compared to documented defect locations, as well as compared with IRT and GPR evaluations.

The defect location and dimensions as well as other useful parameters were then plotted against the measurements taken from UST. Linear regression analysis indicates that the coefficient of determination ( $R^2$ ) varies between 0.82-0.98, indicating that 82-98% of the variability in defect dimensions (depth from surface, length, and width) or specimen characteristics (thickness, reinforcement cover, and spacing) measured by the UST device is directly related to the variability in the actual defect dimensions or specimen characteristics.

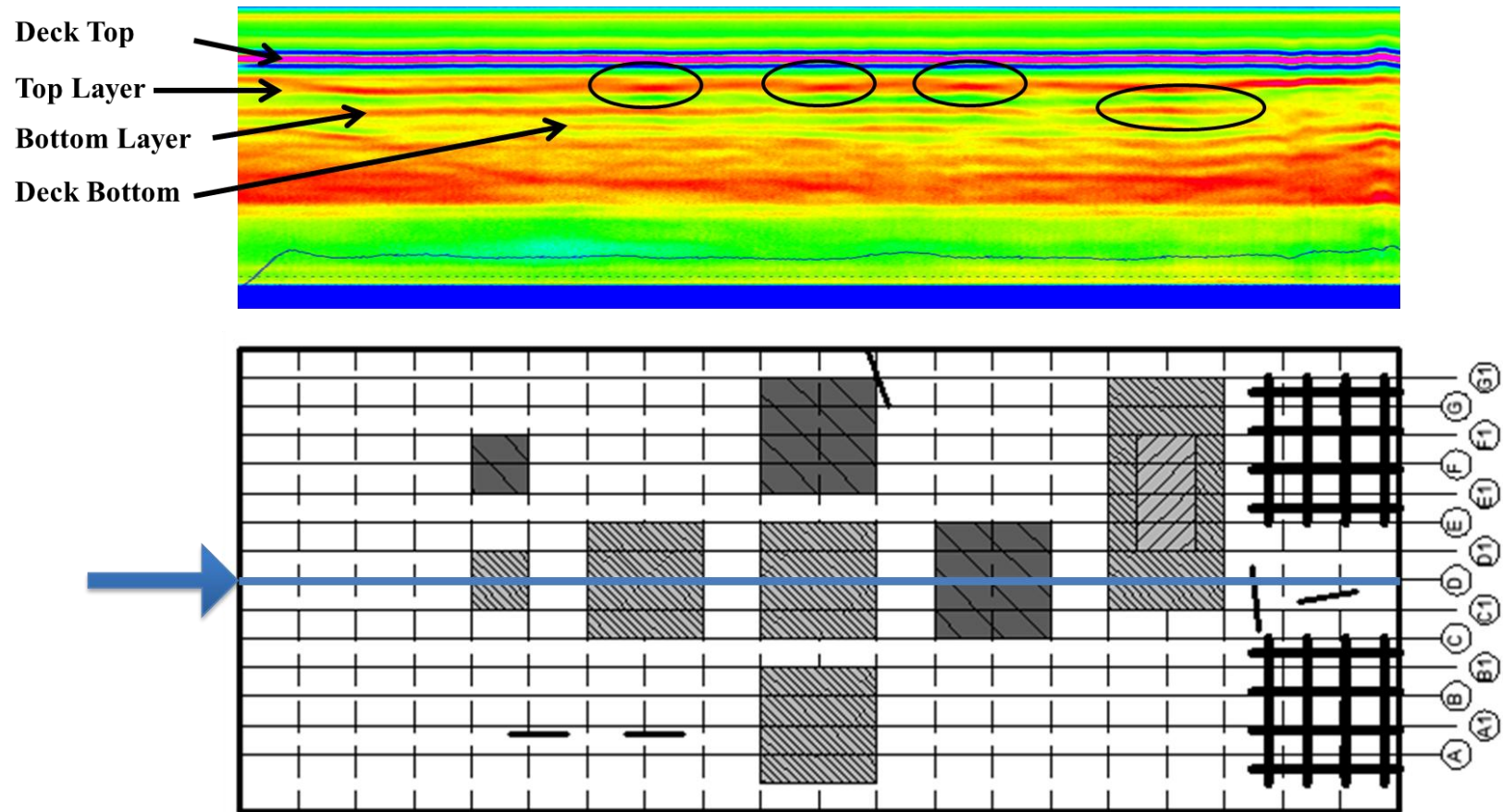


Fig. 22. GPR data indicating four areas of delamination within the top reinforcement

These evaluations on simulated specimens were invaluable for two reasons. Primarily, it instilled confidence that the method of data collection would be reliable for inspection of existing structures, particularly since coring or any type of physical validation may not be allowed. The high values for  $R^2$  translate into a reliability threshold of the system by which we can confidently map real-life structures. It is understood that further testing needs to be completed in order to have a statistical analysis that predicts confidence levels and meaningful probability of detection (POD) curves. A limitation of the research performed here is the lack of numerous constructed specimens with similar or repeated defect evaluations.

There are many variables that can be adjusted when calibrating the tomograph that will improve the accuracy of the device, including period of impulse, time-corrected gain, firing impulse pause, and wave velocity. Determination of wave velocity can be accurately estimated by averaging between 8-10 readings at different positions on the concrete surface, and there is no need for physical validation to improve the chosen speed; however, other variables can be adjusted so that the tomograph is calibrated by a known discontinuity, such as reinforcement depth or backwall reflection. Since these measurements are rarely known in existing structures to a high level of precision without destructive validation, the accuracy of the device can be difficult to fine tune prior to testing. For this reason, most of the simulated specimens were tested blindly by an operator who was not familiar with the location or type of defects to accurately mimic field testing conditions. For all simulated specimens, a wave velocity was calculated by averaging 8-10 evaluations, and no other parameters (period of impulse, time-corrected

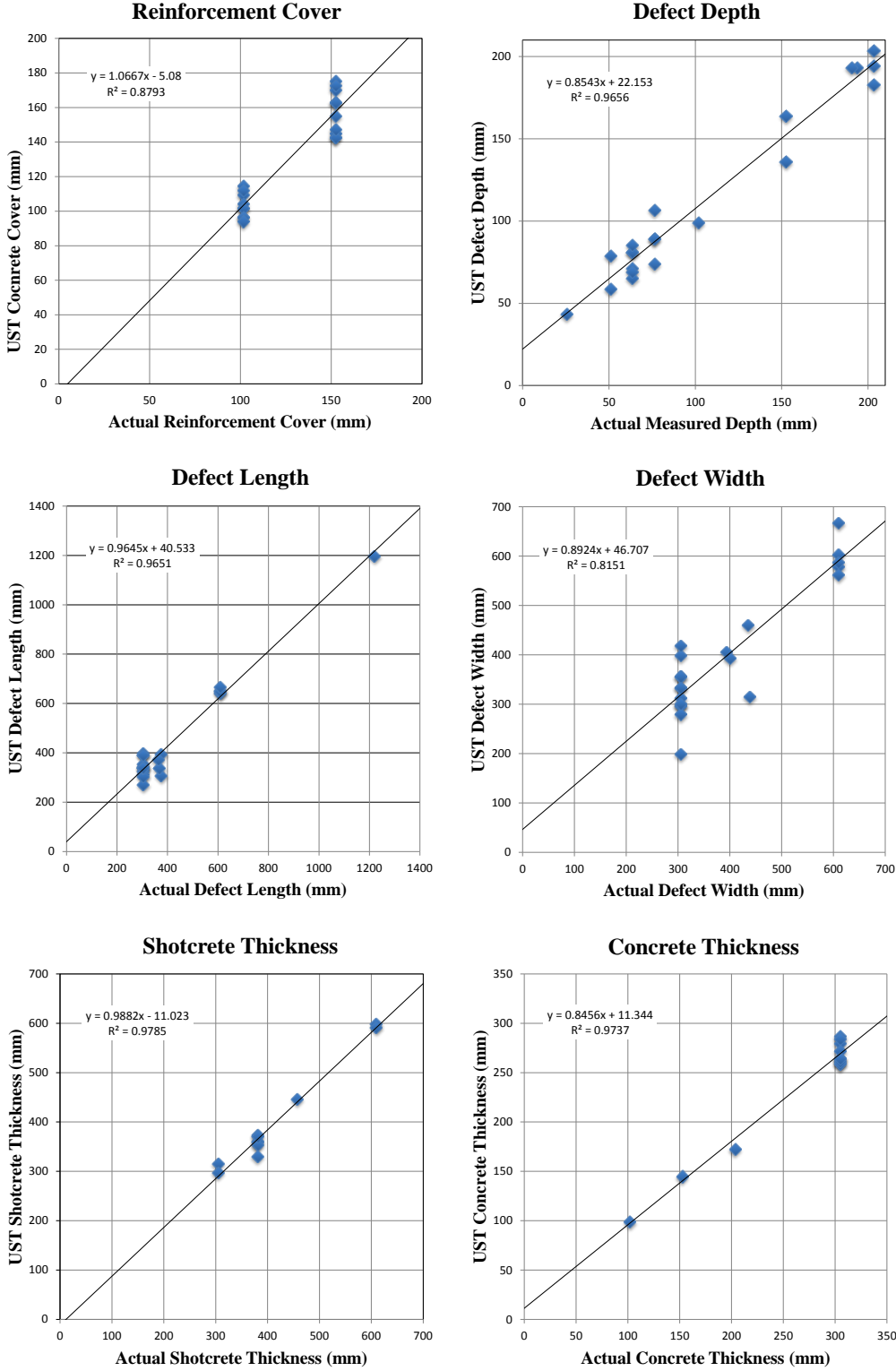


Fig. 23. R<sup>2</sup> for various defect detection parameters in the concrete/shotcrete slabs

gain, firing impulse pause) were changed from default settings. In this manner, the accuracy of the device could be predicted in preparation for testing existing structures. In Section 5.2, discussions on altering the parameters are given for the cases when the object of inspection allows the user to calibrate the device based on a known feature (i.e. precise backwall depth or steel location).

The second reason these evaluations were invaluable was the ability to try many variations of grid size, location, and creation for future use on existing structures. It was critical to learn how to relate a defect found in the 3D image reconstruction with the actual grid established on the specimen. Two methods were used for this comparison, which will be discussed in Section 5.3.

## 4. EVALUATION OF THE ULTRASONIC TOMOGRAPHY SYSTEM IN THE FIELD

For the following six test sites, limited ground truth data was available for confirmation of UST defect locations. The descriptions of the test sites, including interpretation of UST evaluations, are made using engineering judgment.

### 4.1 Eisenhower Memorial Tunnel, CO

Eisenhower Memorial Tunnel, located approximately 97 km (60 mi) west of Denver, CO, is one of a 2.7 km (1.7 mi) dual bore project started in 1968. Shown in Fig. 24, Eisenhower Memorial, which carries Interstate 70 west, is paired with the Edwin C. Johnson Memorial Tunnel, which carries Eastbound I-70. Although the eastbound bore was not completed until almost 1980, construction on the Eisenhower bore was completed by 1973. Built using drill and blast methods through a mountain with a maximum overburden of 448 m (1470 ft), the average tunnel dimensions were 14.6 m in

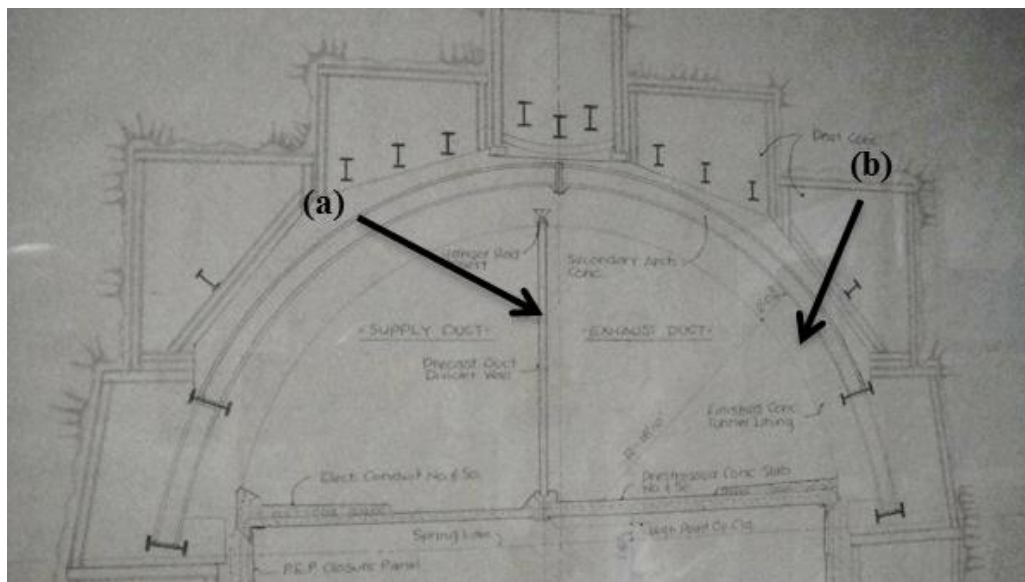


**Fig. 24. Eisenhower Memorial Tunnel, CO. Photographed by Bernd Kramarczik, <http://en.structurae.de/photos/index.cfm>**

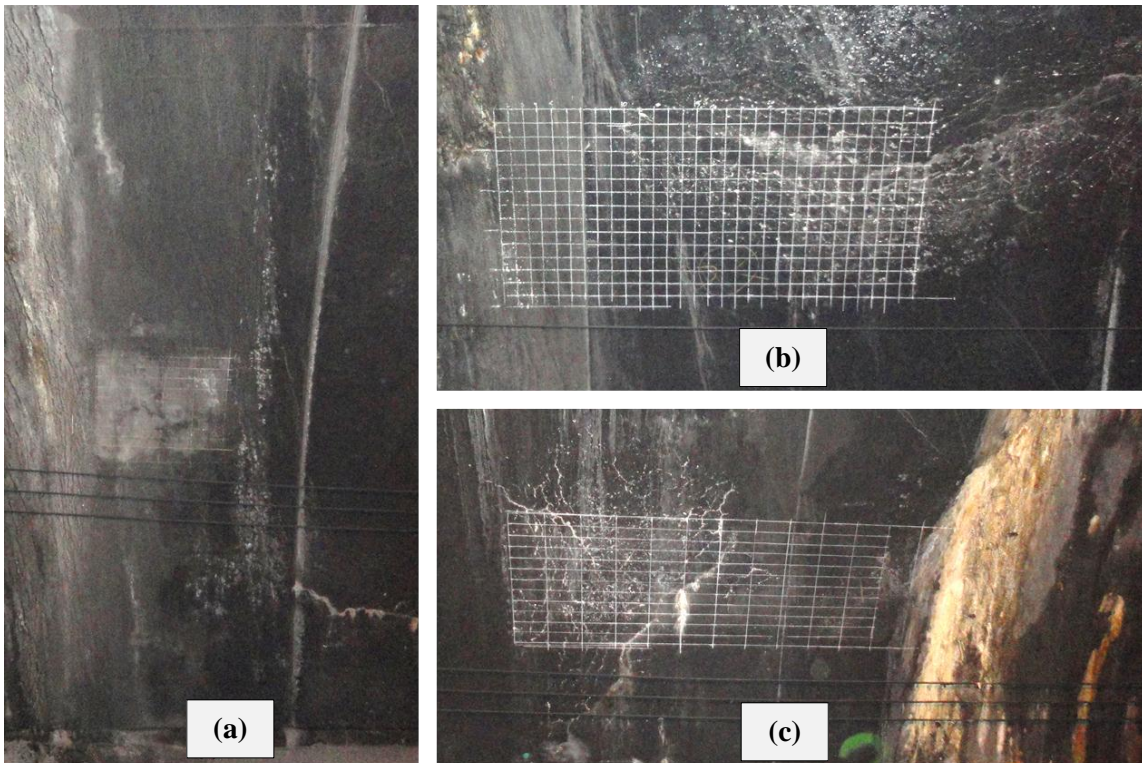
height (48 ft) and 12.2 m (40 ft) in width. In 2011, the average daily traffic was 28,155 vehicles.

All areas of interest evaluated within the tunnel were tested from inside the plenum (above the traffic), and are comprised of evaluations on the precast concrete divider wall separating the intake and exhaust portions of the plenum (Fig. 25a), and evaluations on the lining itself (Fig. 25b). Areas tested on the lining include representative locations of relatively sound (uncracked) concrete (Fig. 26a), areas with particularly extensive surface cracks and crazing near a joint in the tunnel lining (Fig. 26b), and near severe vertical cracks with stalactite formations (Fig. 26c).

As would be expected, the “sound” concrete area (Map ET 10.4-1, 2 in Appendix B) showed no signs of significant delamination, but a clear interface was observed approximately 411 mm (16.2 in.) below the surface (~239 mm, or 9.4 in. wide).



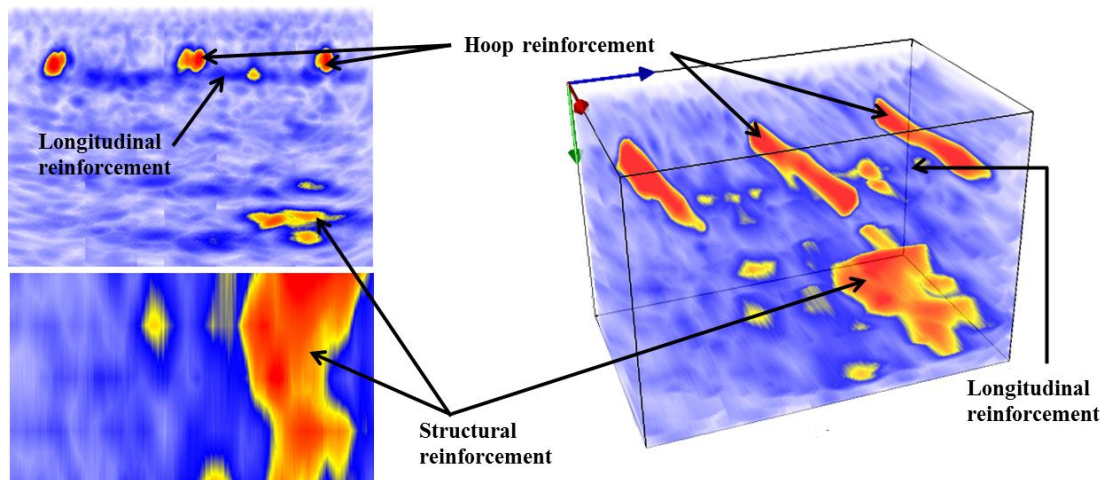
**Fig. 25. Eisenhower Tunnel testing area within the plenum: (a) the interior precast divider wall and (b) the exterior tunnel lining**



**Fig. 26. Scanned areas within Eisenhower Tunnel: (a) “sound” concrete, (b) surface cracking and crazing near joint, and (c) surface cracking and crazing near joint and crack with stalactite formation**

This interface was consistently seen at every testing location between Segments 8-10 within the Eisenhower Tunnel lining and is surmised to be part of the structural reinforcement that was in place prior to the placing of the tunnel lining. Detailed tunnel blueprints for verification at this location were not available for confirmation. Fig. 27 (a, b, and c) correspond to typical B-, C-, and Volume-scans, respectively, at this location. In the B-scan, the hoop (or circumferential) reinforcement is clearly observable at approximately 107 mm (4.2 in.) in depth and at 251 mm (9.9 in.) o.c. A single rebar as part of the longitudinal reinforcement is seen in the B-scan and Volume-scan as well.

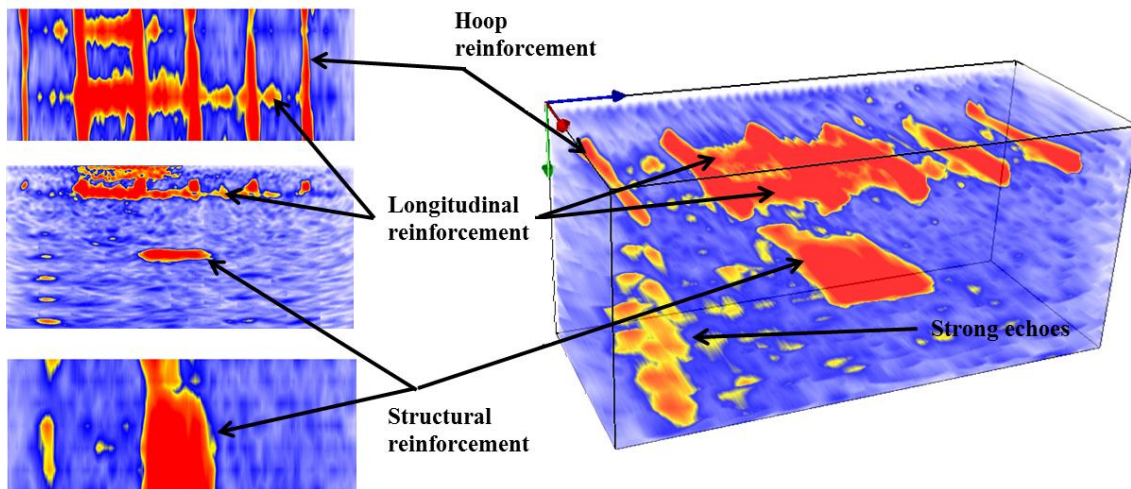




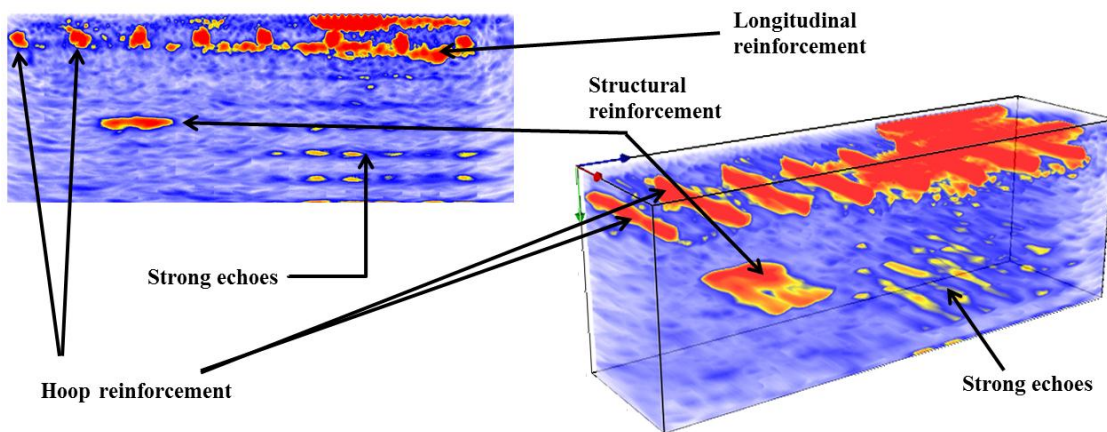
**Fig. 27. UST images of “sound” area: B-scan (top left), C-scan (bottom left), and Volume-scan (right)**

As noted earlier, one of the two areas tested that displayed significant surface cracking and crazing occurred near a joint (Map ET 10.4-4, 5 in Appendix B). At this location, the structural reinforcement is again located approximately 409 mm (16.1 in.) below the surface (~343 mm, or 13.5 in. wide). B-, C-, and Volume-scans are shown in Fig. 28. In the B-scan (Fig. 28b), the longitudinal reinforcement is seen directly under the hoop reinforcement with multiple echoes observed in increments approximately the same as the depth of the longitudinal and hoop reinforcement. These echoes are suspected to be the effect of debonding of the longitudinal and hoop reinforcement. Interestingly, this supposed debonding also occurs directly below the lining joint. This may indicate moisture intrusion has corroded the reinforcement causing debonding. Unfortunately, no ground truth data has confirmed this observation.

In the second area that displayed significant surface cracking and crazing near a joint (Map ET 10.4-3 in Appendix B), a severe crack running vertically down the tunnel



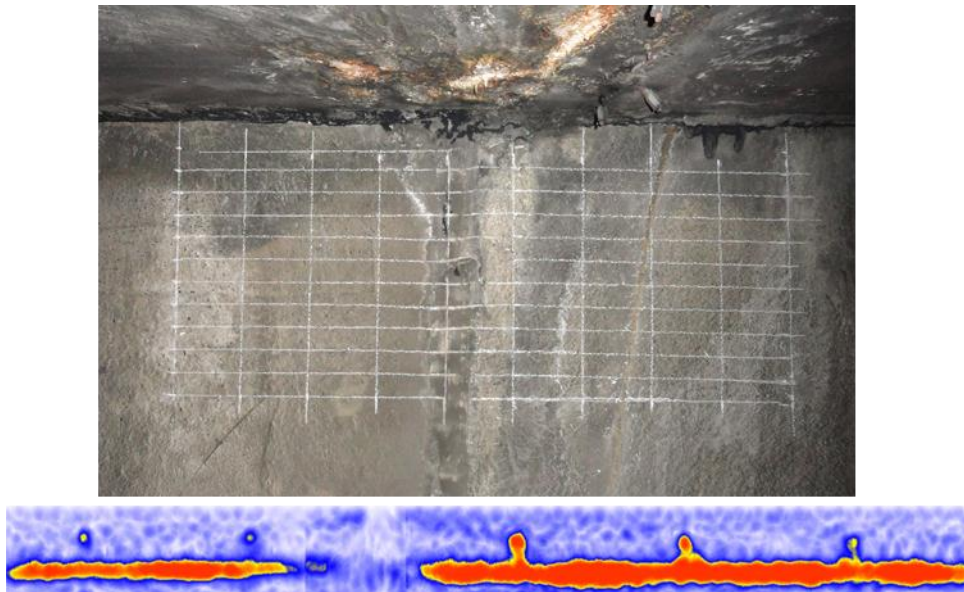
**Fig. 28. UST images of surface cracking/crazing area: B-scan (center left), C-scans (top and bottom left), and Volume-scan (right)**



**Fig. 29. UST images of surface cracking/crazing area near stalactite formation: B-scan (left) and Volume-scan (right)**

lining is present. The map was built to the side of this crack (Fig. 26c), but due to the stalactite formation and grout Zerk fittings, could not extend over the crack. The same structural reinforcement (here approximately 437 mm [17.2 in.] deep and 310 mm [12.2 in.] wide) is present in both the B- and Volume-scans (Fig. 29). Also at this location, strong echoes under the region nearest the stalactite formation and crack indicate

possible debonding of the hoop and longitudinal reinforcement. The last areas tested at the Eisenhower Tunnel were on the interior precast divider wall (particularly surrounding joints) even though significant distress was not visible. Fig. 30 shows the typical B-scan, with the region surrounding the crack completely lacking in any



**Fig. 30. B-scan of precast divider panel showing backwall reflection and reinforcement**

reflection. It is typical for large cracks (here filled with a caulking sealant) to completely attenuate all of the sound waves emitted, making it difficult to assess the presence of nearby distress. This phenomenon surrounding cracks leads to an important clue in analyzing concrete ultrasound images; the lack of reflection around an area can be indicative of an unusual amount of air, making it impossible for the shear wave to be transmitted across the boundary since gases and fluids do not support shear wave propagation.

Overall testing at Eisenhower Tunnel concluded that the UST system could consistently detect some type of structural reinforcement (other than steel rebars), although the type of reinforcement was not determined. The UST evaluation also revealed possible areas of debonding that occur near severe cracks and joints. The reinforcement cover and spacing was also detectable.

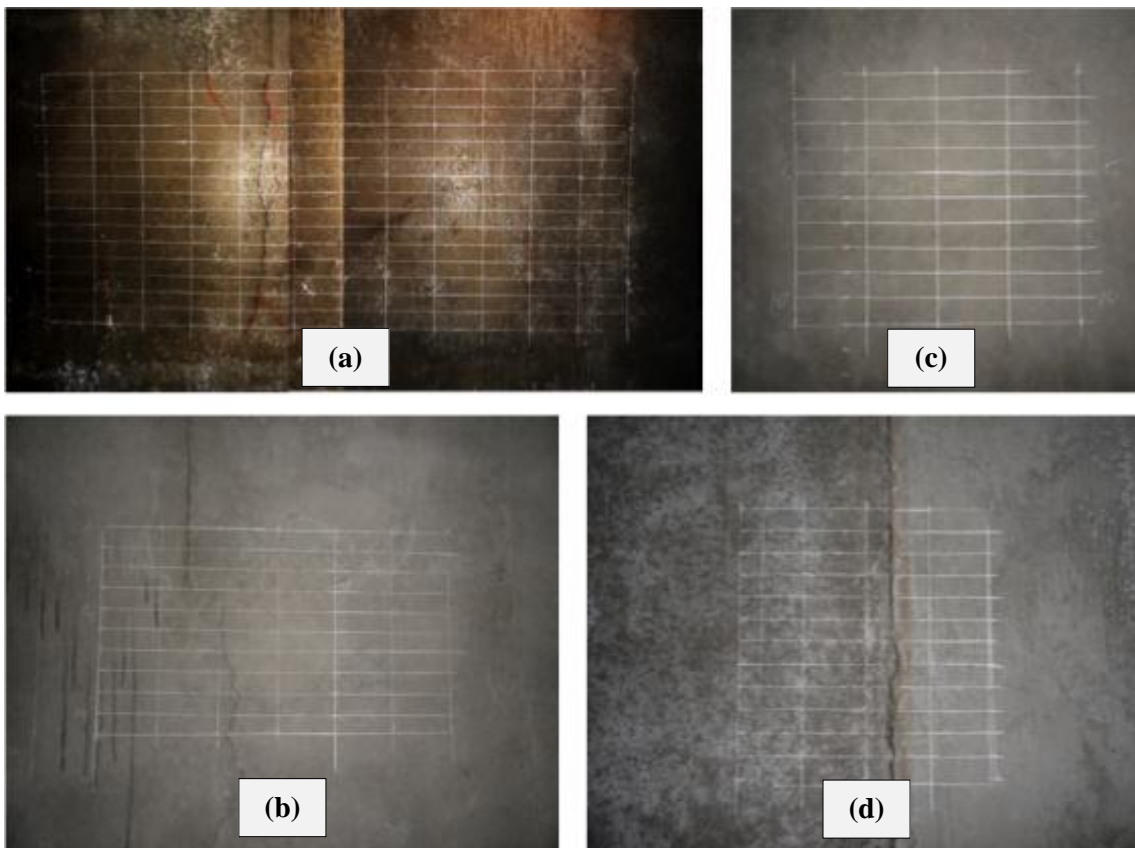
#### **4.2 Hanging Lake Tunnel, CO**

Completed in 1992 with a maximum length of 1219 m (4000 ft) through the southern wall of Glenwood Canyon, Hanging Lake Tunnel (Fig. 31) was the last link to the Interstate Highway System. Both bores of the tunnel were built using multiple-face drill and blast methods. Between the west and eastbound bores, a four-story control center monitors traffic along I-70, fully equipped with emergency response vehicles and trained staff.

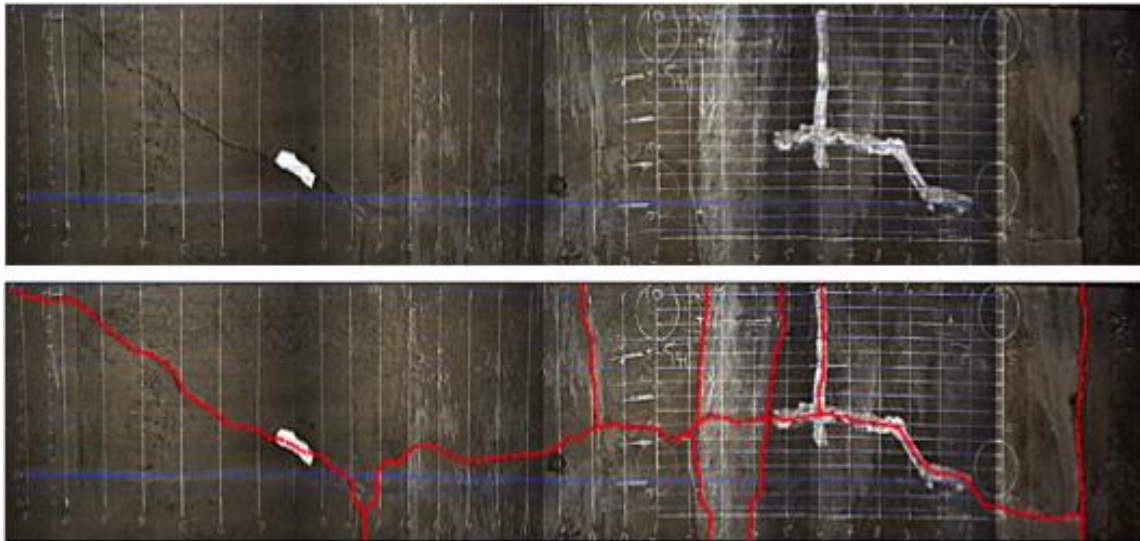
Areas of interest within the tunnel include a number of significant surface cracks (Fig. 32, a and b, as well as Fig. 33), some of which had been partially patched with a skim coat of some type of grout. Other areas include a standard “sound” concrete region (Fig. 32c), regions surrounding joints (Fig. 32d), and lastly, a region of tile in the eastbound lane (Fig. 34).



**Fig. 31. Hanging Lake Tunnel: exterior (left, from <http://www.mesalek.com/colo/glenwood/guide.html>) and interior view (right, FHWA, <http://www.fhwa.dot.gov/publications/publicroads/04mar/04.cfm>)**



**Fig. 32. Images of areas tested at Hanging Lake Tunnel: (a-b) severe vertical cracks, (c) sound concrete, and (d) lining joint**



**Fig. 33. Image collage of extensive map with cracks (shown in red)**



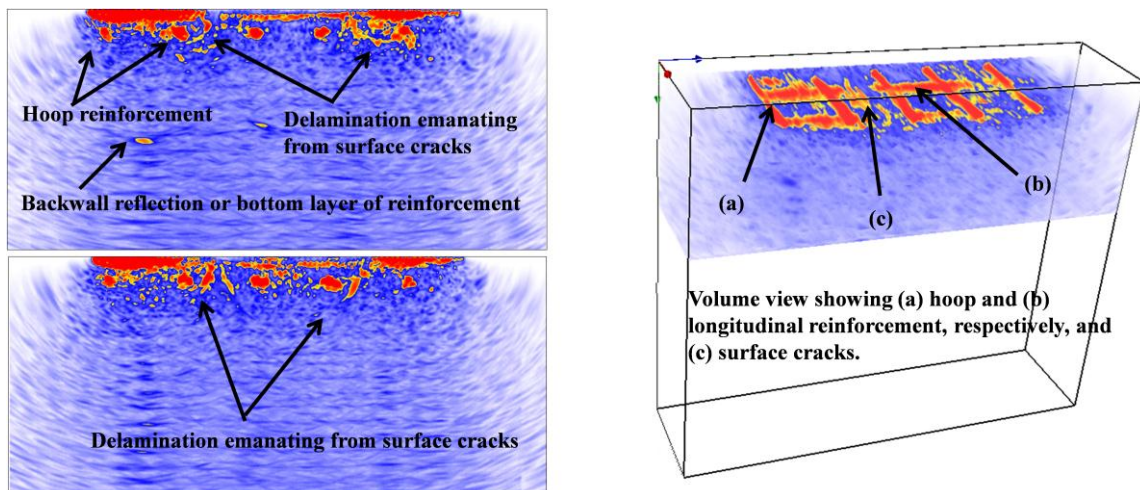
**Fig. 34. Image of tile surface that was evaluated**

The “sound” concrete region (Fig. 32c, as well as Map HLT 10.5-5, 6, 7 in Appendix B) shows that the backwall reflection varies from 752-823 mm (29.6-32.4 in.)

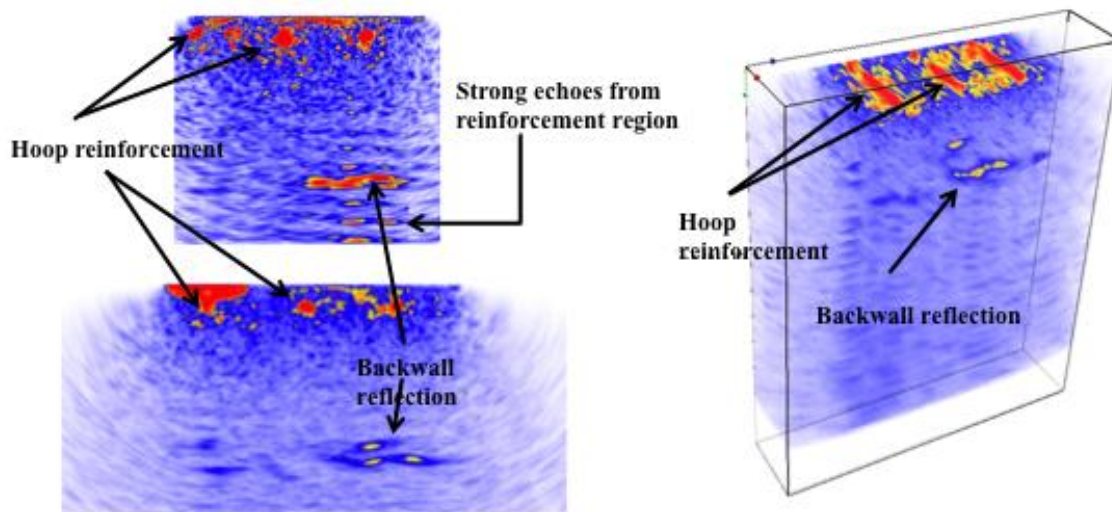
in depth, with the hoop reinforcement at 109-130 mm (4.3-5.1 in.) in depth, with a longitudinal rebar on top of the hoop reinforcement.

One area with significant surface cracks revealed shallow delaminations emanating from the surface cracks (Map HLT 10.5-1, 2, 3 in Appendix B). These cracks (Fig. 35, top and bottom left) show what looks to be the beginning stages of spalling, with the curved cracks penetrating approximately 312 mm (12.3 in.) in depth and closing towards each other. This map also revealed a backwall surface at 701 mm (27.6 in.). The hoop and longitudinal reinforcement can be seen in all scans.

Another area with significant cracking (Map HLT 10.5-8, 9 in Appendix B) did not show any sign of delamination; the surface crack appeared only to follow a single hoop reinforcing rebar. The backwall, however, was clearly distinguished at approximately 752 mm (29.6 in.) in depth (Fig. 36). Above this backwall reflection is



**Fig. 35. UST images showing surface cracks and delamination: B-scans (left) and Volume-scan (right)**



**Fig. 36. UST images showing possible deep delamination: B-scans (left) and Volume-scan (right)**

an area of high reflectivity that either corresponds to shallow (51-76 mm, or 2-3 in.) backwall delamination or the lower layer of reinforcing steel.

Another area showing significant cracking was originally mapped to cover a small area (~1.2 m, or 4 ft wide). After collecting the data, however, it was noticed that a delamination appeared around the boundary of this grid. The grid was extended to cover as much of the delamination as possible, eventually reaching over 4.9 m (16 ft). This map (HLT 10.5-10, 11, 12 in Appendix B) is shown as a collage of photos in Fig. 33. The B-scan shown in Fig. 37 (top) reveals an extensive delamination ranging from 203-508 mm (8-20 in.) below the surface and stretching over 3.4 m (11 ft) in length. The C-scans in Fig. 37 (bottom right) show the hoop and longitudinal reinforcement, as well as a plan view of the curved delamination's planar spread. Because of the significant reflection from the delamination's boundaries, the backwall reflection is not detectable.



The map tested over a joint (Fig. 32d, as well as Map HLT 10.5-4 in Appendix B) showed possible signs of debonding or the presence of voids and/or shallow delaminations at a maximum depth of 229 mm, or 9 in. (Fig. 38). Also, similar to the suspected debonding at Eisenhower Tunnel locations in Figs. 28 and 29, multiple reflections are seen at increments corresponding to the reinforcing steel depth. As noted before, these characteristic echoes are suspected to be present when debonding of the reinforcement occurs due to corrosion.

The last area tested at the Hanging Lake Tunnel was a section of tile inside the eastbound lane along the outer wall (refer back to Fig. 34, as well as HLT 10.5-13 in Appendix B). Although no backwall surface was detectable, all reinforcement could be clearly seen.

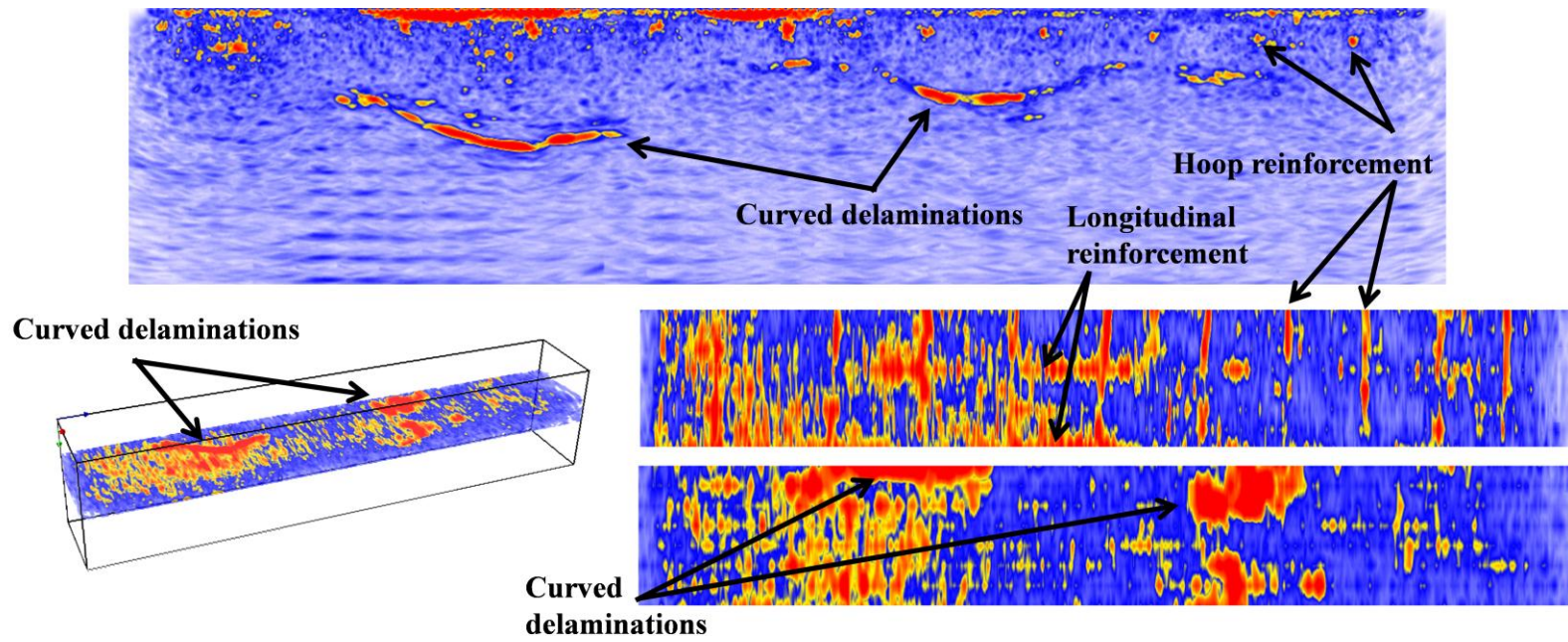


Fig. 37. UST images showing significant deep delamination: Volume-scan (bottom left), B-scan (top), and C-scans (bottom right)

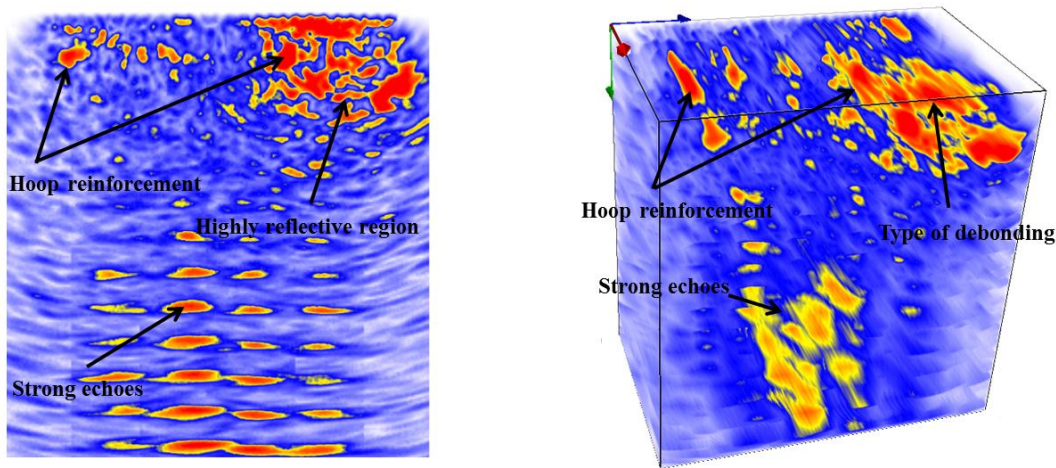
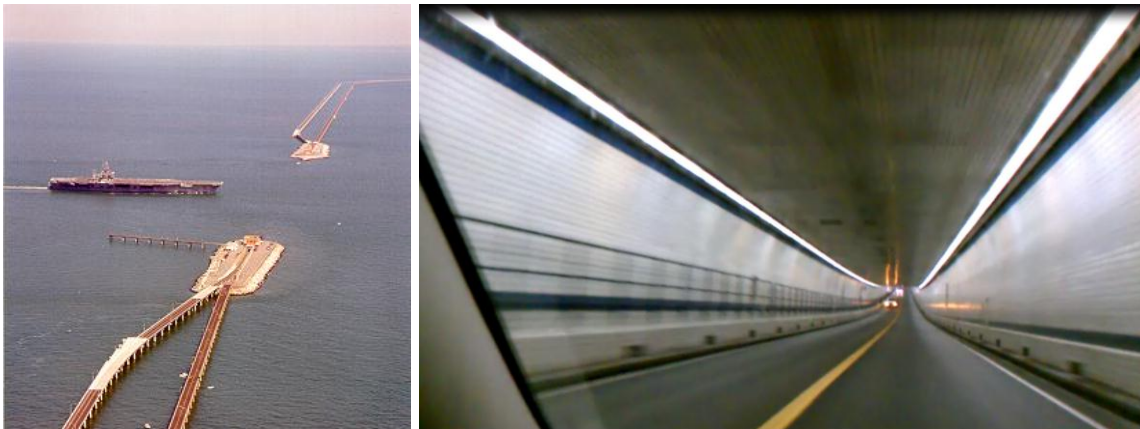


Fig. 38. UST images over lining joint: B-scan (left) and Volume-scan (right)

### 4.3 Chesapeake Channel Tunnel, VA

The Chesapeake Channel Tunnel (Fig. 39) is one of two tunnels that comprise the Chesapeake Bay Bridge Tunnel system, joining southeastern Virginia to the Delmarva Peninsula. Hailed worldwide as a modern engineering wonder, the 37 km (23 mi) long system includes 3.2 km (2 mi) of causeway, four manmade islands, 8.9 km (5.5 mi) of approach roads, 19.3 km (12 mi) of low-level trestle, two 1.6 km (1 mi) steel tunnels, and two bridges. The Chesapeake Channel Tunnel (during construction and briefly afterward it was called the Baltimore Channel Tunnel) was constructed using a cut-and-cover method. Precast steel tubes, fabricated and assembled in Orange, TX, were floated to a ship yard in Norfolk, VA, where the reinforced concrete linings and roadway was constructed. The sections were floated to the site before being sunk into a trench. Each steel tube, 483 m (300 ft) in length and 60 m (37 ft) in diameter, was joined to the other, sealed, and connected to its adjoining section. As each



**Fig. 39. Chesapeake Channel Tunnel: exterior (left, from <http://www.cbbt.com/history.html>) and interior view (right)**

steel section is welded together, patches between the 483 km (300 ft) sections had to be formed with concrete to make an overlapping seal.

As testing began, a cart with an attached GPR antennae was wheeled throughout the entire length of the 1.6 km (1 mi) tunnel in various configurations. The data from the GPR evaluations revealed two significant features. The first was a change in steel layout. Within two segments of the entrance to the tunnel, the layer of reinforcement in the GPR scan showed a change, although specifics of the change were indiscernible. Two maps were built on what appeared to be a representation of “sound” concrete; one before the change shown in the GPR, and one after the change (Maps CBBT 10.11-1 through 4 in Appendix B). The first area, shown in Fig. 40a, revealed that the hoop reinforcement was approximately 61 mm (2.4 in.) in depth and 112 mm (4.4 in.) o.c., with the longitudinal reinforcement located directly beneath it. The backwall at this location was identified to be 627 mm (24.7 in.) from the surface. The second area, shown in Fig. 40b, revealed the hoop reinforcement to be 58 mm (2.3 in.) in depth and 300 mm (11.8 in.)

o.c., with the longitudinal reinforcement located directly beneath it. The backwall at this location was 620 mm (24.4 in.) from the surface. After consulting the blueprints for these two areas, it was verified that the first bridge section on both ends was constructed with the hoop reinforcement at 114 mm (4.5 in.) o.c., and the rest of the sections were constructed with the increase to 305 mm (12 in.) o.c. The plans also indicate all wall thicknesses were to be 610 mm (24 in.) in depth. Comparison of the two B-scans showing the difference in hoop rebar layout is shown in Fig. 41.

The second significant feature of the GPR data was the occasional spike in dielectric. Almost every noticed spike in dielectric corresponded to a lining seam or crack, and was marked for ultrasonic inspection.

Spalling and corrosion are the two predominant damages this tunnel is facing (see Fig. 42 for typical spalling and corrosion damage), therefore the areas of greatest interest were identified to be cracks through which water seeps, or “live cracks”. The primary objective was to cover as much of a variety of cracking conditions located by the GPR dielectric as possible. The most significant live cracks, shown in Fig. 40 (c-d), were evaluated by building a map that spanned across the crack in such a way as to “capture” the origin of the crack. This would theoretically cover the entire surface area of the visible crack for detailed analysis, but due to time constraints, was not practiced at this location. It should be noted that these maps, though large, took from 30 minutes to an hour and a half for data collection.

The area shown in Fig. 43 (top right) displays a live crack at Sta. 474+27 ft (Map CBBT 10.11-5 in Appendix B). The backwall surface, clearly located at 612 mm

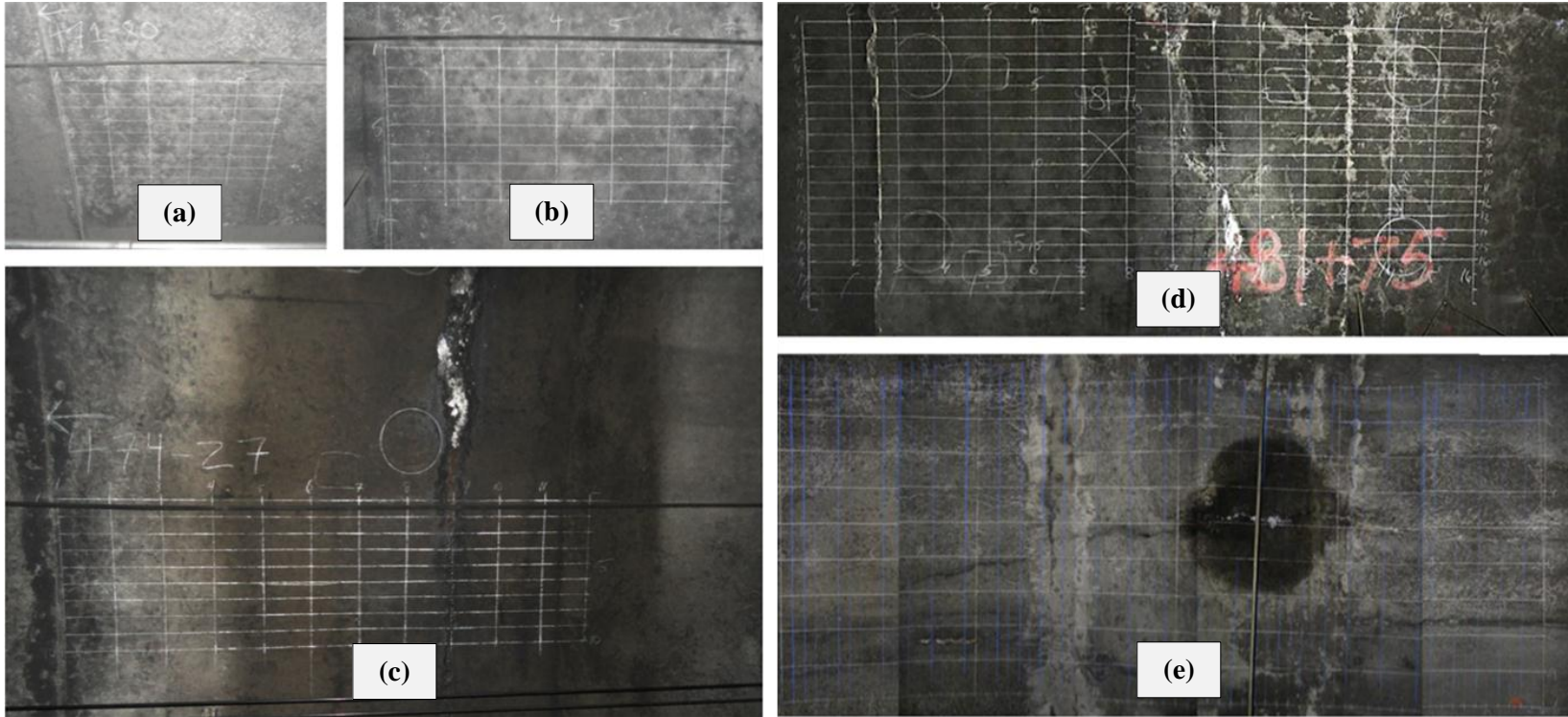


Fig. 40. Areas tested at Chesapeake Bay Tunnel

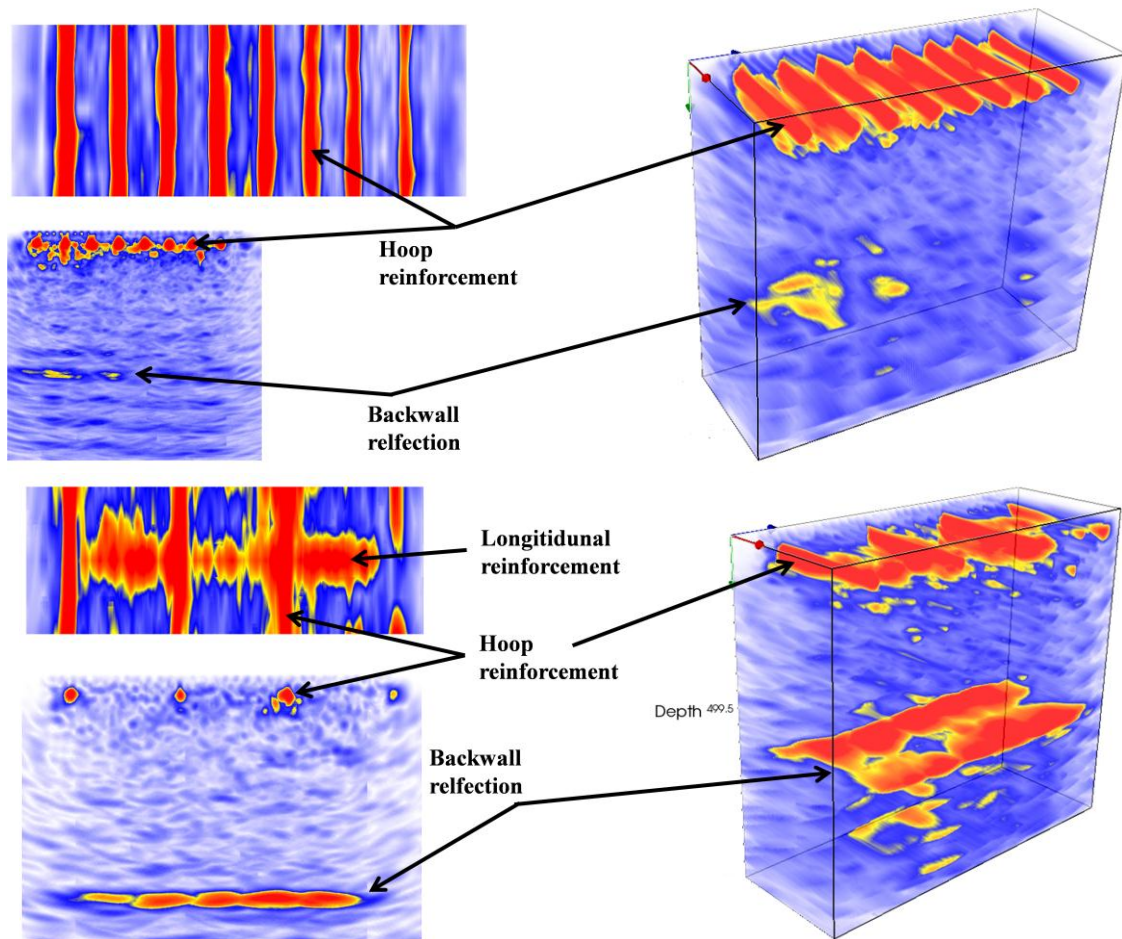


Fig. 41. Comparison of steel layout differences

(24.1 in.) below the surface, is consistent with tunnel blueprints that depict the lining to be approximately 610 (24 in.) in depth. Also in line with the tunnel blueprints for this section of tunnel is the reinforcement spacing. The tomograms indicate the hoop reinforcement to be located at approximately 305 mm (12.0 in.) o.c., at a depth of 51-66 mm (2.0-2.6 in.), along with longitudinal reinforcement located directly beneath (Fig. 39, c and d). The blueprints for this section indicate the hoop reinforcement to be 305 mm (12 in.) o.c., with the longitudinal reinforcement directly underneath.



Fig. 42. Typical spalling and corrosion

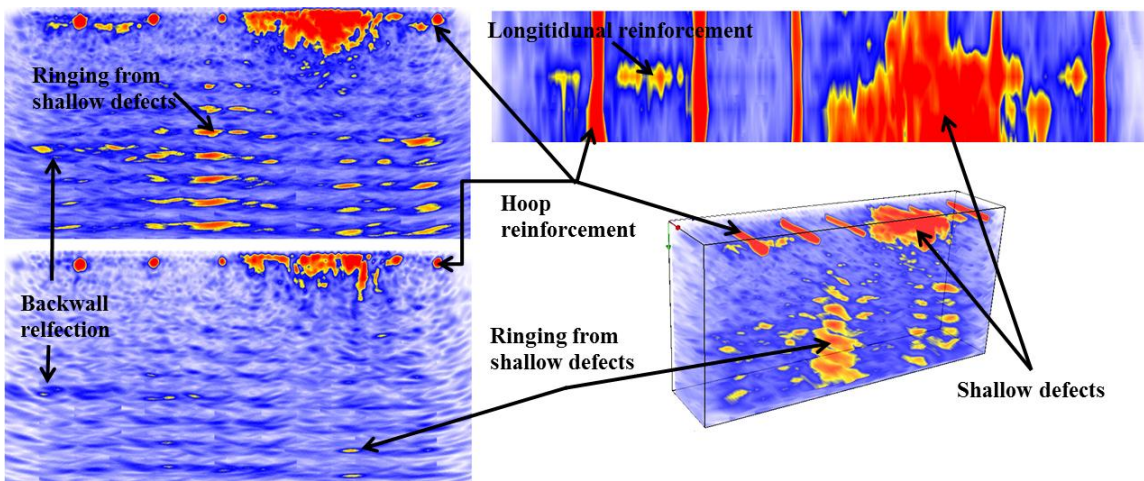
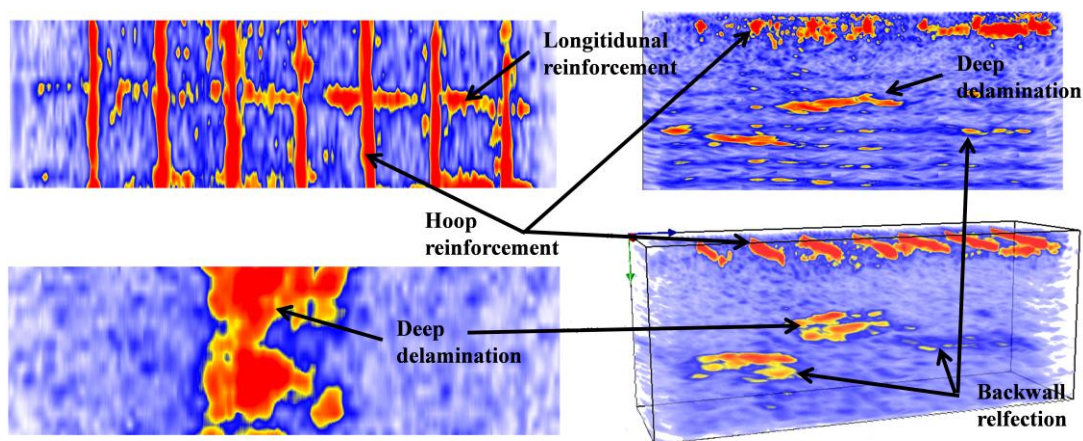


Fig. 43. Area surrounding "live" crack



Surrounding the surface cracks, the tomograms also indicate severe shallow defects, including cracks as deep as 229 mm (9 in.) and possibly shallow delaminations approximately 51 mm (2 in.) below the surface. The heavy ringing surrounding the cracked region (Fig. 43, top left and both bottom images) indicates discontinuities that are suspected to have occurred surrounding the reinforcement.



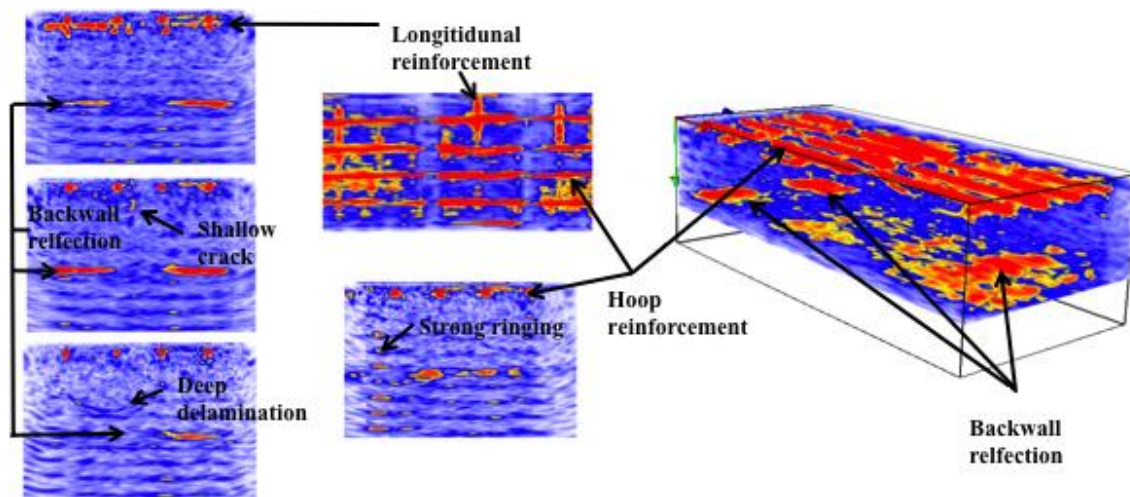
**Fig. 44. UST images at STA. 481+76 showing deep delamination**

Another map covering a severe crack, located at Sta. 481+76 (Map CBBT 10.11-13 in Appendix B) was built to completely capture the width of a delamination less than 102 mm (4 in.) below the bottom surface (from the steel plate). Shown in Fig. 44, this delamination may originate from the layer of hoop reinforcement nearest the steel skin. The backwall surface, a little more than the typical 610 mm (24 in.) in depth, was measured to vary between 676-721 mm (26.6-28.4 in.). The delamination was approximately 513 mm (20.2 in.) below the surface, and approximately 696 mm (27.4 in.) in width. The hoop reinforcement is located approximately 307 mm (12.1 in.) o.c., at

a depth of 51-91 mm (2.0-3.6 in.), along with longitudinal reinforcement located directly beneath. The blueprints for this section indicate the hoop reinforcement to be 305 mm (12 in.) o.c. with the longitudinal reinforcement directly underneath.

Another area of interest involved a circumferential crack that had only just begun to indicate signs of moisture intrusion (Fig. 40e, and Map CBBT 10.11-10 in Appendix B). A map was built around this crack, attempting to cover as much of the length of the crack as was possible from inside the plenum. Another feature that made this crack interesting was the presence of a longitudinal crack in that area between the stainless steel ceiling hangers (visible in Fig. 40e approximately one-third the distance from the left side of the image). The backwall surface was clearly distinguishable, and ranged from 577-658 mm (22.7-25.9 in.) below the surface (Fig. 45). The hoop reinforcement measured to be 69-81 mm (2.7-3.2 in.) in depth and 307 mm (12.1 in.) o.c., and the longitudinal reinforcement measured 434 mm (17.1 in.) o.c. This matches with the blueprint's details of 305 mm (12.0 in.) o.c. for the hoop reinforcement, but the plans do not indicate spacing for the longitudinal. As seen in Fig. 45 (top left B-scan), there appears to be two layers of hoop reinforcement, but as this is not indicated in the blueprints, it is possible that this could be an area of a splice. Light reflections, or echoes, are seen throughout the entire region of the crack, specifically surrounding the reinforcement nearest the moisture. Debonding of the reinforcement is suspected here due to corrosion.

The "gap" in the backwall reflection (Fig. 45, B-scans on left) and the omission of some of the hoop reinforcement (Fig. 45, Volume-scan on right and C-scan top



**Fig. 45. UST images surrounding circumferential crack**

center) indicate the presence of a crack. When cracks are present, the ultrasonic waves are strongly attenuated, causing the reception of the signals to be scarce if not completely absent. The other noticeable feature in this map is the possibility of a curved delamination approximately 450 mm (17.7 in.) in depth and up to 483 mm (19 in.) wide (Fig. 45 bottom left). It is also apparent from Fig. 45 (center left B-scan) that a surface cracks appear to extend a maximum of 249 mm (9.8 in.) in depth.

The last section tested within the plenum was a location detected by a high spike in GPR dielectric. Upon investigation, no live crack was found, but rather a dry seam. Although no visible signs of distress were apparent, hammer tapping revealed an extremely shallow delamination that appeared close to separating and falling. A grid was applied to this region surrounding the seam and shallow delamination and the area broken up into two sections, Region I (Map CBBT 10.11-9 in Appendix B) and Region II (Map CBBT 10.11-7, 8 in Appendix B), as shown in Fig. 46.

Region I UST evaluations reveal significant cracks and/or voids as deep as 218 mm, or 8.6 in. (Fig. 47, bottom left). The hoop reinforcement is shown to vary between 51-76 mm (2.0-3.0 in.) in depth at approximately 310 mm (12.2 in.) o.c., with the longitudinal reinforcement located directly beneath at 503 mm (19.8 in.) o.c. The backwall in this section varies from 617-660 mm (24.3-26.0 in.).

Region II UST evaluations, shown in Fig. 48, show the delaminated region (marked as “shallow delamination”) and also show the presence of cupped delaminations as deep as 488 mm (19.2 in.) below the surface, or approximately the same depth as the lower reinforcement closest to the tube skin. The backwall in this area ranged from 612-660 mm (24.1-26.0 in.). The hoop reinforcement at 56 mm (2.2 in.) deep was found to be 307 mm (12.1 in.) o.c., with the longitudinal rebars underneath at 411 mm (16.2 in.) o.c.

The last two areas tested within the Chesapeake Bay Tunnel were both located in the driving lane, along the tiled wall lining. One of these areas (Fig. 49, left) was discovered by using data from SPACETEC, a German company that utilizes a contact-free scanning system that provides detailed images, profiles, and thermal data for tunnel linings (<http://www.spacetec.de>). After evaluating the Chesapeake Bay Tunnel, SPACETEC’s analysis report revealed an area detected by the infrared scan, indicating possible debonding. When debonding occurs beneath tile, hammer sounding by ear or by microphone can readily differentiate bonded from debonded tile. Debonded tile can occur for two reasons: (1) improper installation (wrong type of thinset, disproportionate water ratios, improper mixing, and/or low standard of workmanship, i.e. not

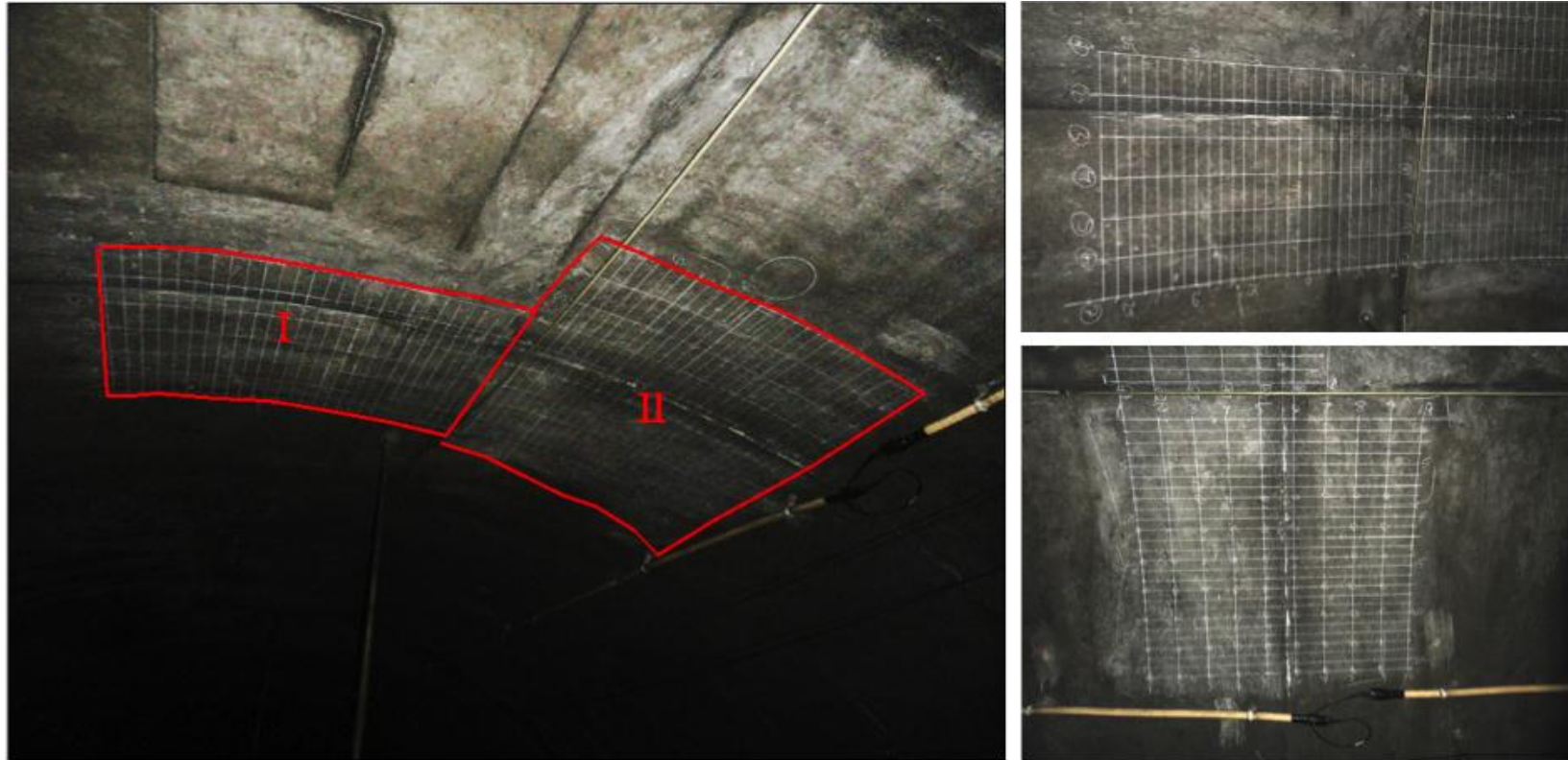


Fig. 46. Images depicting Region I (top right) and Region II (bottom right)

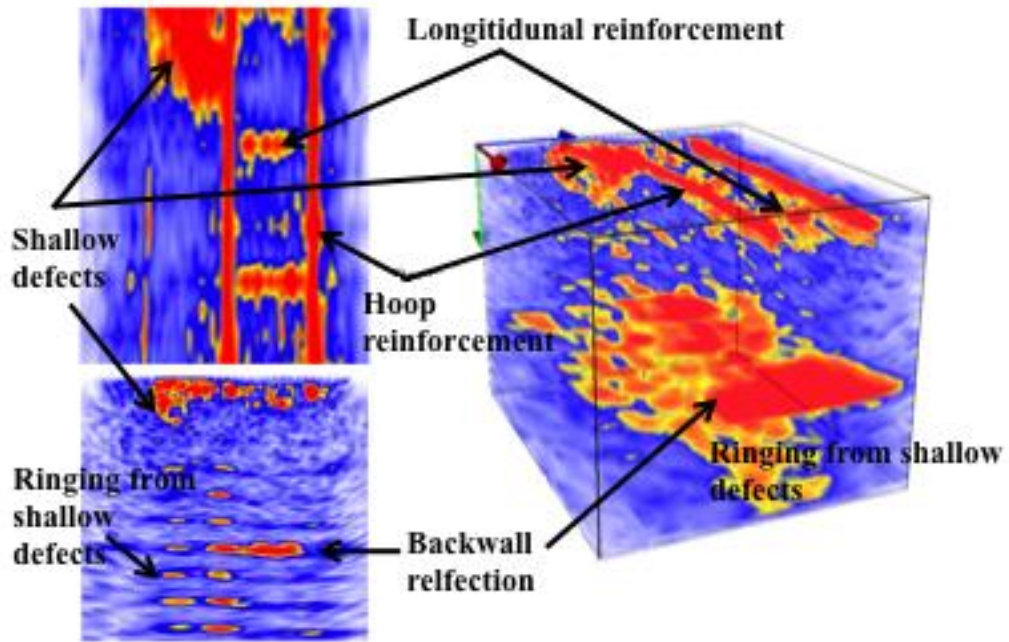


Fig. 47. Region I UST images

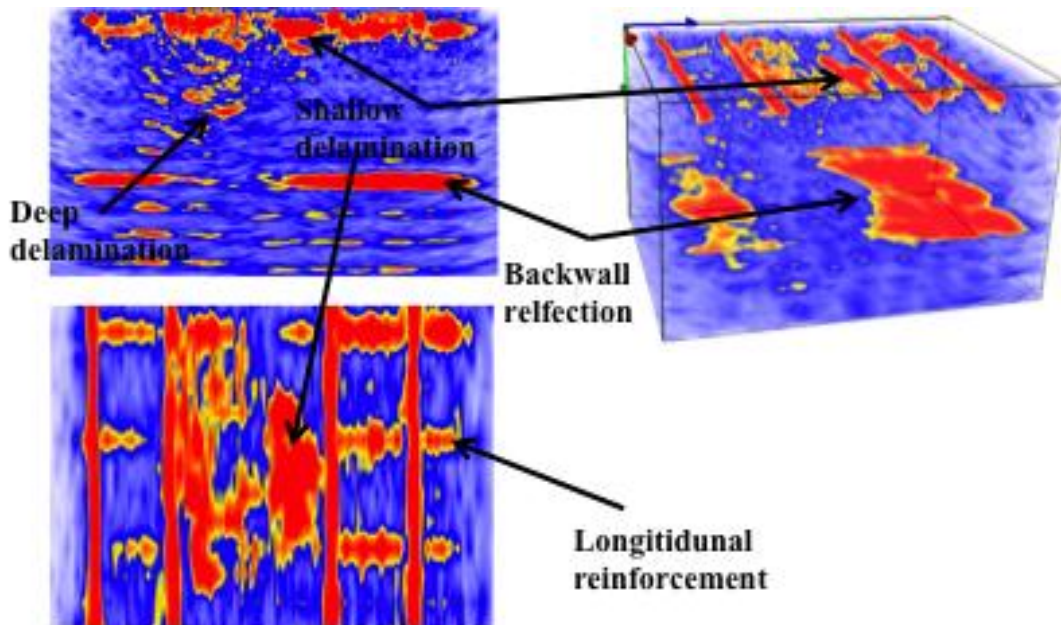
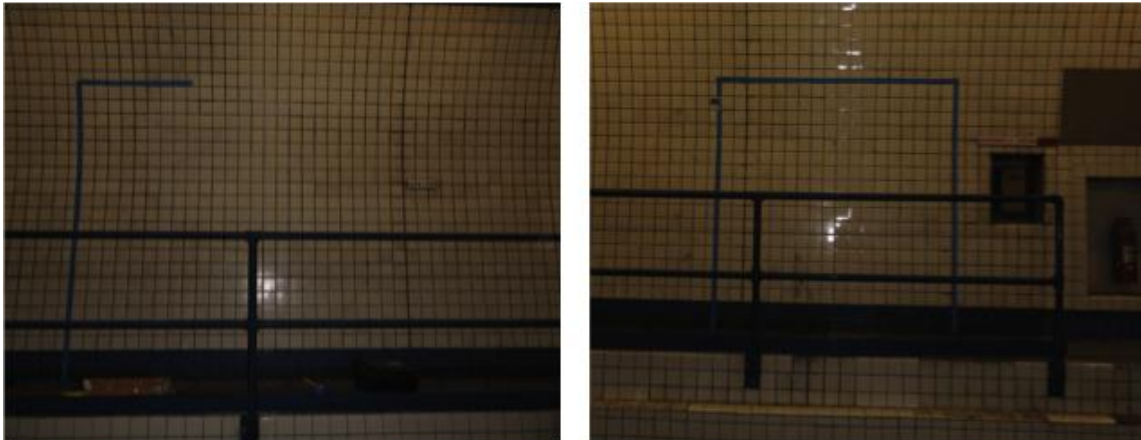
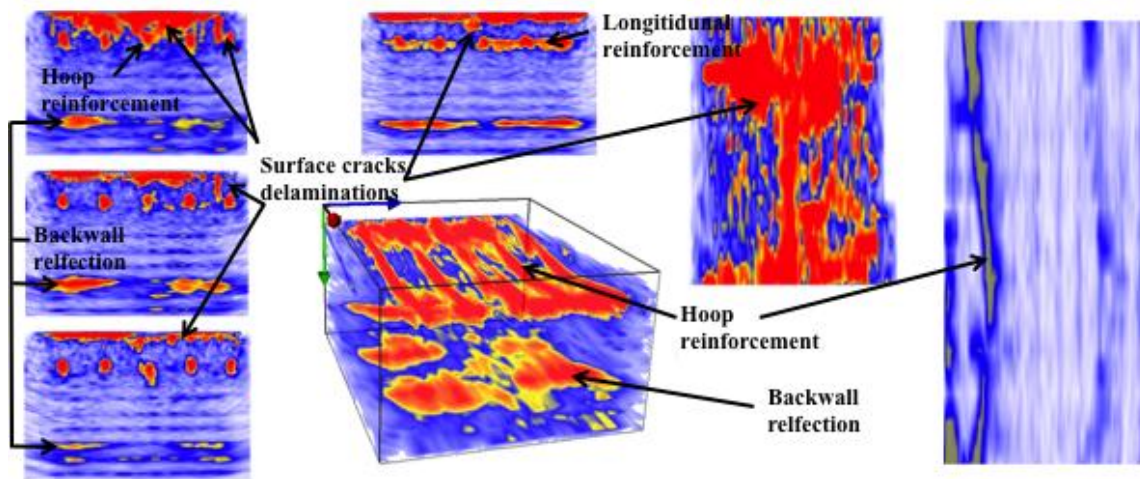


Fig. 48. Region II UST images



**Fig. 49. Tile lining sections in Chesapeake Bay Tunnel**

backbuttering the tile) or (2) presence of degrading agent (typically water) behind the tile lining. If the debonding occurs for the first reason, reapplication of the tile lining can solve the problem. However, when debonding occurs due to cracks that facilitate the degradation of the thinset by moisture entrainment, NDT techniques can hopefully be used to determine the source of such moisture. Therefore, it became a goal to search for a damaged area that was not verifiable by sounding techniques. In other words, we wanted to determine the beginning stages of tile debonding before the tile debonding actually occurred to a noticeable extent. SPACETEC's data served this purpose very well by determining an area (Fig. 49, left) that showed signs of possible delamination but was not detectable via hammer sounding. Fig. 49, right, details a damaged area that includes debonded tile detectable by hammer sounding. The UST results from scanning the area determined by SPACETEC's data are shown in Fig. 50 below. The three B-scans (Fig. 50, left images) indicate the backwall reflection varies between 714-787 mm (28.1-31.0 in.). This variance can be seen in the D-scan in Fig. 50 (far right image- the dark blue curved strip on the right of the figure), which shows the curvature of the tube's



**Fig. 50. First tile lining area tested, discovered by SPACETEC scanning**

skin. Also in Fig. 50 is a C-scan image of the area tested at a depth of 102 mm (4 in.) directly beneath the reinforcement. When compared to SPACETEC's infrared analysis, this outline correlates strongly with the infrared image. It appears that there is significant delamination at the level of reinforcement and above, and this has yet to cause debonding of the tile. The top left image in Fig. 50 shows much of the shallow surface cracks and possibly shallow delaminations above the reinforcement, the center left image depicts a deep crack (directly left of the last hoop rebar on the right). Notice the hoop and longitudinal reinforcement are both detectable at 122-239 mm (4.8-9.4 in.) below the surface at 297 mm (11.7 in.) o.c. (again, refer to the D-scan in Fig. 50 and the hoop reinforcement profile). The longitudinal reinforcement is seen but is hard to differentiate between actual longitudinal rebars and 51 mm-diameter (2 in.) electrical ducts that are present. If the scanning direction was changed, this distinction could be made.



The UST results from the second area tested (Fig. 49, right) are shown in Fig. 51. The region of debonded tile correlated greatly with a joint in the tube lining, as can also be supported by the extensive delamination noted mid-image in the B-scans (Fig. 51, left images). The backwall in this region varied from 635-762 mm (25.0-30.0 in.), due to the same reasons of tube curvature discussed in the previous map. The hoop reinforcement is 109-196 mm (4.3-7.7 in.) in depth, and approximately 307 mm (12.1 in.) o.c. As in the previous map, the longitudinal reinforcement is hard to distinguish from the 51 mm (2 in.) dia. electrical ducts present. It is suspected that the top left image is evidence of a lap splice (notice two distinct layers of steel rebar to the right of the joint, where different tube sections could have different splice locations). During the assembly of the tubes underwater, as noted beforehand, steel skins are connected by bolting and welding overlapped “hoods” (Kozel n.d.). After this mechanical lock connection is complete, concrete is poured surrounding the joint location to make the interior steel-reinforced concrete continuous and waterproof. Although no detailed plans

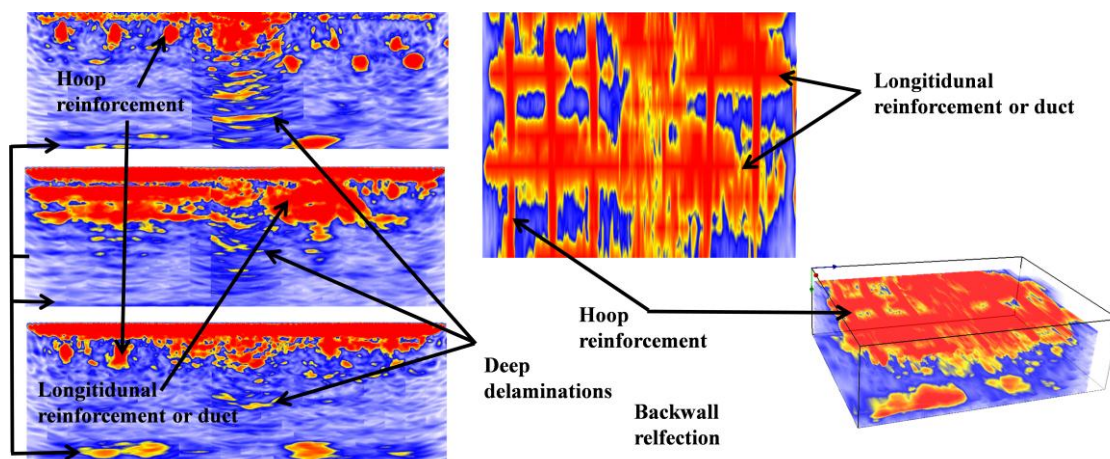


Fig. 51. Second tile lining area tested

show the width of this “scratch joint”, it remains a question as to whether the deep delaminations seen in the B-scans could be a result of degrading concrete joints.

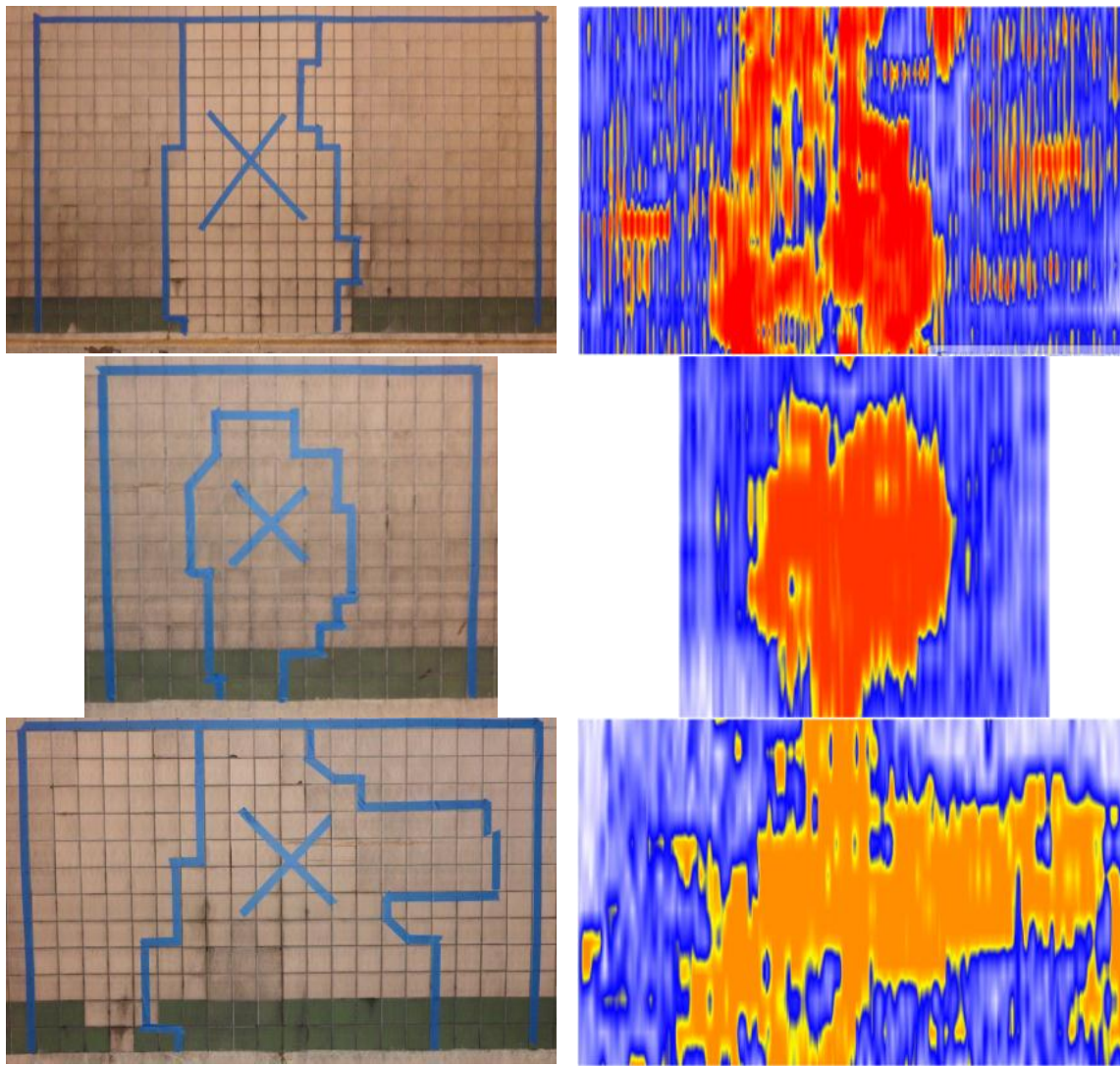
#### 4.4 Washburn Tunnel, TX

Washburn Tunnel (Fig. 52), the only underwater vehicle tunnel in operation in Texas, was completed in 1950 and carries Federal Road beneath the Houston Ship Channel joining two Houston suburbs. The tunnel was constructed via the immersed tube method, with sections joined together in a prepared trench, 26 m (85 ft) below water.

A specific area of interest in this tunnel was tile debonding. As noted earlier, in tile-lined tunnels such as these, acoustic sounding via hammer tapping can quickly reveal debonded tiles. As an object such as a hammer is lightly tapped (or even dragged) along the surface, the lower frequencies perceived by the ear as “pinging” is a typical



**Fig. 52. Washburn Tunnel: exterior (left, from [http://www.texasfreeway.com/houston/photos/around\\_houston/around\\_houston.shtml](http://www.texasfreeway.com/houston/photos/around_houston/around_houston.shtml)) and interior view (right)**



**Fig. 53. Tile linings via UST (left) paired with the associated C-scans (right)**

typical indication of debonding. Most debonding of tiles happens as water infiltrates the lining, deteriorating the mortar that holds the tile. However, trouble arises when trying to locate the source of the water infiltration; while hammer sounding is effective in locating debonded tiles, it does not necessarily locate the source of the water. In this tunnel, four areas were evaluated that indicated debonding through hammer sounding. Blue painter's

tape was used to outline both the grid and the outside perimeter of the area that the human ear perceived as a debonded section.

The first three sections are shown in Fig. 53. The images shown here have blue painters tape that outline debonded areas (by hammer sounding), and are paired with the associated C-scan that shows shallow delaminations ranging from 16 – 103 mm (0.63 – 4.1 in.) deep. It can be seen that the area marked off by hammer sounding closely matches the region of shallow debonding.

Representations of typical B-, C-, and Volume-scans for the three regions in Fig. 53 are shown below in Fig. 54. Again, large areas depicting shallow debonding are visible, as well as regions of delamination surrounding the reinforcement. It is clear from the B-scans that there exists significant damage that penetrates as deep as 457 mm (18 in.). These B- and C-scans are representative of the other areas tested in Washburn Tunnel, and the full reports can be found in Appendix A.

The last section tested, depicted in Fig. 55, reveals shallow debonding (note the C-scan image of the debonded area 16 mm, 0.63 in. below the surface in Fig. 55, bottom center). The B-scan (Fig. 51, bottom left) shows areas suspected to have deep delamination. This delamination is also seen in the Volume-scan on the right.

Overall, testing at Washburn Tunnel showed significant damage behind debonded tile that leads to the conclusion that the debonding is due to lining stresses (i.e., not due to tile workmanship).

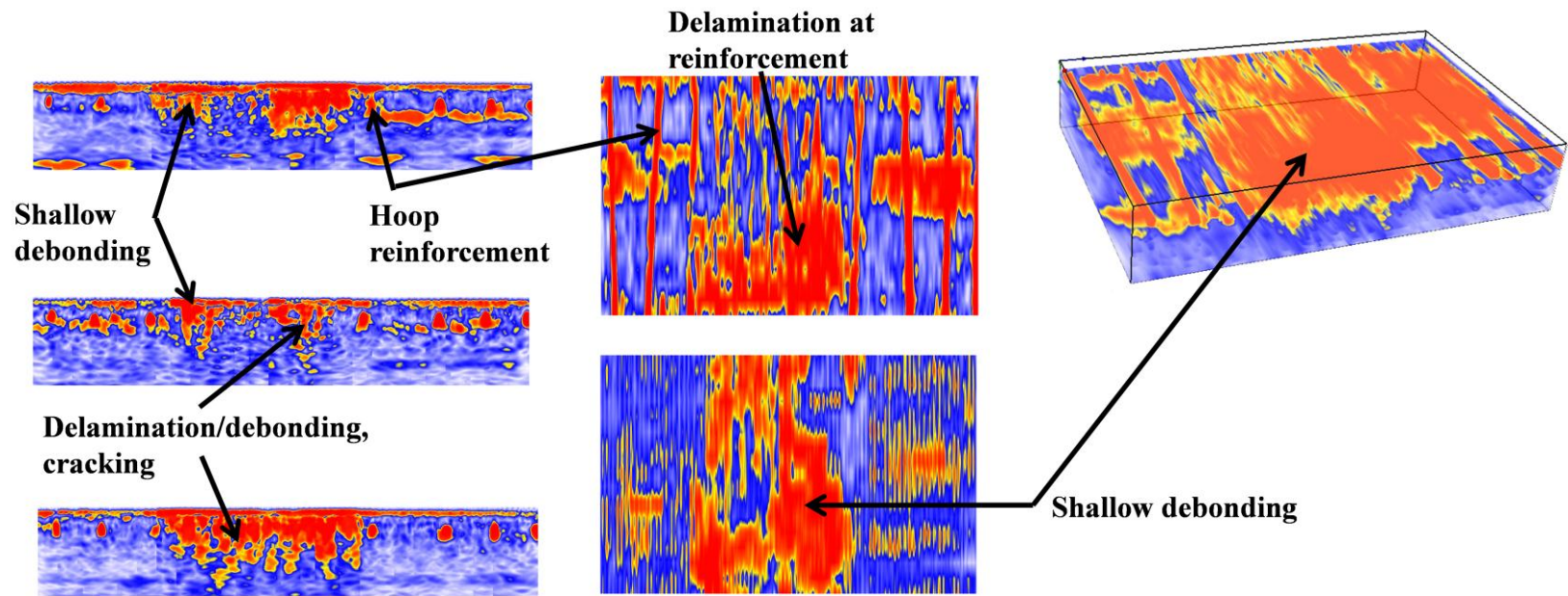


Fig. 54. Area tested surrounding debonded tiled: B-scans (left), C-scans (center), and Volume-scans (right)

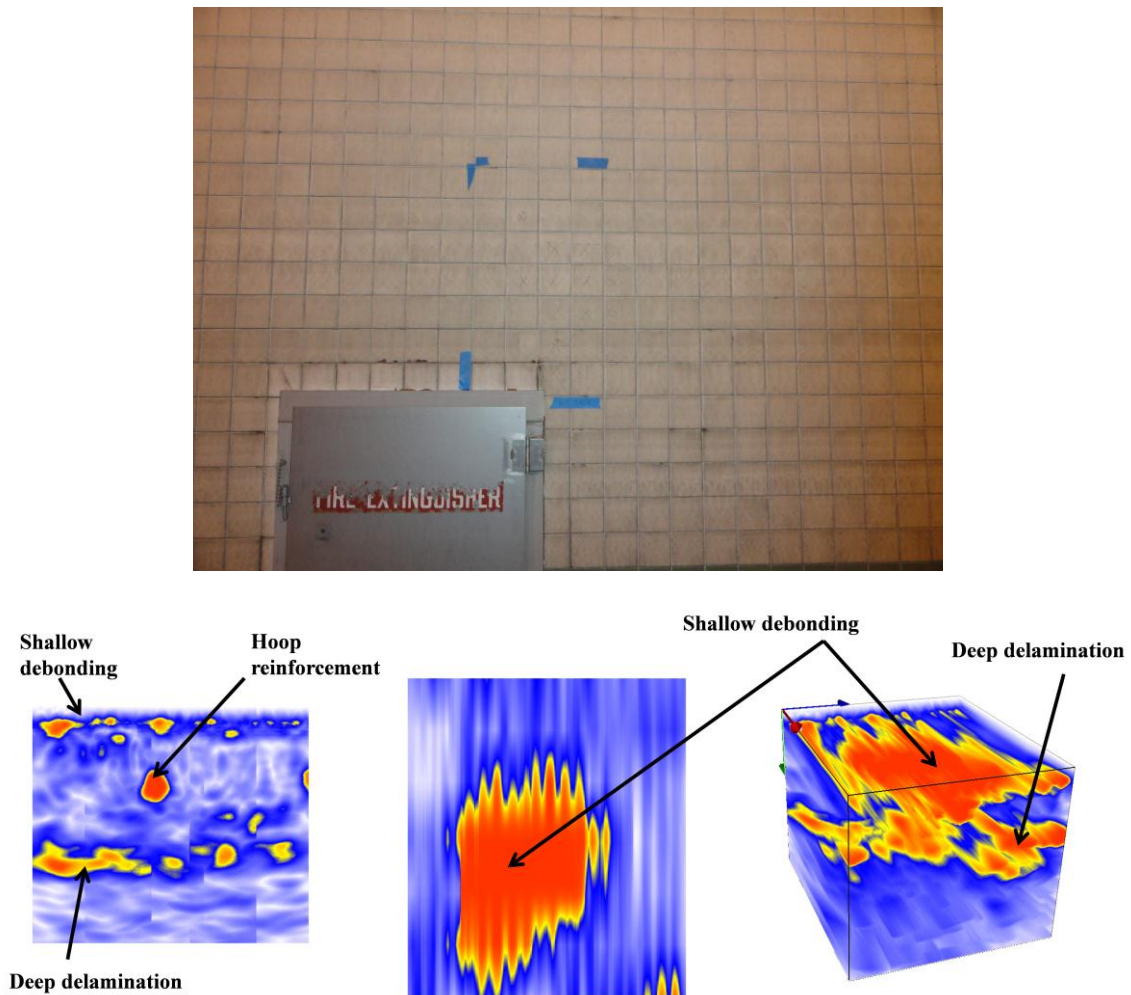


Fig. 55. Tile lining tested at Washburn Tunnel

#### 4.5 CRCP on Interstate 20 in Ft. Worth, TX

In the past few decades, Interstate 20 (Fig. 56) has had numerous repairs and overlays, including a section of CRCP in Ft. Worth, TX, west of RM 2871 (~ MP 426 + 0.5). A nominal 254 mm (10 in.) thick CRCP was constructed over a two-lift pavement, which consisted of a top layer of 51 mm (2 in.) asphalt base. Over a period of time, significant signs of distress began to appear. The ultrasonic tomography method was used to evaluate transverse surface cracks on the CRCP and determine the existence of



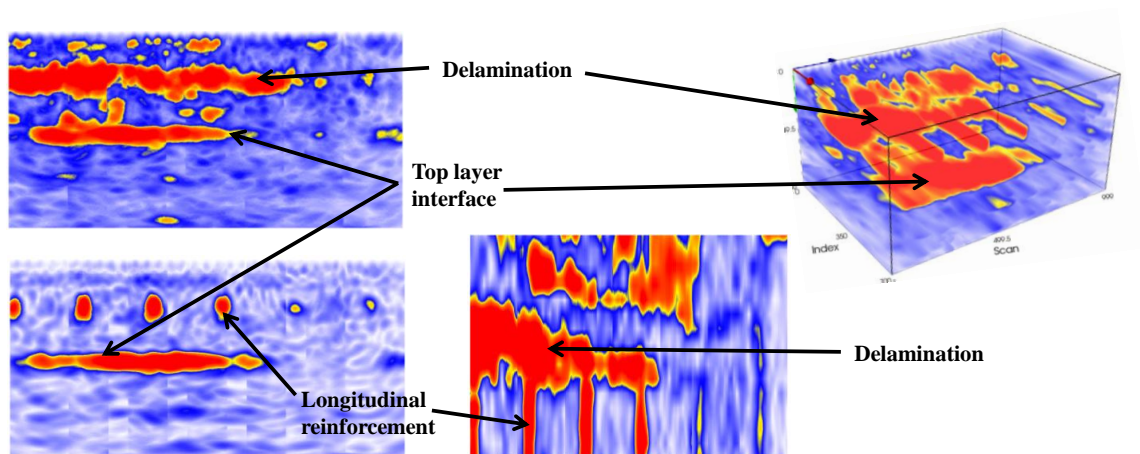
**Fig. 56. I-20 in Ft. Worth, TX**

any delamination within the overlay. The four areas tested are shown in Fig. 57. Each area was tested using a 50 mm x 150 mm (2 in. x 6 in.) grid. After scanning the section, cores were taken to verify the predicted overlay depth, reinforcement cover, and delamination depth.

The UST results of the first area tested (Fig. 57, top left), are shown in Fig. 58. These are typical B-, C-, and Volume-scans that are seen in the other scanned areas, and all full reports can be found in Appendix A. The two B-scans in Fig. 58 (left) show an area with delamination at the level of longitudinal reinforcement (top B-scan) and an area with no delamination, but a backwall reflection at the top layer interface



**Fig. 57. Four areas tested on I-20 in Ft. Worth, TX**

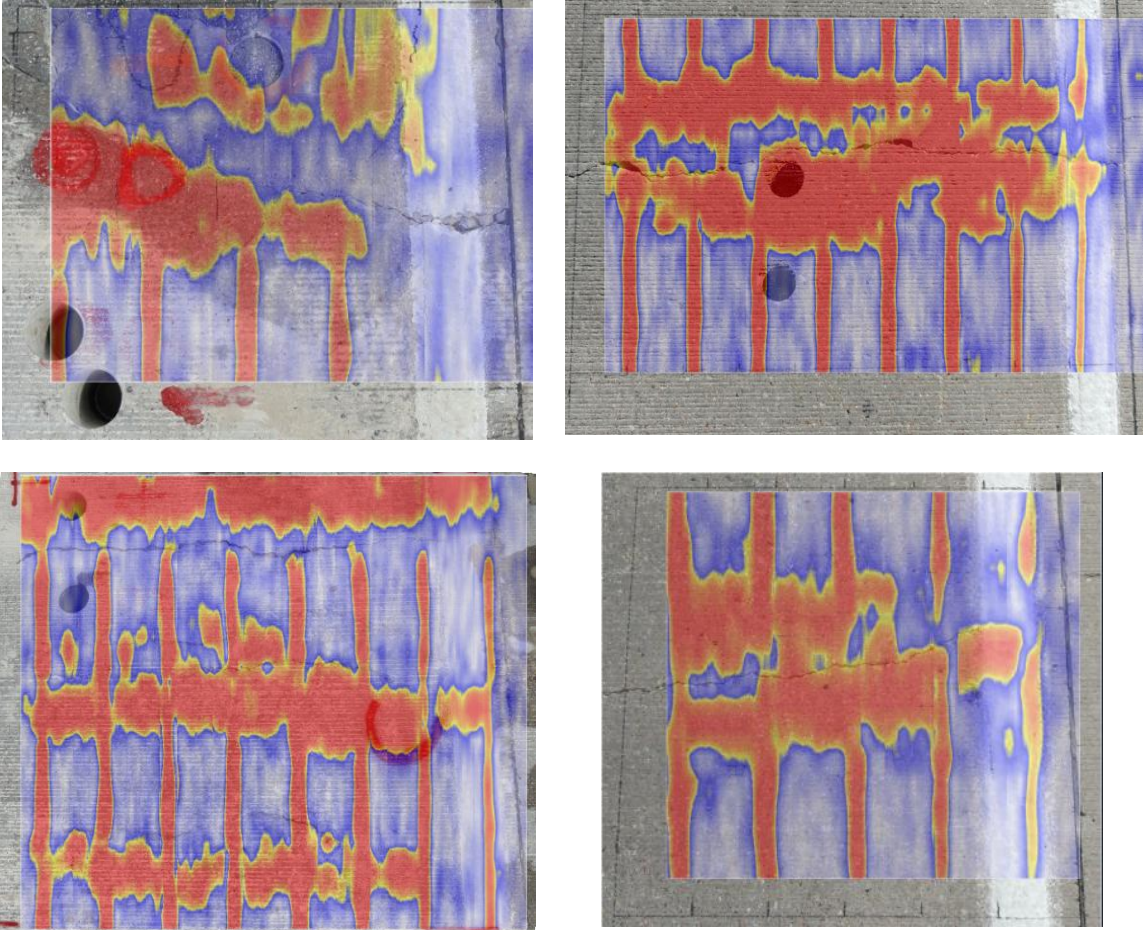


**Fig. 58. Typical UST results for I-20 scanning**

(bottom B-scan). The C-scan (Fig. 58, center) shows the width of the delamination at the level of reinforcement.

Fig. 59 below shows all four areas scanned with their appropriate C-scans overlaid on the image. All delaminations in these figures are at the level of reinforcement (see Tables 3-6 for details).





**Fig. 59. UST C-scans overlaid on I-20 images: Section A (top left), Section B (top right), Section C (bottom left), and Section D (bottom right)**

**Table 3. Section A, I-20 evaluations**

<b>Overlay</b>		
Tomograph		
Depth to delamination	Varies: 107 – 127 mm	
Depth to reinforcement	Varies: 117 – 127 mm	
<b>Core 1</b>		
	Tomograph	Core Results
Depth to asphalt sub-layer	264 mm	259 mm
Depth to delamination	None	None
Depth to reinforcement	127 mm	127 mm
<b>Core 2</b>		
	Tomograph	Core Results
Depth to asphalt sub-layer	254 mm	259 mm
Depth to delamination	None	None
Depth to reinforcement	None	None

**Table 4. Section B, I-20 evaluations**

<b>Overlay</b>		
Tomograph		
Depth to delamination	Varies: 114 – 135 mm	
Depth to reinforcement	Varies: 114 – 132 mm	
<b>Core 3</b>		
	Tomograph	Core Results
Depth to asphalt sub-layer	257 mm	264 mm
Depth to delamination	None	None
Depth to reinforcement	None	None
<b>Core 4</b>		
	Tomograph	Core Results
Depth to asphalt sub-layer	N/A	239 mm
Depth to delamination	117 mm	119 mm
Depth to reinforcement	None	None

**Table 5. Section C, I-20 evaluations**

Overlay		
Tomograph		
Depth to delamination	Varies: 117 – 130 mm	
Depth to reinforcement	Varies: 122 – 127 mm	
Core 5		
	Tomograph	Core Results
Depth to asphalt sub-layer	257 mm	259 mm
Depth to delamination	None	None
Depth to reinforcement	None	None
Core 6		
	Tomograph	Core Results
Depth to asphalt sub-layer	259 mm	259 mm
Depth to delamination	104 – 135 mm	137 mm
Depth to reinforcement	None	None

**Table 6. Section D, I-20 evaluations**

Overlay	
Tomograph	
Depth to delamination	Varies: 119 – 140 mm
Depth to reinforcement	Varies: 122 – 130 mm

As can be seen, UST predictions for delamination, pavement, and reinforcement depths closely matched with core measurements.

#### **4.6 George Bush Intercontinental Airport, Houston, TX**

A recent construction project at the George Bush Intercontinental Airport (IAH) in Houston, TX entailed overlaying existing runways with a nominal 203 mm (8 in.) jointed plain concrete pavement (Fig. 60). The existing runways were 762 mm (30 in.)

sections of concrete pavement: a 457 mm (18 in.) Portland cement concrete (PCC) layer over a 305 mm (12 in.) PCC layer. Within a period of three months, significant surface



**Fig. 60. Airport runway at IAH**

cracks on the bonded concrete overlay (BCO) instigated an evaluation on the source of these cracks. Using a grid spacing of 100 mm x 200 mm (4 in. x 7.9 in.), UST was used to completely scan two entire sections of the runway (two 7.6 m x 7.6 m, or 25 ft x 25 ft slabs) to evaluate the extent of damage present. The UST results are shown in Figs. 57 and 58. The first runway tested shows over 70 % of the area delaminated at the first layer interface (Fig. 61, C-scan at bottom right, Volume-scan at top right). The B-scans on the left of this figure show the first layer interface at 193-206 mm (7.6-8.1 in.) deep, the second layer interface at 683 mm (26.9 in.) deep, and the third layer interface at 958 mm (37.7 in.) deep. The second area tested shows approximately 15% of the total area

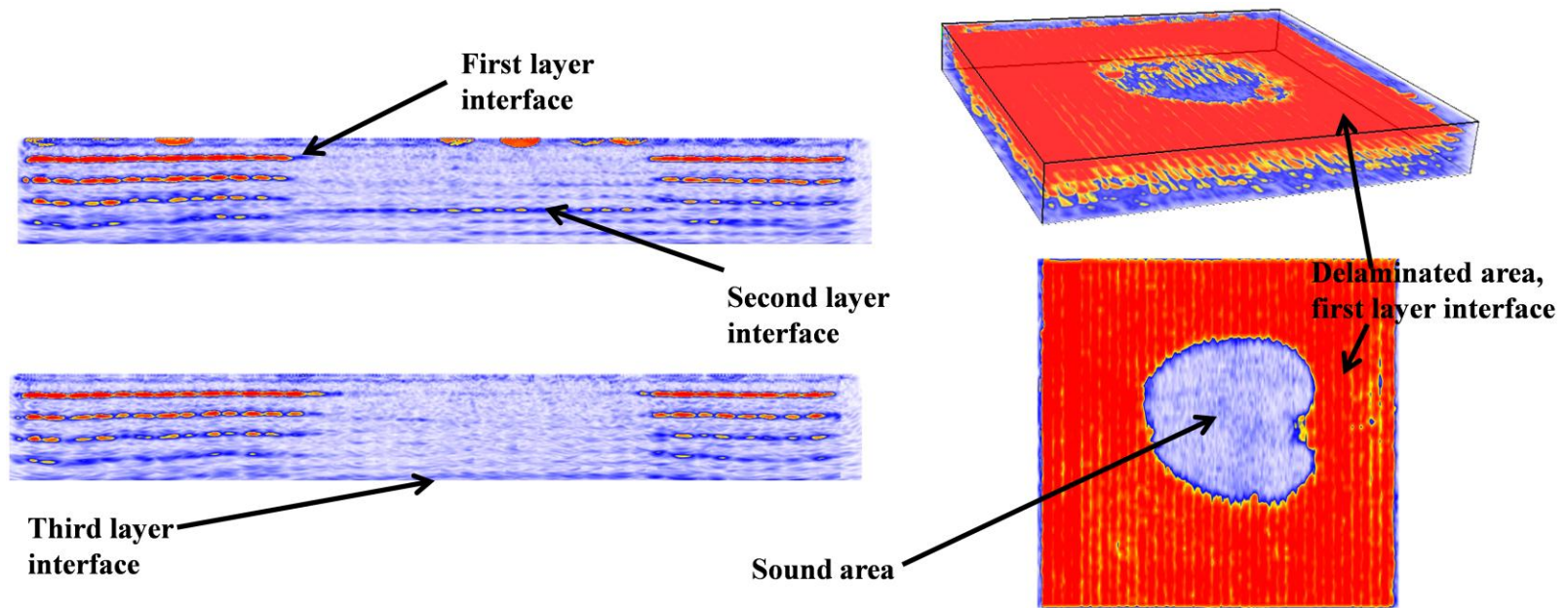


Fig. 61. First segment tested at IAH: B-scans (left), Volume-scan (top right), and C-scan (bottom right)

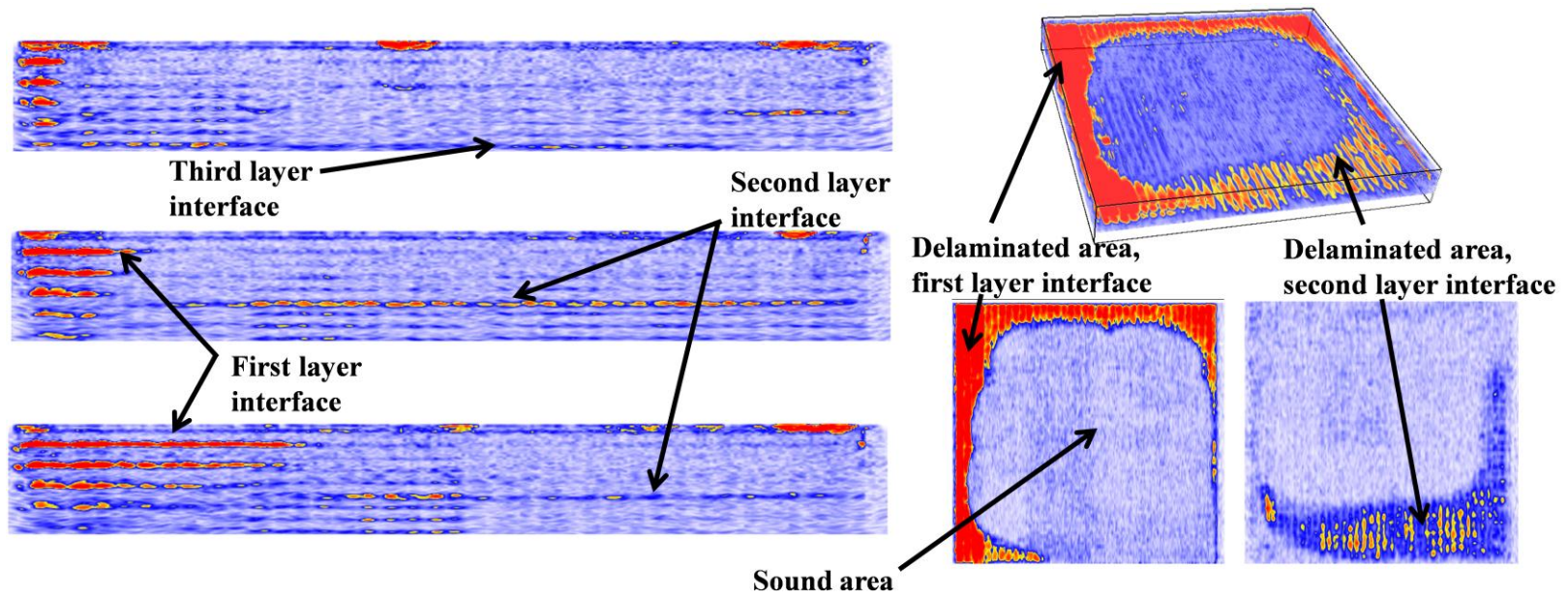


Fig. 62. Second segment tested at IAH: B-scans (left), Volume-scan (top right), and C-scans (bottom right)

debonded at the first layer interface (Fig. 61, C-scans at bottom right, Volume-scan at top right). It is also easy to see the partially bonded region at the second layer interface.

Cores were taken in both runway sections to verify the degree of bond based on three locations: where the UST results indicated (1) full bonding, (2) full debonding, and (3) an area in between. Three core strength testing locations within location 1 (predicted full bond) indicated tensile strengths ranged from 1230 Pa to 1500 Pa (178 psi to 219 psi). A core in location 2 (predicted partial bond) indicated a tensile strength of 131 Pa (19 psi). Finally, a couple of cores in location 3 (predicted full debond) confirmed delamination at the first layer interface.

## 5. DEVELOPMENT OF A METHODOLOGY FOR THE UST SYSTEM

### 5.1 Methodology Needs

In order to optimize the UST system, it is necessary to develop a testing process that is efficient and field-ready. Since the device used in this research can be used in two modes (the *Review* and *Map Modes*), it is necessary to determine which mode provides the best results for a given evaluation. The Review Mode is intended for single-point evaluations, where the internal structure of the concrete under the device is limited by the aperture of the focused array. This mode is quite successful in determining quick facts such as reinforcement depth, backwall reflections, and horizontal delaminations, particularly when the user has a sense of what type of discontinuity should be expected. The Map Mode, on the other hand, is used to create a grid of single-point evaluations that are then post-processed by computer software. Some of the specific needs for each mode use are outlined below, followed by Section 5.2, in which each need is addressed. Finally, Section 5.3 suggests a generalized testing procedure for using the A1040 MIRA system for evaluation of concrete specimens for both the Review and Map Modes.

#### 5.1.1 Review Mode and Needs

For the Review Mode, needs that will be address include:

- wave speed determination
- device orientation, or *y*-scanning direction
- locating a proper origin for ground truth comparison
- repeatability



The Review Mode has detection/interpretation limitations. Even though its operation can be much faster than building the necessary grids and data collection in the Map Mode, it is primarily convenient for (1) locating internal discontinuities that are previously identified or expected (i.e., reinforcement quantity and layout, or determining precise location of defect after discovery in Map Mode), or (2) getting a sense of easily established features such as concrete depth or the presence of horizontal delamination. If the device is used in Review Mode to determine the presence of unknown defects, great care should be taken to view the defect from many angles of orientation to verify the nature of the defect and specific lateral dimensions.

### ***5.1.2 Map Mode and Needs***

Using the Map Mode involves constructing a grid on the testing surface and using appropriate scanning increments to build a data map. This mode offers an advantage by building a map of single-point evaluations that can be constructed in such a way that each single-point evaluation overlaps another. This overlap increases resolution and offers a degree of repeatability, as each discontinuity that is highly repeatable stands out over random scatters. Appropriate software then reconstructs the dataset for 3D analysis in the laboratory.

When building a dataset in the Map Mode, the needs that should be addressed are as follows:

- wave speed determination
- device orientation, or *y*-scanning direction
- grid increment

- scanning depth
- creating a grid
- origin/boundary establishment; relation to computer model
- repeatability

## **5.2 Addressing the Needs for Operating in Map and Review Modes**

### ***5.2.1 Wave Speed Determination***

For both the Review and Map Modes, a wave speed determination has to be made. When in Review Mode, it is good practice to allow the system to automatically calculate the wave speed during each single-point evaluation. This will allow the user to determine if the calculated wave speed varies considerably between individual scans. Since the wave speed is calculated by comparing 66 transducer pairs and their measured pulse arrival times, any significant change in wave speed may be indicative of a change in concrete integrity or the presence of a discontinuity. In the Map Mode, it is recommended that the user first obtain 8-10 automated readings of the wave speed in Review Mode, and use the average of those readings as a fixed wave speed for use in the Map Mode. The assumption made in using an average wave speed instead of a point-by-point evaluation in wave speed is that the concrete is uniform in stiffness. This may not always be the case, but it allows for changes of medium within the concrete (steel, air, wood, etc.) to be consistent across the entire map.

### ***5.2.2 Device Orientation, or Y-Scanning Direction***

The y-scanning direction is defined to be the direction perpendicular to the B-scan and as such is relevant to the orientation of the device. When investigation by

Review Mode is chosen, the direction of orientation should be varied in order to investigate the lateral dimensions of the defect. When building maps, the choice of  $y$ -scanning direction is crucial and can vary depending on the type of discontinuity and where it is mostly suspected to be located in relation to other structural characteristics (i.e., reinforcement presence and direction). Generally speaking, horizontal delaminations and any type of void (including water-filled, air-filled, and volumes of foreign material such as clay lumps) can be viewed using an arbitrary  $y$ -scanning direction. These types of defects tend to have horizontal cross-sections with surface areas greater than half the wavelength of the penetrating acoustic wave. This makes detection assured from any angle. If particular dimensions are wanted, then multiple  $y$ -scanning directions are needed to assess the dimension in line with the device's natural polarization. To summarize, as long as the surface area encountered by the wave exceeds half of the wavelength in size in a plane *parallel* to the testing surface, the defect detection is largely irrelevant to testing direction. If internal discontinuities have a "thin" dimension (less than half the wavelength of the ultrasonic pulse, or typically 43-53 mm [1.7-2.1 in.] for shear wave speeds between 2000-2800 m/s [6562 ft/s or 9186 ft/s]) that is parallel to the polarization of the device, then detection of the discontinuity will be vaguely discernible at best. For instance, compare the resolution of the hoop and longitudinal reinforcement in the C-scan in Fig. 28. The  $y$ -scanning direction is in line with the hoop reinforcement, whereas the longitudinal reinforcement is much more vague due to the minimum  $y$ -scanning increment of 50 mm (2 in.) Vertical cracks are problematic for choosing a  $y$ -scanning direction since the width of the crack can go

undetected if the direction of the ultrasonic pulses is oriented parallel to the direction of the crack. For this reason, *y*-scanning in a direction that is parallel or 45-degrees from the general direction of the crack is recommended. It should be noted that cross-scanning (*y*-scanning in two directions perpendicular to each other) can be highly beneficial for evaluating the depth of vertical cracks. Data taken from the scans perpendicular to the crack direction can be initially examined to understand characteristics such as crack origination, depth, and contour. The cross-scan can then be utilized to verify the interpretation of the perpendicular scan. In this manner, micro delaminations that emanate perpendicular to the primary crack can be observed.

### ***5.2.3 Choosing Appropriate Grid Increments***

When using Map Mode to construct an array of data, it is necessary to determine an appropriate grid increment. An appropriate choice will consider the object of inspection's lateral size and depth. If measurements are not overlapped, the constructed images will be "spotted", or without full coverage. If a continuous image is desired for comprehensive defect dimensioning, overlap is strongly recommended. The transducer array has a limited aperture due to the combination of Snell's Law of refraction and superposition of acoustic waves. Snell's Law states the angle of incidence is equal to the angle of reflection for a given wave. By this law, an "undisturbed" ultrasonic pulse will always reflect from discontinuities located half the distance from a transducer pair. However, the modified synthetic focusing technique used in the software image reconstruction utilizes repeated signals to develop the colored output. This means that the signal strength (as observed by the color output of the MIRA scans) representing a

given discontinuity's width (in the  $x$ -scanning direction) will vary in signal strength depending on how close it is to the center of the focused aperture. The goal in continuous mapping then becomes to overlap in such a manner that critical planes of inspection are fully covered by a large number of transducer beams. Therefore, closely-spaced scanning increments will better suit defects such as small voids, clay lumps, and early propagation of small cracks, whereas general slab thickness can be estimated from very widely-spaced scanning increments. Table 7 suggests scanning increments for generating a 3D map for defect analysis. These suggestions are experimentally determined based on defects within 305 mm (12 in.) of the surface.

**Table 7. Recommended scanning directions and grid spacing**

<b>TYPE OF DISCONTINUITY</b>	<b>Y-SCANNING DIRECTION</b>	<b>RECOMMENDED GRID SPACING (Y vs X)</b>
Voids with diameter < 50 mm (air and water-filled)	Any orientation	Maximum of 50 mm x 150 mm
Voids with diameter > 50 mm (air and water-filled)	Any orientation	Minimum of 50 mm x 150 mm
Horizontal delaminations	Any orientation	Optimal: 50 mm x 150 mm to 100 mm x 200 mm
Vertical cracks	Parallel to surface crack direction	No greater than 50 mm x 100
Clay lumps < 150 mm	Any orientation	Maximum of 50 mm x 150 mm
Clay lumps > 150 mm	Any direction	Minimum of 50 mm x 150 mm
Reinforcement detail in one direction	Perpendicular to reinforcement layout	Optimal: 50 mm x 150 mm to 100 mm x 250 mm
Reinforcement detail in two directions	45° from reinforcement direction	Optimal: 50 mm x 150 mm
Slab thickness	Any direction	Maximum of 100 mm x 200 mm

#### ***5.2.4 Scanning Depth, or Z-Scanning Direction***

Choosing an appropriate scanning depth ( $z$ -scanning direction) is an important decision when choosing to build a 3D data set in both Review and Map Mode. If the

chosen depth is too shallow, it might be that critical information regarding the depth of structure details is omitted. If the z-scanning depth is set too deep, the resolution of shallow structural details is diminished. An appropriate z-scanning depth should be chosen after multiple inspections via the Review Mode. When the operator has obtained a feel for structural characteristics that should be included in the map, a depth should be chosen that slightly exceeds the lowest element needed to be captured. An example would be an analysis on concrete pavements, where the operator is asked to build a map for analyzing possible delamination at any depth within the overlay. In this case, it would be recommended that the depth be set to only capture the depth of the overlay. This minimizes unnecessary data and improves resolution for delamination detection. On the other hand, if the operator is to generate a map for an analysis of bonding between a top layer and a sublayer, it would be advisable to choose a minimum z-scan depth that exceeded at least twice the depth of the overlay. This is due to the fact that bonds that have fully separated will produce backwall “multiples”, or echoes, which are repeated backwall reflections at multiples of the initial layer depth. This feature is caused by the nearly elastic reflection of the acoustic waves as they encounter the concrete-air original interface. The presence and intensity of such echoes can depict the severity of debonding. If little or no echoes are present, but instead a weak signal at the top layer/sublayer interface is present, then this can depict a loss of strength or a partially-bonded interface. If no interface is detected at all, then a fully bonded pavement at that location can be expected.

### ***5.2.5 Constructing a Grid***

For the UST system to operate in Map Mode, it is necessary to construct an accurate grid or marking system to fully characterize the specimen under evaluation. The creation of a grid can be one of the most critical jobs when building a map with the tomograph. Every grid must be square and accurate in order to utilize the map for noting precise areas of interest.

There are two methods of grid construction that are recommended here. The first method is by constructing chalk lines that outline the area to be tested, including the interior grid spacing. It is recommended to use white or blue chalk lines when it is desirable to have a removable grid, while more permanent grids can be established using red or black chalk. The creation of the grid starts with generating a right angle that extends a minimum of half the length of the tomograph past the outer boundary of the desired testing surface in the  $x$ -scanning direction and half the width of the tomograph past the outer boundary of the desired testing surface in the  $y$ -scanning direction. The first side of the right angle can be made by popping a chalk line that is visually approximated as in line with the desired direction of scanning. The second side of the right angle can be projected by using a square or by using a measuring tape to establish a point corresponding to a 3-4-5 triangle. Once the second side of the right angle is popped, it is necessary to mark the  $x$ - and  $y$ -scanning increments on the appropriate sides of both right angle projections. It should be noted that welder's chalk is an excellent marking tool, as it is highly durable on concrete surfaces, yet removal is possible with water. Once the length and width of the grid has been marked off, it is

necessary to use a measuring tape to finish marking the perimeter of the inspection area by projecting the ends of the right angle's sides by the appropriate distance to establish the corner opposite the origin. Increments can then be marked along these sides, and the interior  $x$ - and  $y$ -scanning direction gridlines can be popped via chalk lines. When the scanning begins, it will only be necessary to place the light from the corner of the device on the crosshairs of the incremented grid.

The second, albeit more permanent, method for grid placement involves constructing a grid template from a thin sheet of plywood or particle board (3.2 mm or 0.125 in. MDF was used in this study). A section of sheet can be as long and wide as is appropriate for the size of the area under investigation. After cutting the sheet (which is typically purchased in 1.2 m x 2.4 m, or 4 ft. x 8 ft. stock) down to the desired size,



**Fig. 63. Gridlines using grid template**



incremental rips should be made using a table saw. The “slots” cut by the table saw should begin within 100 mm (4 in.) of the sheet’s edge and proceed to 100 mm from the sheet’s opposite edge (the grid established by this method is shown in Fig. 49).

Using this sheet as a template for the grid spacing, it should be placed on the testing surface in the direction of the desired  $y$ -scanning direction. It is recommended to use landscaping paint to mark the slotted areas. This process can be repeated for the  $x$ -scanning direction by placing the grid template square with the previously-marked grid by aligning the outside of the sheet with the marked  $y$ -scanning grid lines.

#### ***5.2.6 Origin/Boundary Establishment; Relation to Computer Model***

Due to the aperture of the transducer array, actual discontinuities discovered by the 3D analysis cannot be referenced from the established origin. The width of the ultrasonic tomograms are dependent on the size of the grid spacing and  $z$ -scanning depth and must be superimposed on the physical grid to determine with certainty the location of a particular defect. The process for establishing the relationship between the computer model’s origin and the grid’s origin is described here.

After the data from each successive increment has been gathered and downloaded to the remote computer, the 3D model analysis program will allow measurements to be made relative to the device’s aperture. Unfortunately, this aperture can be less than or greater than the created grid depending on the scanning depth. To be able to relate the origin of the physical specimen (denoted as  $\{0, 0\}_0$ ) to the origin on the analysis software (denoted as  $\{0, 0\}_1$ ), the relationship between origins must be developed. To establish this relationship, several terms must be defined as follows:

$X_0$ , the total  $x$ -offset between  $\{0,0\}_0$  and  $\{0,0\}_1$ , taken as positive in the  $x$ -scanning direction

$Y_0$ , the total  $y$ -offset between  $\{0,0\}_0$  and  $\{0,0\}_1$ , taken as positive in the  $y$ -scanning direction

$X_1$ , the chosen  $x$ -scanning increment

$Y_1$ , the chosen  $y$ -scanning increment

$W_0$ , the width of the tomograph array in the  $x$ -scanning direction, measured from outside transducer to outside transducer (330 mm, or 13 in. for the A1040 MIRA)

$L_0$ , the length of the tomograph array in the  $y$ -scanning direction, measured from outside transducer to outside transducer (90 mm, or 3.5 in. for the A1040 MIRA)

$W_1$ , the distance in the  $x$ -scanning direction from the lead LED guide to the nearest transducer (10 mm, or 0.4 in. for the A1040 MIRA)

$L_1$ , the distance in the  $y$ -scanning direction from the lead LED guide to the nearest transducer (10 mm, or 0.4 in. for the A1040 MIRA)

$W_3$ , the total width of a single B-scan as can be seen from the Review or Map Modes

Using the definitions defined above, the physical location of the 3D image's origin ( $\{0, 0\}_1$ ) relative to the origin of the grid on the specimen ( $\{0, 0\}_0$ ) is defined by

$$X_0 = (W_1 + \frac{W_0}{2}) - \frac{W_3}{2}$$

and,

$$Y_0 = L_1 + \frac{L_0}{2}$$

Or for the MIRA system (in mm),

$$X_{0-MIRA} = (175) - \frac{W_3}{2}$$

and,

$$Y_{0-MIRA} = 55$$

Again, positive values are taken to be in the  $x$ - and  $y$ -scanning directions. After establishing this origin ( $\{0, 0\}_1$ ) on the specimen, all  $x$ - and  $y$ -dimensions taken directly from the 3D software can be measured from this point of reference.

In the field applications from Section 4, the offset typically varied from 100 mm (2 in.) inside the specimen grid to 406 mm (16 in.) outside the specimen grid. If this scale of accuracy is not required for the particular type of evaluation (say the inspector is only interested in a nominal layer depth), the defect location can be estimated using the direct measurements from the analysis software, then pinpointed by using the device in Review Mode. Whether or not great accuracy is necessary, using the Review Mode to fine tune the final location can help to confidently establish the defect location.

### ***5.2.7 Repeatability***

A reliability assessment of the device would not be complete without discussing repeatability. Although system repeatability was not explored greatly in Section 3, it was discovered that all repeated scans (different days and outside temperatures, same operator, same grid) indicated remarkable agreement.

The specific reason repeatability was not emphasized in this study is that the UST device used in this study has inherent repeatability features. The color palette shown in the UST images, although specified as intensity, is merely created by the repeated incidences of wave reflection on a boundary. Therefore, if a discontinuity is seen in two overlapping B-scans, repeatability is already established to a certain extent. The system should be analyzed for reproducibility and repeatability, but this topic is beyond the scope of this research. More on repeatability can be seen in Section 6.3.

### **5.3 General Testing Procedures**

The following procedures have been developed and modified based on hundreds of evaluations with the A1040 MIRA system. As all case studies will be different, it is necessary to adapt testing procedures to fit the needs of the evaluation specific to the location, type of surface, type of construction, and primary defects under consideration.

#### ***5.3.1 Review Mode Testing Procedures***

*Step 1: Determine wave speed.* In Review Mode, there are two options for wave speed determination. One option is to use the automatic wave speed generated per scan without inputting a constant wave speed. The benefit of this approach is the user can see the variation of wave speed throughout the object of inspection. In areas of deterioration or significant defects, the automatic wave speed decreases due to path lengthening of the acoustic pulse. The second option is to take a sample of wave speeds and use the average as a manual input. This approach allows discontinuity details to be measured accurately since the wave speed is fixed for the concrete medium. This is done by first setting the wave speed control to automatically collect the wave speed per individual scan. It is then

necessary to collect 8-10 scans in areas free of surface deterioration or severe unevenness. Attempt to collect the wave speed in locations where reinforcement and other shallow discontinuities will not affect the measurements. This can be done by viewing the B-scans and attempting to measure in between reinforcement layout, if any is present. After collecting the scans, use the numeric average of the wave speeds and manually set the wave speed control to this velocity.

*Step 2: Set Z-scanning depth.* Based on the discussion in Section 5.2.4, determine the appropriate Z-scanning depth.

*Step 3: Begin scanning.* To collect the data, fully press the system to the surface very firmly, and press the collect trigger. Wait until the red status bar has gone to green before orienting the device on the next location. It is suggested to use welder's chalk when scanning to mark on the surface when the B-scan depicts an interesting feature. Note that the variety of parameters included in the main control can be altered, including color and analog gain, time delay, number of periods, time corrected gain, frequency, etc. It is suggested to keep these values at their default settings unless there is a way to calibrate the device for the object of inspection. If a known discontinuity is available for calibration, the appropriate settings can be altered to fine tune the measurements. Note that shear wave frequency can be varied from 25-85 kHz, so that smaller and more shallow defects can be seen at the expense of wave attenuation.

### ***5.3.2 Map Mode Testing Procedures***

*Step 1: Determine grid increments and scanning direction.* Referring to the discussions in Sections 5.2.3 and 5.2.5, along with Table 7, determine the size of the desired grid

based on the object of inspection. If no known discontinuities are apparent, it is suggested to take numerous scans in Review Mode to determine possible target defects.

*Step 2: Establish a grid.* Using either of the techniques described in Section 5.2.5 or any other method that accurately projects a scanning grid, mark the specimen in the proper direction and the proper increments established in Step 1.

*Step 3: Set X, Y, Z-scanning depths.* Again referring to the discussions in Section 5.2.3 and 5.2.4, input the stepping scans and depths.

*Step 4: Begin scanning.* To scan with the system, place the beam of light from the underside of the array on the origin, using the other light beams to visually square the device relative to the grid. Using the origin established when making a grid as a starting point, begin collecting data in either the  $x$ - or  $y$ -scanning direction. Either direction can be used for data collection, but it is advisable to keep the data sets as “square” as possible. If datasets are too long and narrow, the analysis software has difficulty computing the SAFT reconstruction algorithm due to the lack of neighboring scans for wave superposition. For example, if a specimen to be tested requires a 5 x 30 element grid, it would be advisable to begin either going back and forth along the shorter 5 elements, or scan in two sets of manageable 5 x 15 grids. By this approach, if data collection is interrupted, the dataset will be less likely to encounter difficulty during 3D reconstruction. To collect the data, fully press the system to the surface very firmly, and press the collect trigger. Wait until the red status bar has gone to green before orienting the device on the next location. It is suggested to use welder’s chalk when scanning to mark on the surface when the B-scan depicts an interesting feature.

*Step 5: Transfer dataset and process.* Using the appropriate cables, transfer the dataset from the system to a computer with the proprietary software. Analysis can take place immediately after the dataset has been downloaded, often allowing an analysis to be started in the field. Record all typical features of interest, including backwall reflection, depth to reinforcement, width of apparent discontinuities, etc., for future reference. It is recommended to start with a Volume-scan in order to get a glimpse of the global element, then to comb through each B-, C-, and D-scans for irregularities. The color gain dial allows the relative intensities to be decreased in order to visualize slighter changes in impedance. Note that depths to discontinuities are taken as distance to the center of the reflectivity cloud.

*Step 6: Locate areas of interest on physical grid.* Once areas of significance have been located and dimensioned and ground truth verification is desired, use the offsets established in Section 5.2.6 to mark the areas accurately on the physical specimen.

## 6. CONCLUSIONS AND RECOMMENDATIONS

### 6.1 Conclusions

The UST system was used to evaluate a variety of simulated defects in concrete and shotcrete constructed specimens that included: air- and water-filled voids, vertical cracks, horizontal delaminations, and abnormalities such as clay lumps. The device was also used to determine reinforcement depth and spacing, as well as concrete thickness measurements. After evaluating the system's capabilities and establishing confidence in the used methodology, the system was used on six existing structures. Where able, ground truth data was further used to determine the precision and accuracy of the system. Table 8 shows the maximum and minimum features detected by this research. Note that these values do not necessarily express the limits of the device, but the limits of the performed research. Further research needs include expanding the variety of structural defects (both size and location) to determine maximum and minimum detectable features along with confidence levels for each type of defect.

The UST device was discovered to be exceptional at locating horizontal delaminations and could even differentiate between fully debonded and partially bonded areas. Backwall surfaces, up to a depth of 711 mm (28 in.), were successfully and accurately located. Both air- and water-filled voids could be detected and even differentiated by looking for shadowing under the defect. Since water, an incompressible fluid, cannot sustain shear waves, the US pulses are not transmitted past water-filled regions, and typically, only the initial boundary is reflected. Reinforcement layout and



depth, as long as the device is polarized in the correct direction, was also successfully determined, with the only exception being in some shotcrete applications. When very porous materials such as the shotcrete specimens were evaluated, the natural inclusion of voids made internal inspection very difficult. With the exception of medium-sized clay lumps surrounding reinforcement, all clay lumps tested were also highly successful.

**Table 8: Maximum and minimum detected features tested by the A1040 MIRA system. Note that all testing here reported with 50 kHz scanning frequency**

<b>Component Detected</b>	<b>Component Extremes</b>	<b>Minimum Depth Detected</b>	<b>Maximum Depth Detected</b>
<i>*Reinf. diameter</i>	Min. diameter: #5	83 mm (to center)	184 mm (to center)
	Max. diameter: #11	51 mm (to center)	196 mm (to center)
<i>Reinf. cover</i>	N/A	#11 @ 33 mm	#9 @ 377 mm
<i>Secondary reinf. layer</i>	Min. diameter: #5	184 mm (to center)	184 mm (to center)
	Max. diameter: #9	210 mm (to center)	377 mm (to center)
<i>*Delamination thickness</i>	Min. thickness: 0.05 mm	43 mm (to center)	89 mm (to center)
	Max. thickness: 2.0 mm	69 mm (to center)	69 mm (to center)
<i>Delamination depth</i>	N/A	0.05 mm thickness @ 43 mm depth (to center)	0.25 mm thickness @ 183 mm depth (to center)
<i>Clay lump diameter (all 51 mm thick)</i>	Min. diameter: 102 mm	61 mm (to center)	216 mm (to center)
	Max. diameter: 152 mm	107 mm (to center)	160 mm (to center)
<i>Specimen thickness (structural depth)</i>	N/A	102 mm	711 mm
<i>Air-filled voids</i>	Only thickness tested: 13 mm	76 mm (to center)	203 mm (to center)
<i>Water-filled voids</i>	Water-filled Ziploc bag: ~ 13 mm	76 mm (to center)	203 mm (to center)

**\* Size only verified by ground truth data; feature not detectable by the A1040 MIRA system**

## 6.2 Limitations of the UST System

The limitations of the device are as follows:

- *Speed of data acquisition.* If the system is used for detailed mapping in the Map Mode, the user should expect the scanning process to take between 9-

25 min/m<sup>2</sup> (0.8-2.3 min/ft<sup>2</sup>) The Review Mode can be used for single-point evaluations at much faster rates of inspection (3-5 seconds per scan), but only limited-width B-scans are available for evaluation in this mode.

- *No indication of phase change.* The color palette response represents quantity of reflectivity regions and is a measurement relative to the medium (in which there should ideally exist zero reflectivity, the *blue* spectrum). As such, the type of defect is largely guess-work on the end of the user and requires greater skill and knowledge of ultrasonics to interpret these signals.
- *Detection of layered defects.* If defects are “stacked”, particularly in such a manner that air gaps are located above other types of defects, then the device can rarely determine anything below the initial air-filled gaps. This is due to ultrasonic pulse attenuation at air boundaries. If pulses are capable of being transmitted past air interfaces, then the received signal is extremely weak and should be examined to be certain it is not a multiple or echo of the initial flaw.
- *Shallow defects.* Due to the spacing of the transducer array and the beam spread of the individual transducers, defects that exist approximately 25 mm (1 in.) from the surface cannot be expected to be received by other transducers and carry any accurate information regarding the depth and lateral dimensions of the shallow defects. However, near surface defects can leave a “shadow” on the data collected below the near-surface defects. An example of this is the shotcrete Specimen L and concrete Specimen Iota,

where the defect leaves a shadow beneath its presence. Though it is too shallow to reflect the actual boundary, its presence inhibits ultrasonic pulses to be transmitted (or received) beyond it.

### **6.3 Recommendations for Future Research**

The author recommends the following considerations for future improvements in ultrasonic tomography:

- *Incorporating material phase change output.* Direct information regarding phase changes within the medium would be a great improvement for UST. The received pulse's phase change would indicate to the operator the type of discontinuity (hard or soft), and would be used help identify the type of material and/or bond, if the material type is already known.
- *Two-way polarization.* One drawback of the system is the natural polarization of the device. A technique that could be investigated would involve superimposing data taken from two angles of data collection for 3D analysis. Two-way polarization in any form would add a much-needed perspective to the ultrasonic images.
- *Rotating system.* Any ground-coupled form of the ultrasonic technique as it is used and understood today will inevitably face critique concerning time effectiveness. One possible solution is the introduction of a rotating array. For example, if eight panels of transducers, each containing a phased-array module such as the MIRA system, were constructed in an octagonal manner and rotated about an axle, such a device could be "rolled" over areas of

inspection. The cost of such a system would be very high due to the number of transducers, but would not likely be cost-prohibitive when taking into account the time saved for data acquisition.

- *Probability of Detection (POD) assessment*

This thesis uses a performance demonstrated approach to evaluate the UST system. To complete a thorough investigation, POD assessments should be made for specific types of defects. To establish a POD curve, numerous tests need to be performed varying only the thickness of the discontinuities. Such tests should be carried out on delaminations ranging from hairline fractures to complete separation, reinforcing steel of various sizes, etc.

- *Other structural elements to be tested*

Other structural elements that should be evaluated include asphalt pavements, tendon voids in post and pre-stressed elements, and structural elements with developed alkali-silica reaction, delayed ettringite formation, and advanced corrosion.

- *Automated detection software*

As the UST systems and other highly resolute systems are developed, automated detection software should be developed that allows massive amounts of data to be sorted. This software should take into account UST intensity readings as well as phase changes of the material.

- *Modifications for shallow defects, cracks*

The UST technique needs to be modified for detection of shallow (less than 1 in. from the surface) delaminations. This may be accomplished by introducing a scanning medium, such as a low impedance elastic polymer, that allows the system to scan a distance from the evaluation surface. Vertical crack details, which tend to be largely overlooked due to the orientation of the transducer pairs, could be examined by using the same phased-array structure of the A1040 MIRA system, but allowing the signals to be received for long periods of time (~10 ms). In this manner, it may be possible to use one-sided coda wave interferometry to quantify shallow crack detail based on the amount of shallow scatterers (Shokouhi et al. 2010).

## REFERENCES

- Acoustic Control Systems (n.d.). "MIRA- Ultrasonic Tomograph for Imaging of Concrete Structures."  
 <[http://acsys.ru/eng/production/?type\\_id=16&subtype\\_id=7&product\\_id=23](http://acsys.ru/eng/production/?type_id=16&subtype_id=7&product_id=23) >  
 (December, 2011).
- Brennan, R. (2007). "Ultrasonic nondestructive evaluation of armor ceramics." Ph.D. dissertation, Rutgers, The State University of New Jersey, New Brunswick, NJ.
- Celaya, M., Nazarian, S., Chetana, R., and Von Quintus, H. (2010). "Delamination Detection of HMA Airport Pavements with NDT Devices." *Proc., 2010 FAA Worldwide Airport Technology Transfer Conference*. Federal Aviation Administration (FAA), Atlantic City, NJ.
- De La Haza, A., Peterson, C., and Samokrutov, A. (n.d.). "Three Dimensional Imaging of Concrete Structures Using Ultrasonic Shear Waves." *ACS*  
 <[http://acsys.ru/eng/article/files/Imaging\\_of\\_concrete\\_structures.pdf](http://acsys.ru/eng/article/files/Imaging_of_concrete_structures.pdf)>  
 (December, 2011).
- Desch, E., Sproule, D., and Dawson, W. (1946). "The detection of cracks in steel by means of supersonic waves." *J. Iron Steel Inst.*, 153, 319-352.
- Elsener, B., Andrade, C., Gulikers, J., Polder, R., and Raupach, M. (2003). "Half-cell potential measurements- Potential mapping on reinforced concrete structures." *Materials and Structures*, 36(7), 461-471.
- Federal Highway Administration (FHWA) (2001). "Highway Bridge Inspection: State-of-the-Practice Survey." *FHWA-RD-01-033*, Washington, DC.
- Federal Highway Administration (FHWA) (2005). "Highway & Rail Transit Tunnel Maintenance & Rehabilitation Manual." *FHWA-IF-05-017*, Washington, DC.
- Firestone, F. (1942). "Flaw Detecting Device and Measuring Instrument." *US-Patent 2 280 226*. Filed May 27, 1940, and issued April 21, 1942.
- Firestone, F. (1946). "Refinements in Supersonic Reflectoscopy. Polarized Sound." *J. Acoust. Soc. Am.*, 18(1), 200-211.
- FLIR (n.d.). "FLIR T-Series Infrared Cameras."  
 <<http://www.flir.com/thermography/americas/us/view/?id=44804> > (February, 2012).

- Im, S., Hurlbauss, S., and Trejo, D. (2010). "Inspection of Voids in External Tendons of Posttensioned Bridges." *Transportation Research Record: Journal of the Transportation Research Board*, Transportation Research Board of the National Academies, Washington, DC, 2172, 115–122.
- International Atomic Energy Agency (IAEA) (2002). "Guidebook on non-destructive testing of concrete structures." IAEA-TCS-27, Vienna, Austria.
- Iyer, S., Schokker, A., and Sinha, S. (2003). "Ultrasonic C-Scan Imaging: Preliminary Evaluation for Corrosion and Void Detection in Posttensioned Tendons." *Transportation Research Record: Journal of the Transportation Research Board*, Transportation Research Board of the National Academies, Washington, DC, 1827, 44-52.
- Kozel, S. (1997). "Highway and Transportation History Website." <<http://roadstothefuture.com/main.html>> (February, 2012).
- Krause, M., Bärmann, M., Frielinghaus, R., Kretzschmar, F., Kroggel, O., Langenberg, K., Maierhofer, C., Müller, W., Neisecke, J., Schickert, M., Schmitz, V., Wiggenhauser, H., and Wollbold, F. (1997). "Comparison of pulse-echo methods for testing concrete." *NDT&E International*, 30(4), 195-204.
- Krause, M., Gräfe, B., Mielentz, F., Milmann, B., Friese, M., and Wiggenhauser, H. (2009). "Ultrasonic imaging of post-tensioned concrete elements: New techniques for reliable localization of grouting defects." *Proc., 2<sup>nd</sup> International Conference on Concrete Repair, Rehabilitation and Retrofitting*, Concrete Repair, Rehabilitation, and Retrofitting II, Cape Town, South Africa, 215-216.
- Schickert, M. (1995). "Towards SAFT-Imaging in Ultrasonic Inspection of Concrete." *Proc., International Symposium on Non-destructive Testing in Civil Engineering*, NDT-CE, Berlin, Germany, 1, 411-418.
- Schickert, M., Krause, M., and Muller, W. (2003). "Ultrasonic Imaging of Concrete Elements Using Reconstruction by Synthetic Aperture Focusing Technique." *J. Mater. Civ. Eng.*, 15(3), 235-246.
- Shokouhi, P., Niederleithinger, E., Zoega, A., Barner, A., and Schone, D. (2010). "Using Ultrasonic Coda Wave Interferometry for Monitoring Stress-Induced Changes in Concrete." *Proc., 23<sup>rd</sup> EEGS Symposium on the Application of Geophysics to Engineering and Environmental Problems*, Environmental and Engineering Geophysical Society, Keystone, CO.

- Shokouhi, P., Wöstmann, J., Schneider, G., Milmann, B., Taffe, A., and Wiggerhauser, H. (2011). "Nondestructive Detection of Delamination in Concrete Slabs." *Transportation Research Record: Journal of the Transportation Research Board*, Transportation Research Board of the National Academies, Washington, DC, 2252, 103.
- Sokolov, S. (1929). "On the Question of the Propagation of High Frequency Acoustic Oscillations in Various Bodies." *Elkt. Nachr. Tech.*, 6, 454-460.
- Streicher, D., Algernon, D., Wöstmann, J., Behrens, M., and Wiggerhauser, H. (2006). "Automated NDE of Post-Tensioned Concrete Bridges Using Imaging Echo Methods." *Proc., 9<sup>th</sup> European Conference on Nondestructive Testing, ECNDT*, Berlin, Germany.
- Woo, J. (2006). "A Short History of the Development of Ultrasound in Obstetrics and Gynecology." < <http://www.ob-ultrasound.net/history1.html> > (February, 2012).



APPENDIX A  
SUPPORTING MATERIAL

**Detailed defect dimensions (dim.), depth, and cover and spacing (C & S). All units in inches.**

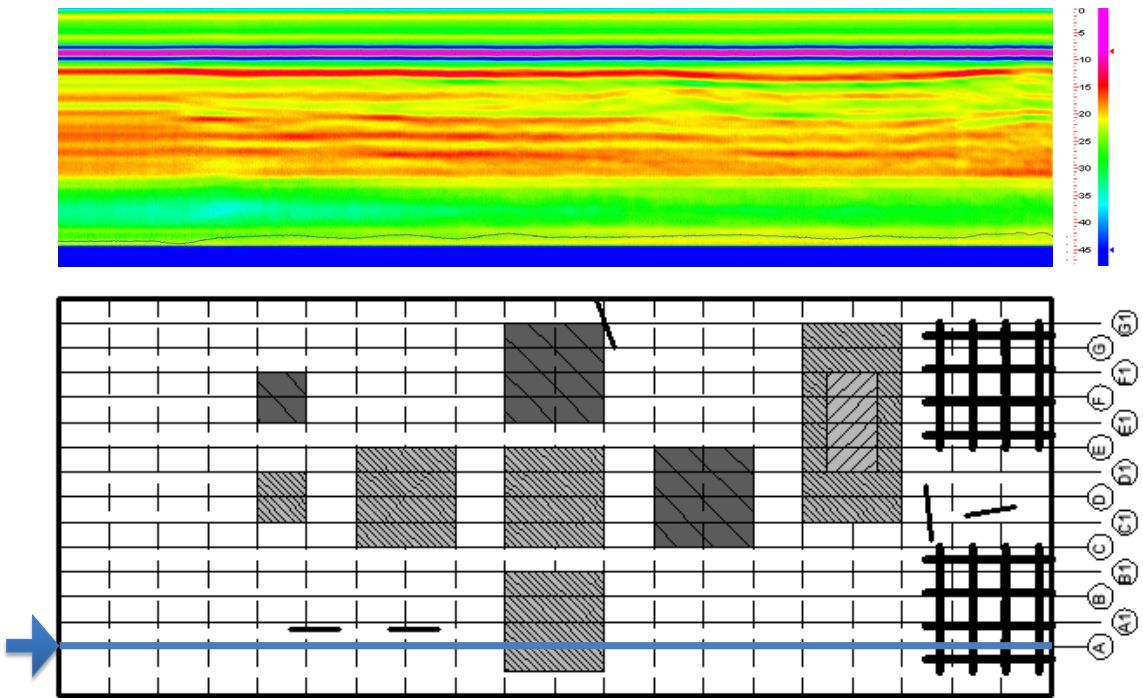
C=concrete; SC=shotcrete; WF=water-filled; AF=air-filled

SPECIMEN NAME & MATERIAL	ACTUAL REINF. C & S	MEASURED REINF. C & S	TYPE OF DEFECT	ACTUAL DIM. OF DEFECT	ACTUAL DEPTH OF DEFECT	MEASURED DIM. OF DEFECT	MEASURED DEPTH OF DEFECT	ACTUAL SPECIMEN DEPTH	MEASURED SPECIMEN DEPTH
Alpha, C	None	N/A	None	N/A	N/A	N/A	N/A	12	12.4
Beta, C	*	4.0 @ 8.0 OC	None	N/A	N/A	N/A	N/A	18	17.6
Gamma, C	*	4.3 @ 7.9 OC	None	N/A	N/A	N/A	N/A	12	11.7
Delta, C	None	N/A	None	N/A	N/A	N/A	N/A	24	23.6
Epsilon, C	*	4.1 @ 8 OC	None	N/A	N/A	N/A	N/A	24	23.3
Zeta, C	*	3.8 @ 7.9 OC	None	N/A	N/A	N/A	N/A	15	14.1
Eta, C	*	4.5 @ 7.9 OC	plastic	12 x 12 x 1	2	11.7 x 12.8	2.3	15	14.2
Theta, C	*	4.4 @ 8.0 OC	plastic	12 x 12 x 1	3	11.7 x 13.5	3.5	15	13.9
Iota, C	*	4.0 @ 8.0 OC	plastic	12 x 12 x 1	1	7.8 x 12.3	1.7	15	13.0
Kappa, C	*	3.8 @ 8.0 OC	Styrofoam	12 x 12 x 1	8	15.7 x 15.7	8.0	15	14.7
Lamda, C	*	3.7 @ 8.1 OC	WF void	12 x 12	8	16.5 x 15.4	6.5-8.8	15	14.6
A, SC	None	N/A	None	N/A	N/A	N/A	N/A	4	3.9
B, SC	None	N/A	None	N/A	N/A	N/A	N/A	6	5.7
C, SC	None	N/A	None	N/A	N/A	N/A	N/A	8	6.8
D, SC	**	6.9	AF void	17.25 x 14.75	7-5/8	12.4 x 12.1	7.6	12	11.3
E, SC	**	6.4	WF void	15.75x 14.5	7-1/2	15.5 x 13.3	7.6	12	11.0
F, SC	**	6.7	AF void	17.125 x14.75	3	18.1 x 15.6	3.5	12	11.2
G, SC	**	6.8	WF void	15.5 x 14.25	3	16.0 x 14.7	4.2	12	10.7
H, SC	**	6.4	Thin cloth	12 x 12	8	14.0 x 10.7	7.2	12	10.2
I, SC	**	5.7	Thin cloth	12 x 12	4	11.0 x 14.0	3.9	12	10.4
J, SC	**	6.1	Thin cloth	12 x 12	3	13.1 x 12.0	2.9	12	10.4
K, SC	**	5.6	Thin cloth	12 x 12	2	12.3 x 13.4	3.1	12	10.2
L, SC	**	5.6	Thin cloth	12 x 12	1	14.0 x 13.3	Very shallow	12	10.3
M, SC	**	5.8	None	N/A	N/A	N/A	N/A	12	10.4
A2, C	***	N/A	None	N/A	N/A	N/A	N/A	N/A	N/A
B2, C	***	N/A	1 clay lump	6-ø x 2	~ 6	6.1	6.3	N/A	N/A
C2, C	***	N/A	6 clay lumps	4-ø x 2	~3, 6, 9	3.1-4.1	2.7, 5.4, 8.5	N/A	N/A
D2, C	***	6.0 @ 8.0 OC	None	N/A	N/A	N/A	N/A	N/A	N/A
E2, C	***	6.0 @ 8.0 OC	1 clay lump	6-ø x 2	~ 6	4.2	4.6	N/A	N/A
F2, C	***	6.0 @ 8.0 OC	6 clay lumps	4-ø x 2	~3, 6, 9	2.9-3.9	2.4, 5.4, 7.8	N/A	N/A

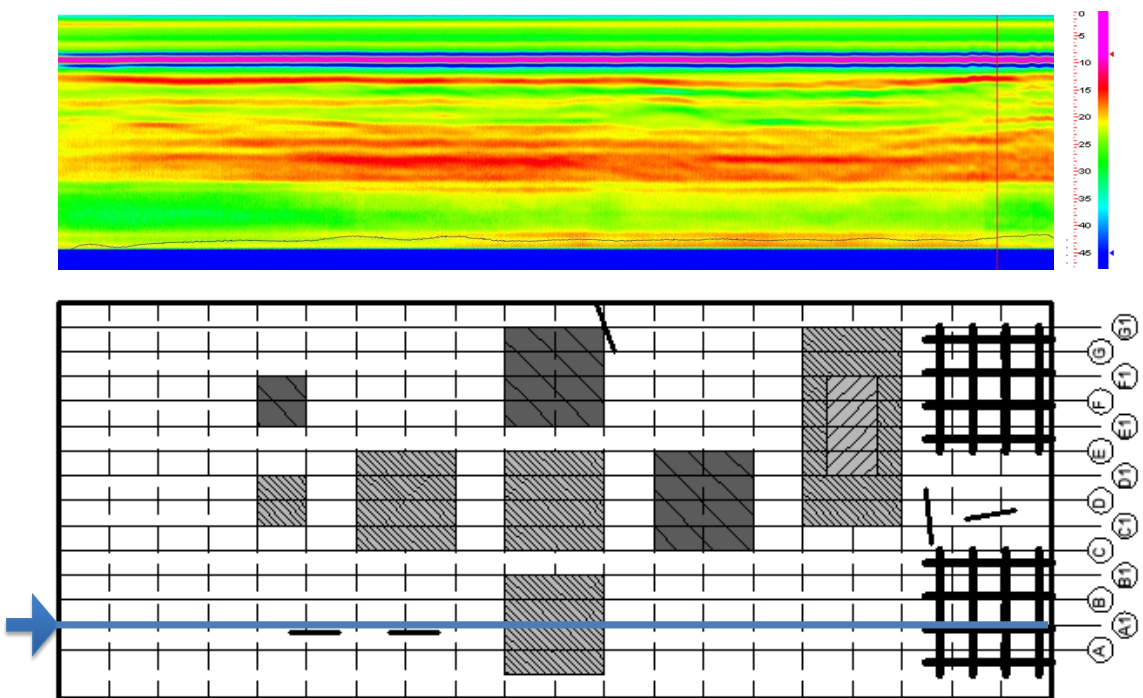
\* Two mats of No. 5 Rebar, 4 in. from top and bottom, 8 in. o.c.

\*\* One lattice girder in center of slab, sitting on bottom form, centroid of upper bar 5.25 in. from bottom, or ~6.25 in. from top

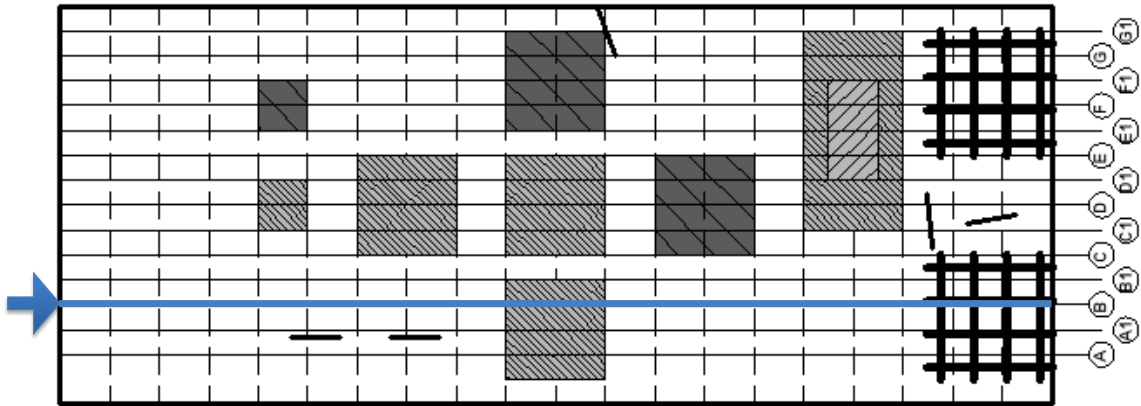
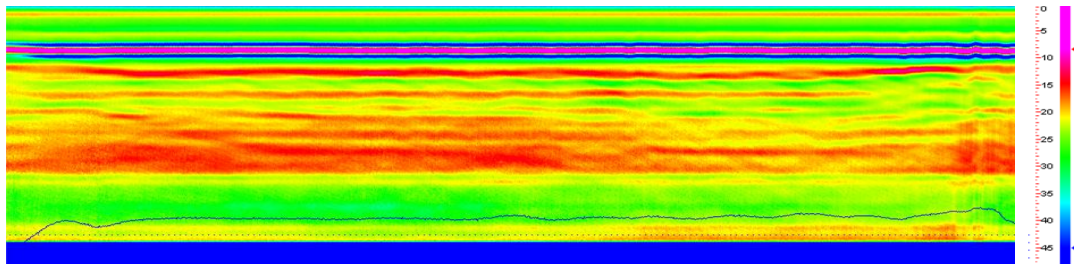
\*\*\*One mat of No. 5 Rebar, 6 in. from top, 8 in. o.c.



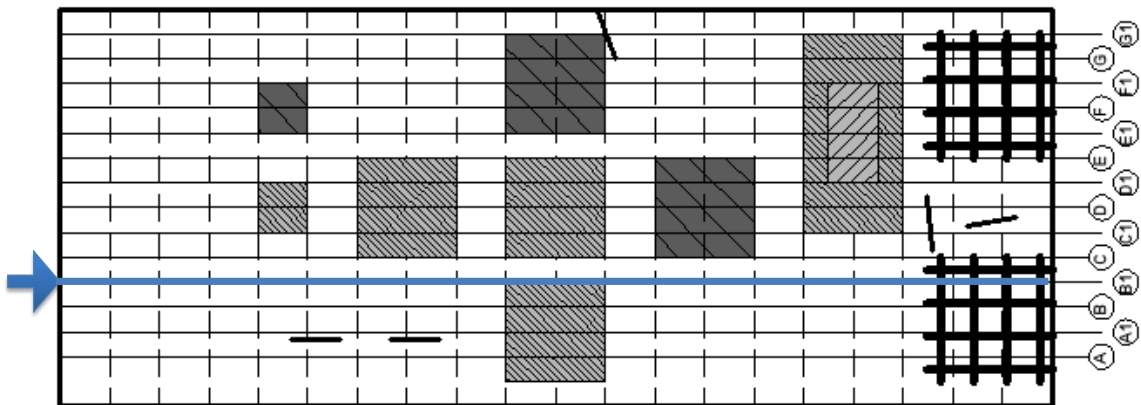
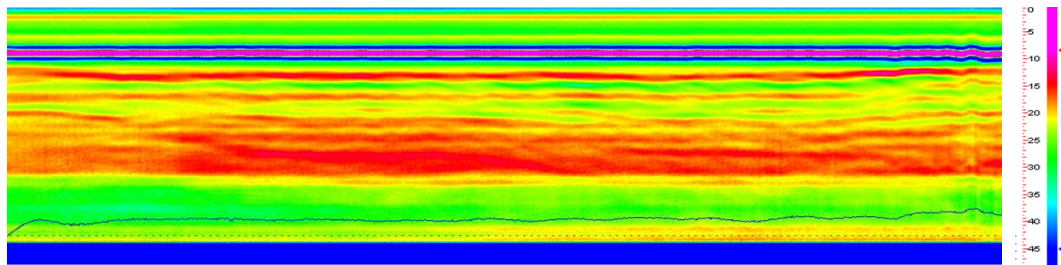
UTEP Bridge Deck, GPR Scan 1



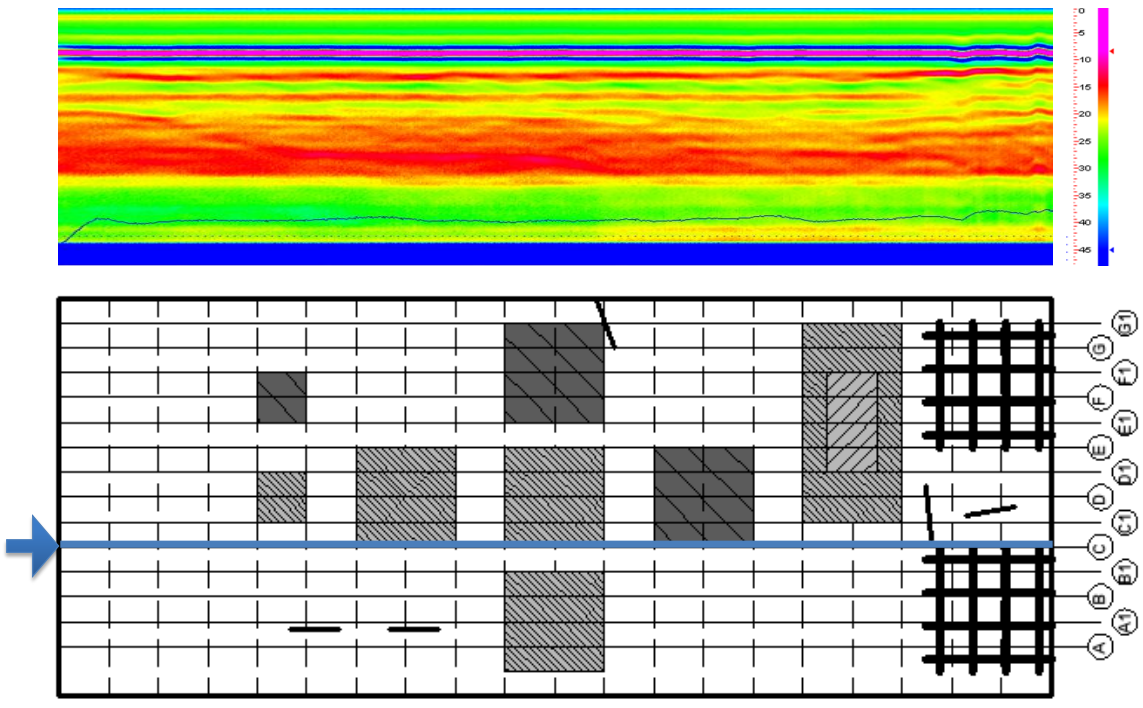
UTEP Bridge Deck, GPR Scan 2



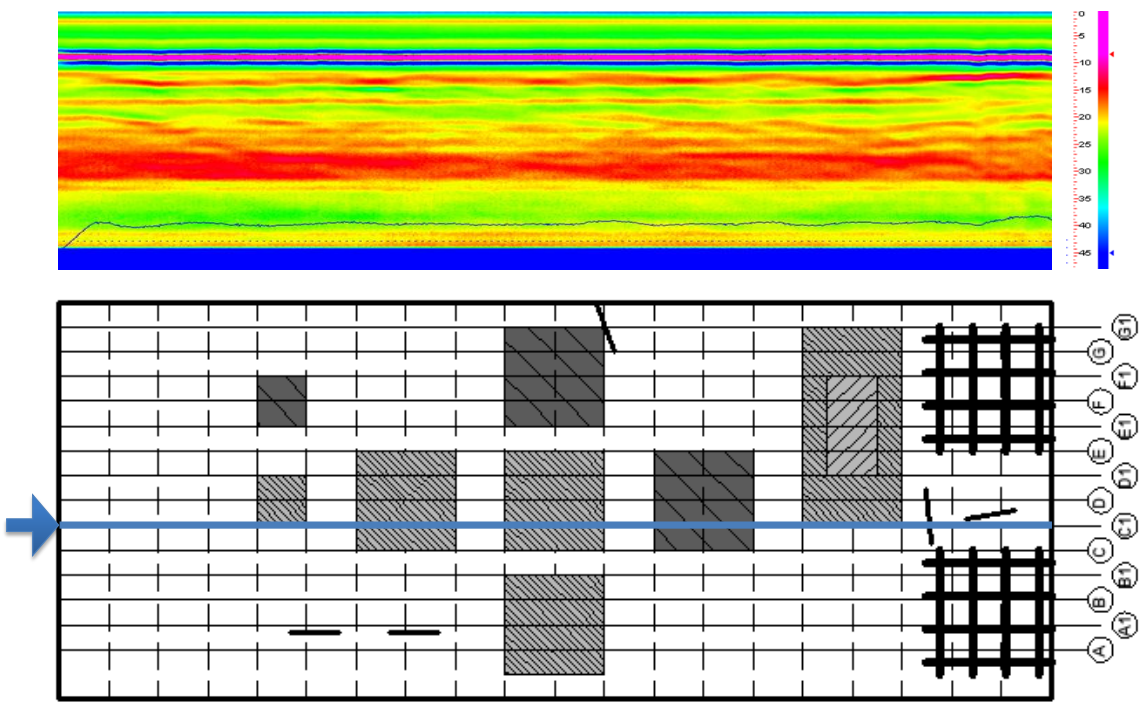
UTEP Bridge Deck, GPR Scan 3



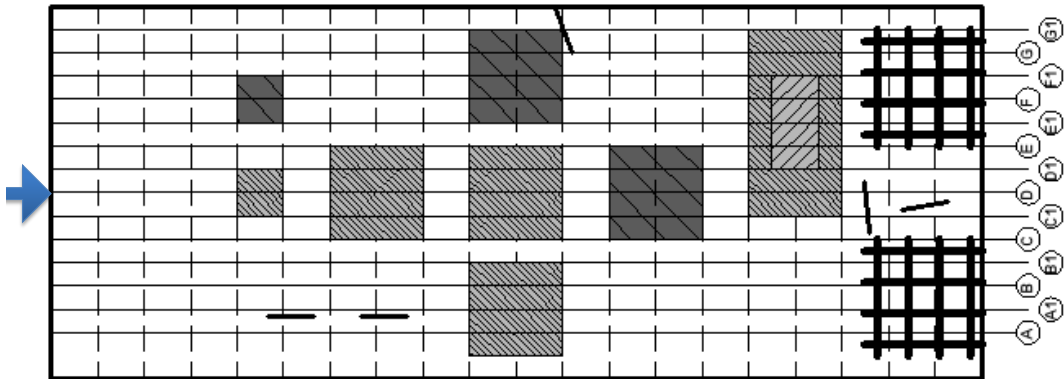
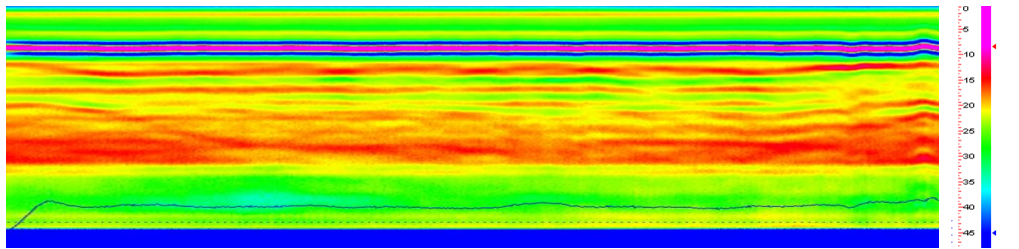
UTEP Bridge Deck, GPR Scan 4



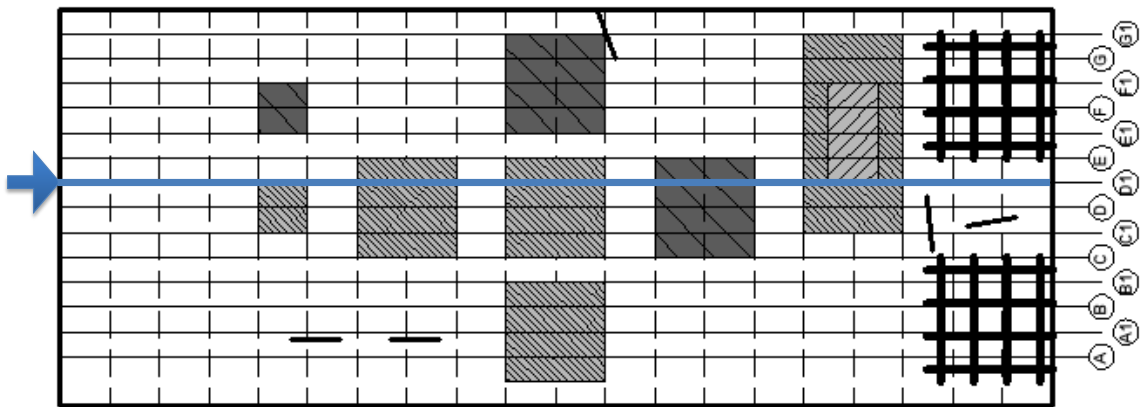
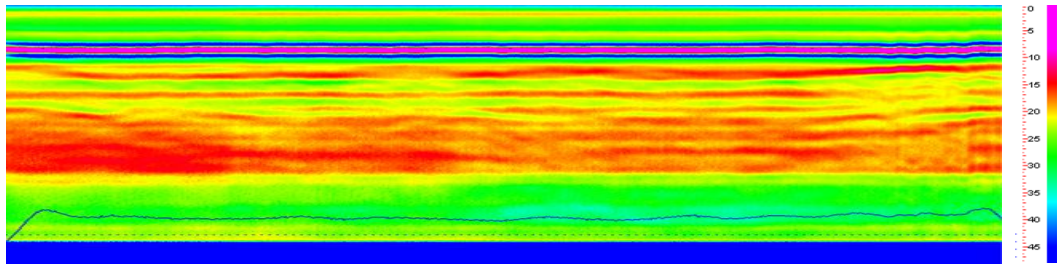
UTEP Bridge Deck, GPR Scan 5



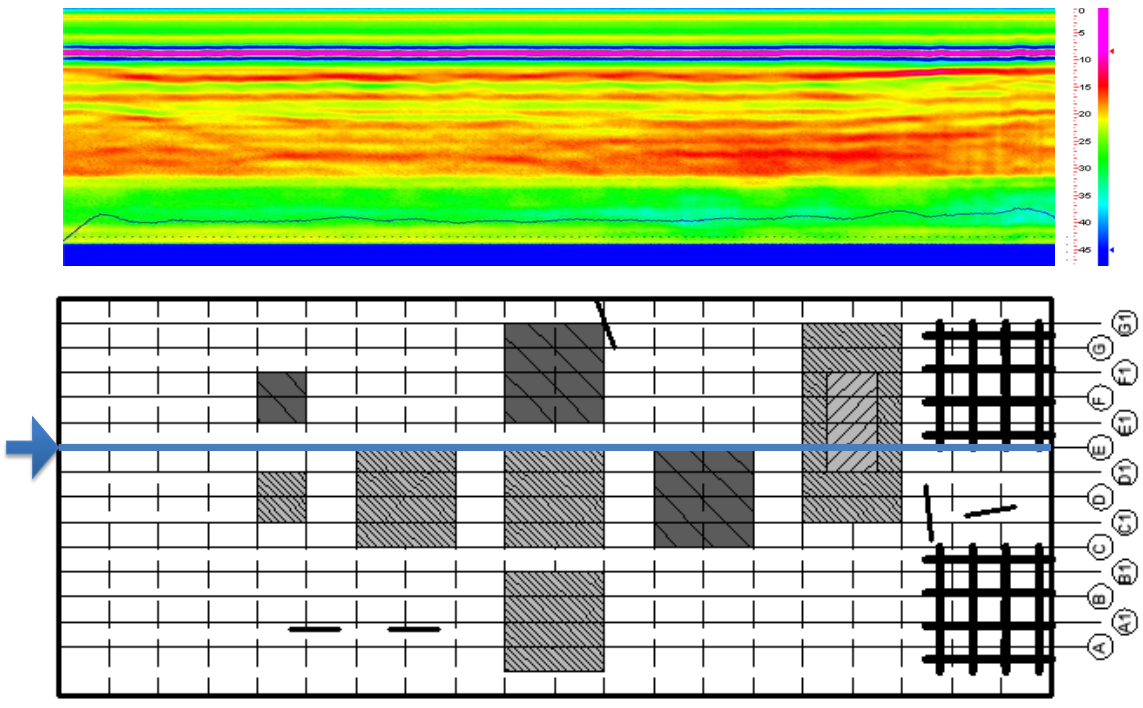
UTEP Bridge Deck, GPR Scan 6



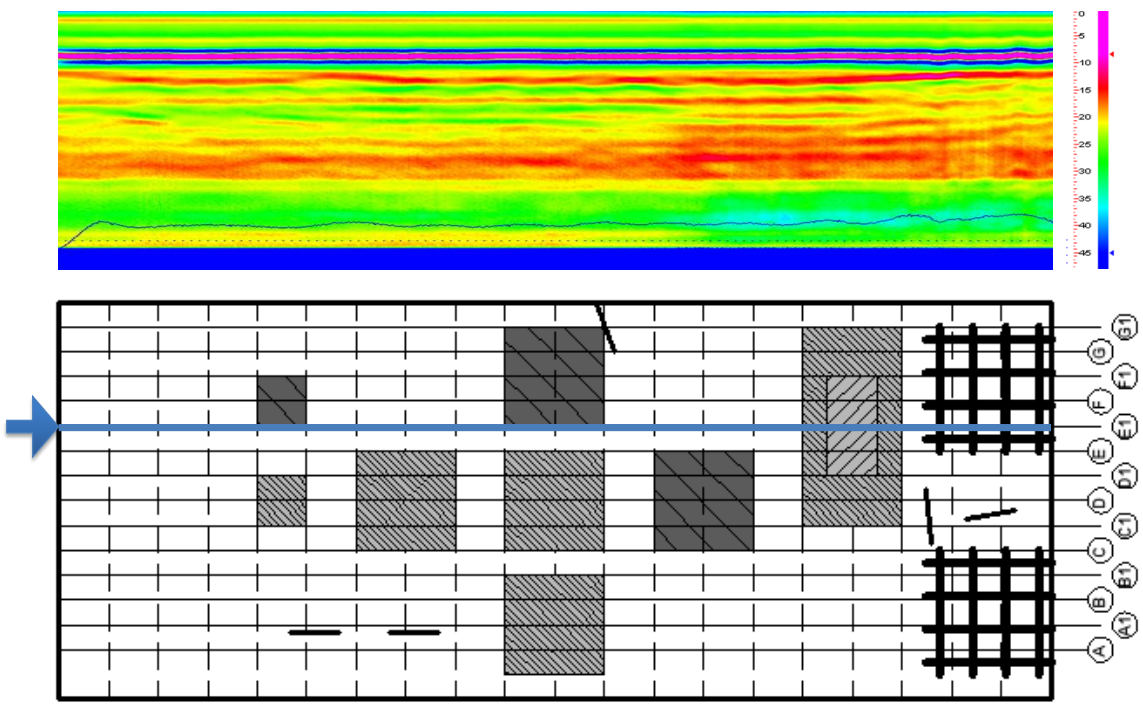
UTEP Bridge Deck, GPR Scan 7



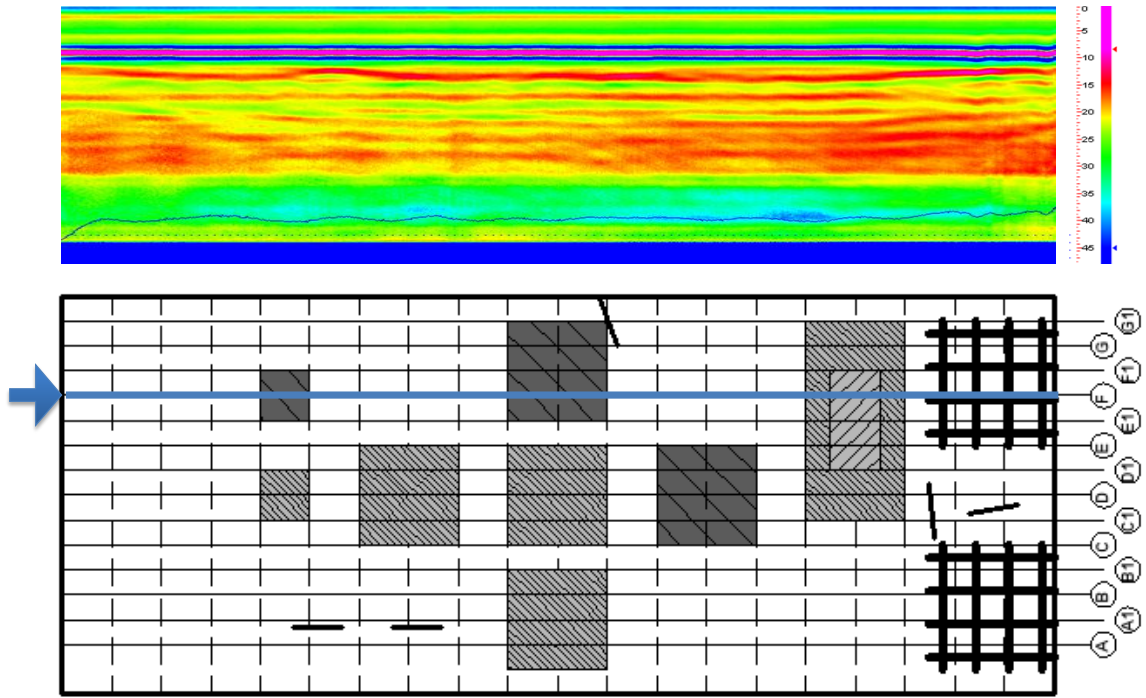
UTEP Bridge Deck, GPR Scan 8



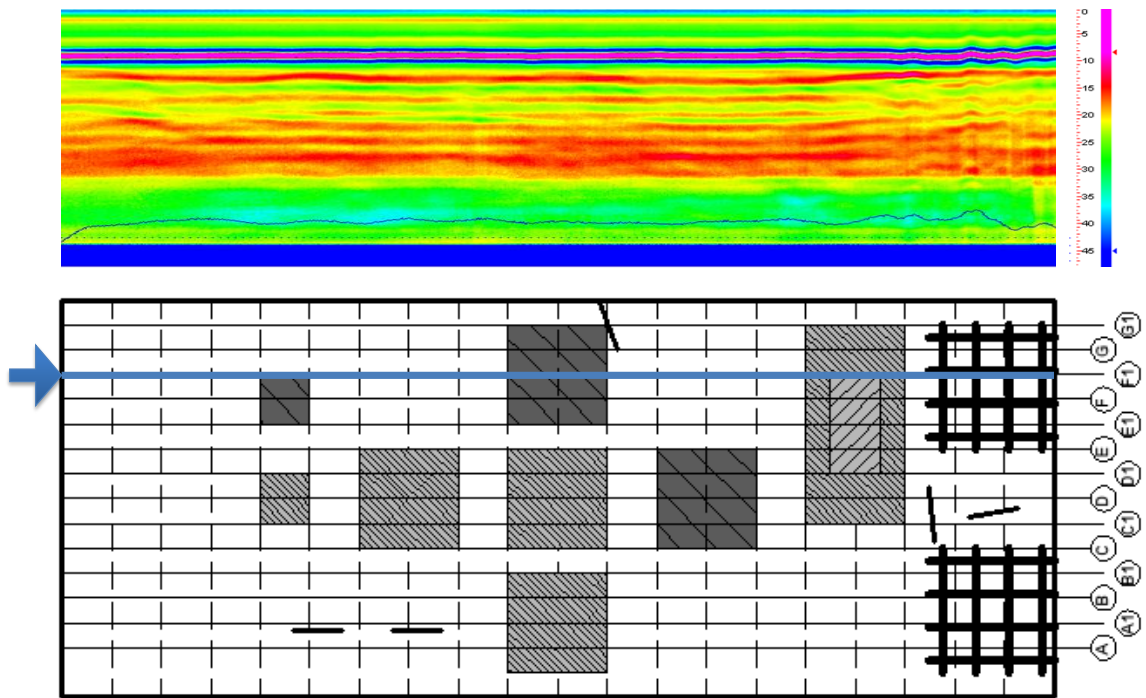
UTEP Bridge Deck, GPR Scan 9



UTEP Bridge Deck, GPR Scan 10

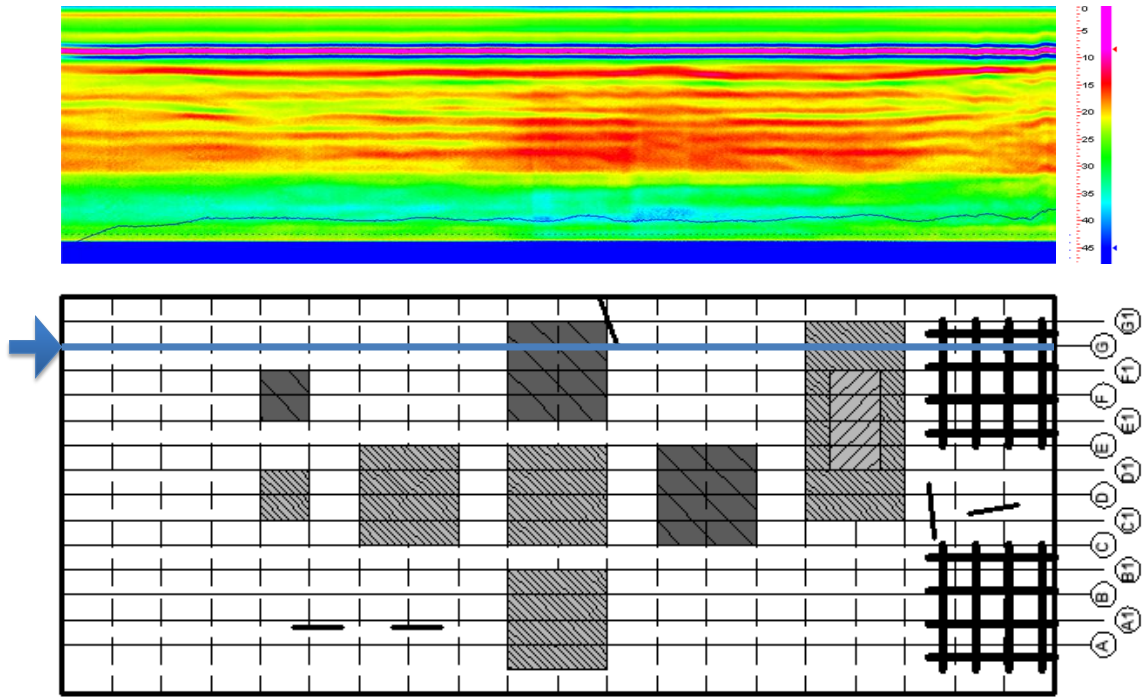


UTEP Bridge Deck, GPR Scan 11



UTEP Bridge Deck, GPR Scan 12





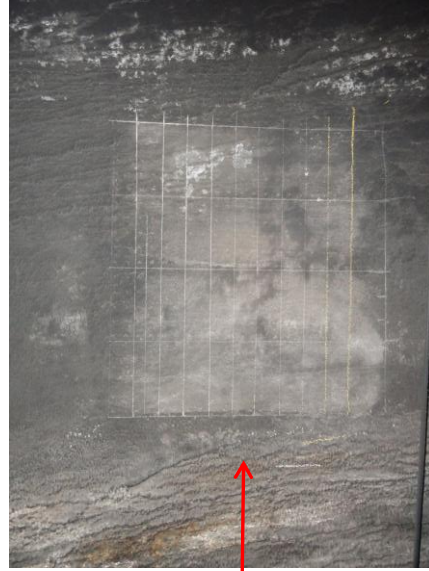
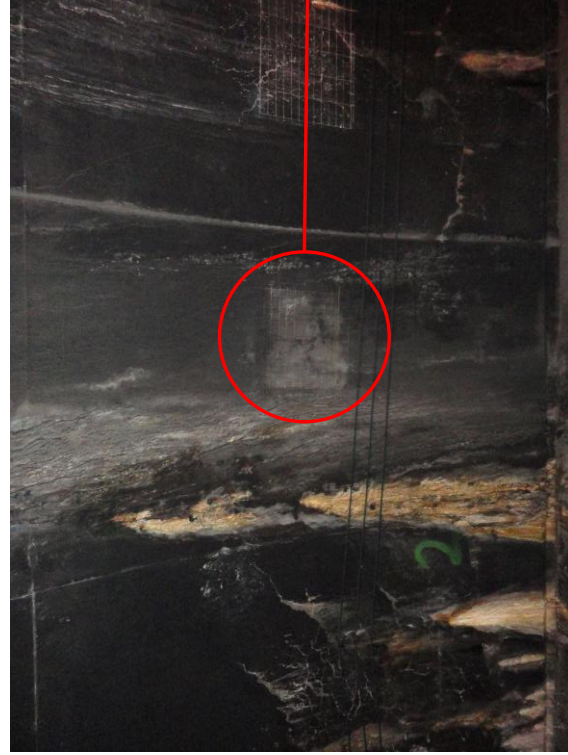
UTEP Bridge Deck, GPR Scan 13

APPENDIX B  
SUMMARY OF NDT REPORTS

## Eisenhower Memorial Tunnel, Dillon, CO

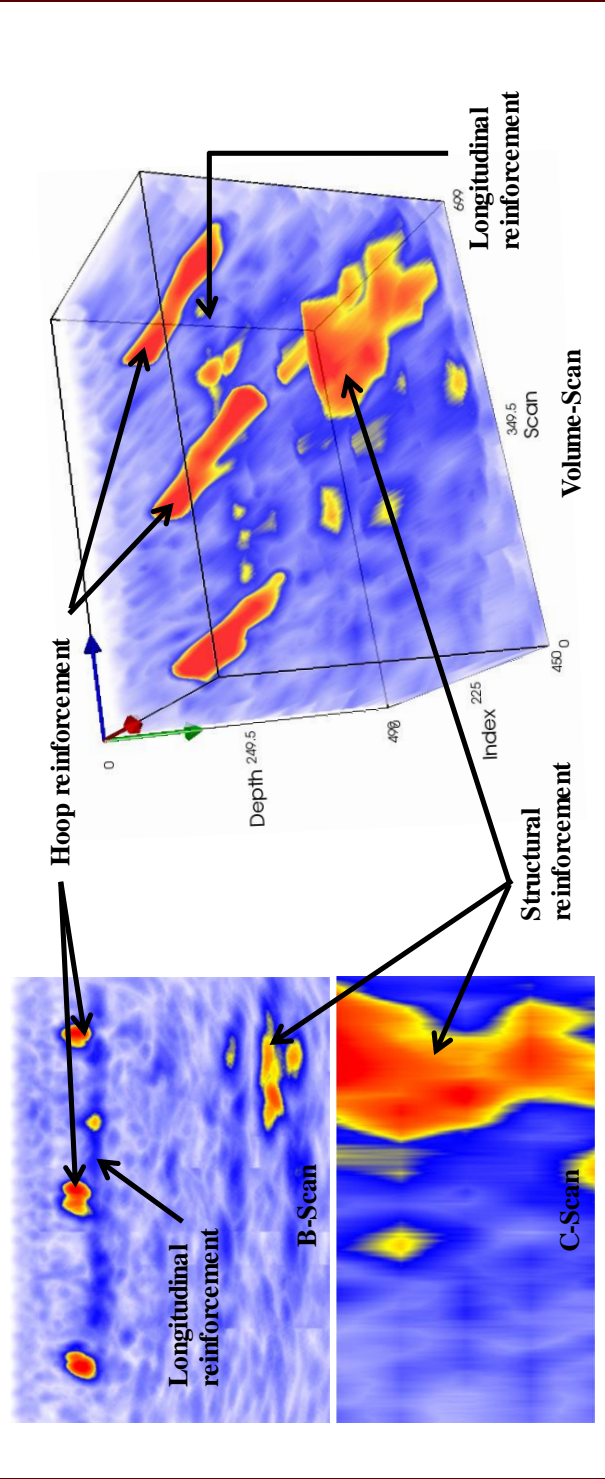


Defects	Notes	Backsurface	Reinf. Detail	Test Parameters
No significant defect noticed, except for "strip" of area (~9.4" wide, 16.2" deep) consistently found in other maps. Possibly structural reinforcement: wood or steel?	Area tested as representative of "sound" concrete.	Not discernible	Hoop Reinf. ~4.2" deep @ ~9.9" O.C. Longitudinal Reinf: On bottom	$V_{shear} = 2751 \text{ m/s}$ X-step: 150 mm Y-step: 50 mm Max Depth: 1000 mm Frequency: 50 kHz
Dillon, CO Eisenhower Tunnel ET 10.4-1, 2 Segment 8 TAMU/TTI 10/2011				



## Eisenhower Memorial Tunnel, Dillon, CO

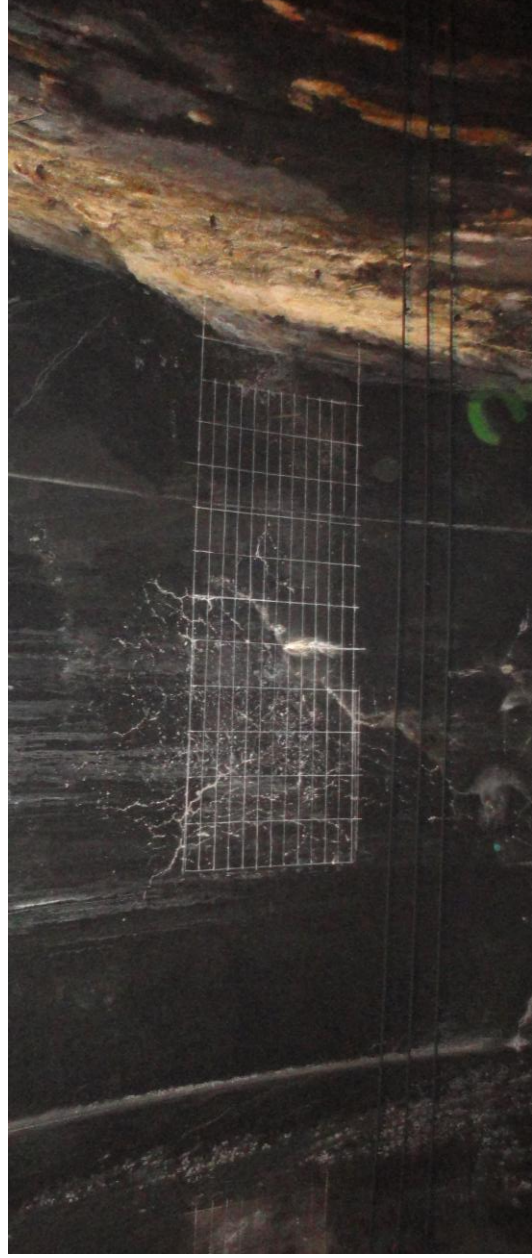
Defects	Notes	Backsurface	Reinf. Detail	$V_{shear} = 2751$ m/s X-step: 150 mm Y-step: 50 mm Max Depth: 1000 mm Frequency: 50 kHz Dillon, CO Eisenhower Tunnel ET 10.4-1, 2 Segment 8 TAMU/TTI 10/2011
No significant defect noticed, except for "strip" of area (~9.4" wide, 16.2" deep) consistently found in other maps. Possibly structural reinforcement: wood or steel?	Area tested as representative of "sound" concrete.	Not discernible	Hoop Reinf. ~4.2" deep @ ~9.9" O.C. Longitudinal Reinf: On bottom	



## Eisenhower Memorial Tunnel, Dillon, CO

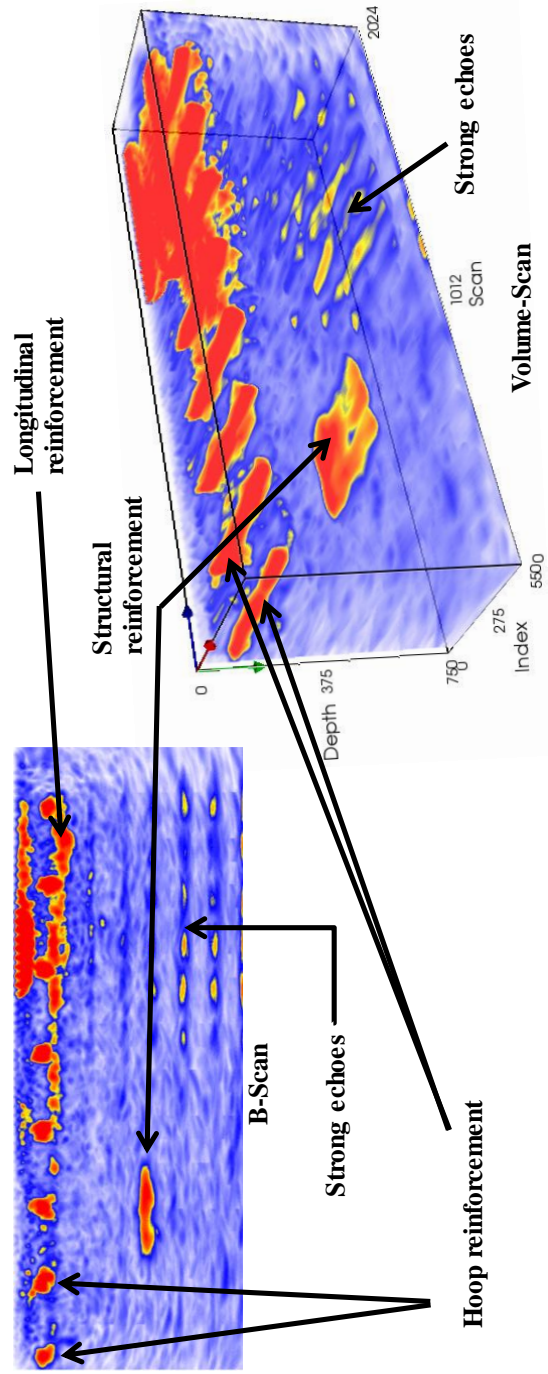


Defects	Notes	Backsurface	Reinf. Detail	$V_{shear} = 2751 \text{ m/s}$ X-step: 150 mm Y-step: 50 mm Max Depth: 750 mm Frequency: 50 kHz
No significant defect noticed, except for "strip" of area (~12.2" wide, 17.2" deep) consistently found in other maps. Possibly structural reinforcement: wood or steel?	Area tested because of surface cracking and crazing, nearby stalactite formation (Could not test over stalactite crack due to obtrusions).	Not discernible	Hoop Reinf: ~3.7"-5.1" deep @ ~10.1" O.C. Longitudinal Reinf: On bottom	Dillon, CO Eisenhower Tunnel ET 10.4-3 Segment 8 TAMU/TTI 10/2011



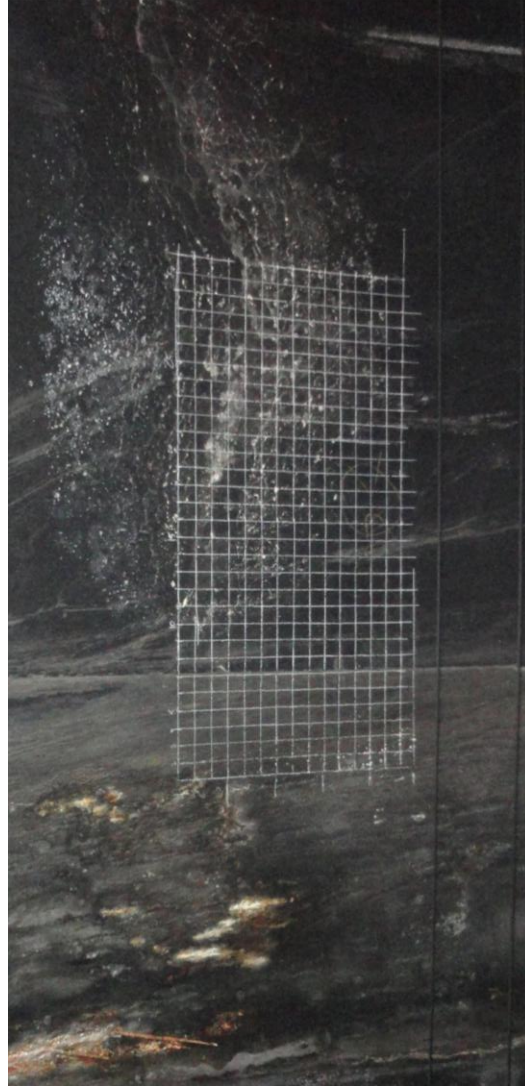
## Eisenhower Memorial Tunnel, Dillon, CO

Defects	Notes	Backsurface	Reinf. Detail	$V_{shear} = 2751$ m/s X-step: 150 mm Y-step: 50 mm Max Depth: 750 mm Frequency: 50 kHz Dillon, CO Eisenhower Tunnel ET 10.4-3 Segment 8 TAMU/TTI 10/2011
No significant defect noticed, except for "strip" of area (~12.2" wide, 17.2" deep) consistently found in other maps. Possibly structural reinforcement: wood or steel?	Area tested because of surface cracking and crazing, nearby stalactite formation (Could not test over stalactite crack due to obtrusions).	Not discernible	Hoop Reinf: ~3.7"-5.1" deep @ ~10.1" O.C. Longitudinal Reinf: On bottom	



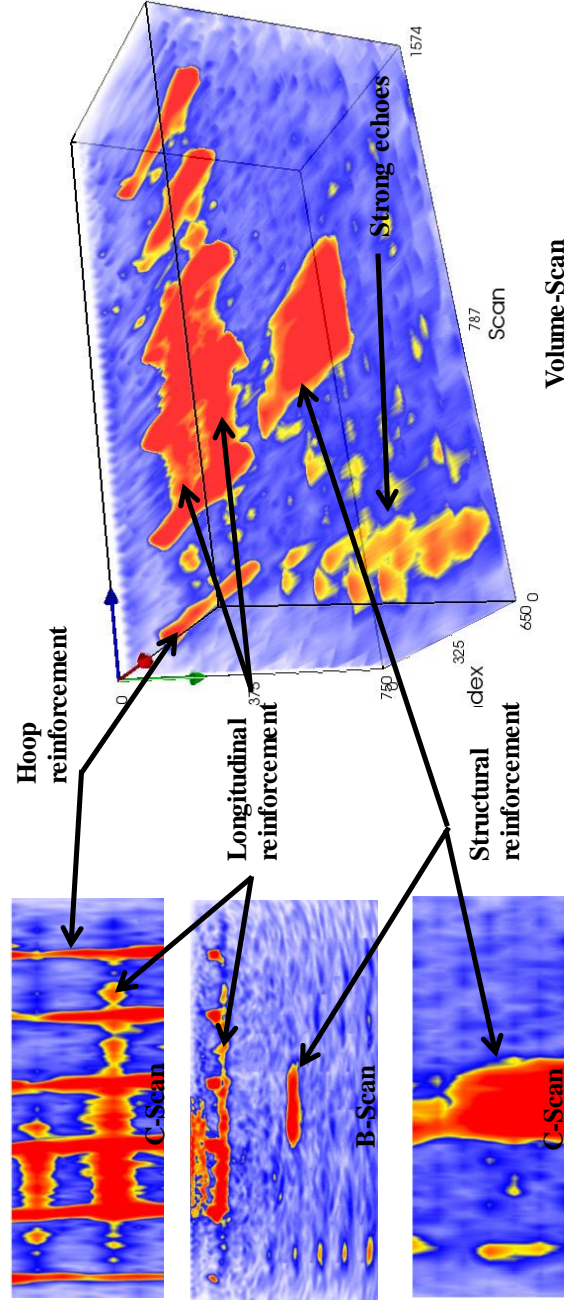
## Eisenhower Memorial Tunnel, Dillon, CO

Defects	Notes	Backsurface	Reinf. Detail	$V_{shear} = 2751$ m/s X-step: 150 mm Y-step: 50 mm Max Depth: 750 mm Frequency: 50 kHz
No significant defect noticed, except for "strip" of area (~13.5" wide, 16.1" deep) consistently found in other maps. Possibly structural reinforcement: wood or steel?	Area tested because of surface cracking and crazing, nearby joint.	Not discernible	Hoop Reinf. ~4.1" deep @ ~10.1" O.C. Longitudinal Reinf: On bottom	Dillon, CO Eisenhower Tunnel ET 10.4-4, 5 Segment 10 TAMU/TTI 10/2011



## Eisenhower Memorial Tunnel, Dillon, CO

Defects	Notes	Backsurface	Reinf. Detail	$V_{shear} = 2751$ m/s X-step: 150 mm Y-step: 50 mm Max Depth: 750 mm Frequency: 50 kHz Dillon, CO Eisenhower Tunnel ET 10.4-4, 5 Segment 10 TAMU/TTI 10/2011
No significant defect noticed, except for "strip" of area (~13.5" wide, 16.1" deep) consistently found in other maps. Possibly structural reinforcement: wood or steel?	Area tested because of surface cracking and crazing, nearby joint.	Not discernible	Hoop Reinf. ~4.1" deep @ ~10.1" O.C. Longitudinal Reinf: On bottom	

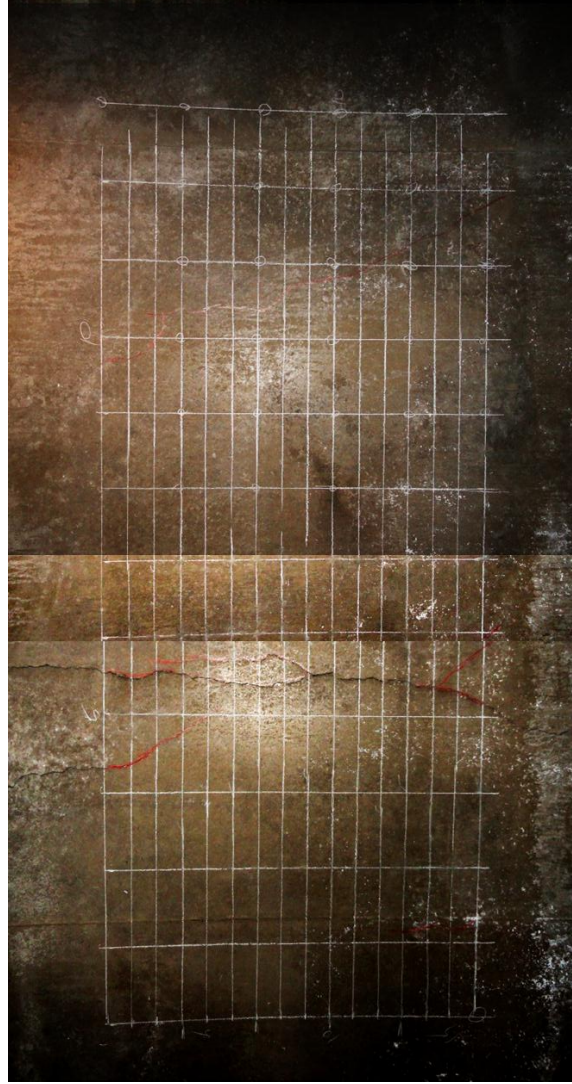




## Hanging Lake Tunnel, Glenwood Springs, CO



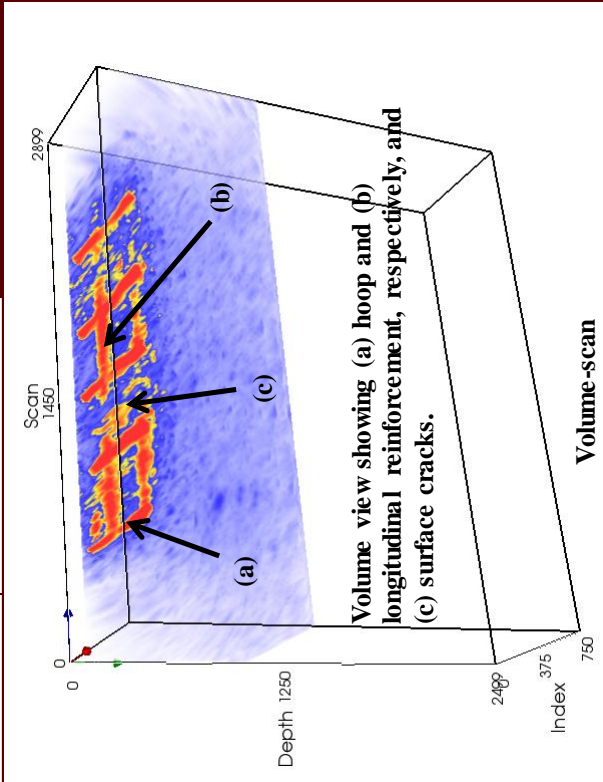
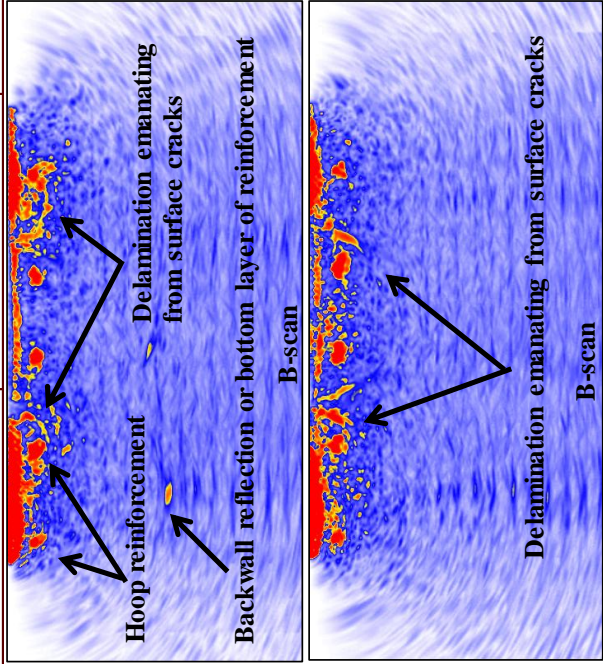
Defects	Notes	Backsurface	Reinf. Detail	V <sub>shear</sub> = 2159 m/s X-step: 150 mm Y-step: 50 mm Max Depth: 2500 mm Frequency: 50 kHz
Apparent delamination extending 12.3" deep, originating from surface crack; possibly trying to meet another crack located approximately 35" east (right) of surface crack.	Severe cracking. Area also tested by BAM.	Possibly 27.6"	Hoop Reinf: 4.6"- 6.2" deep @ 15.7" O.C. Longitudinal Reinf: On top (and below?) HR @ 14.1" O.C.	Glenwood Springs, CO Hanging Lake Tunnel HLT 10.5-1, 2, 3 Segment 57 TAMU/TTI 10/2011



# Hanging Lake Tunnel, Glenwood Springs, CO



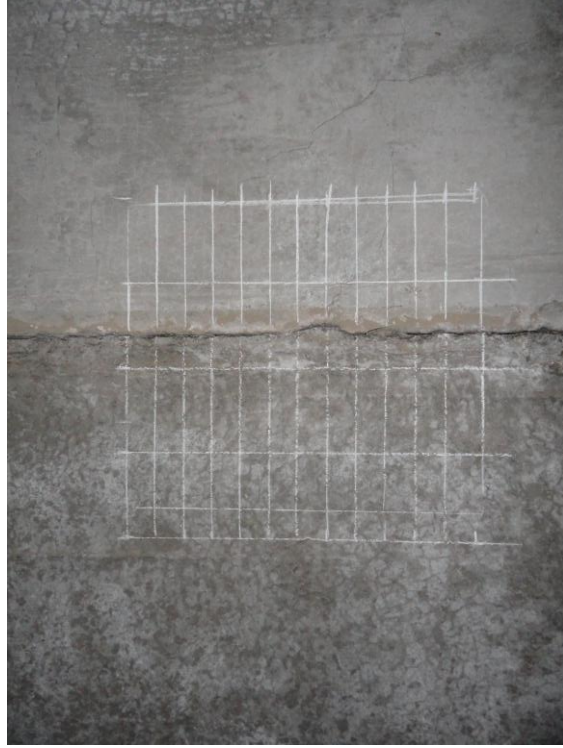
Defects	Notes	Backsurface	Reinf. Detail	$V_{shear} = 2159 \text{ m/s}$ X-step: 150 mm Y-step: 50 mm Max Depth: 2500 mm Frequency: 50 kHz Glenwood Springs, CO Hanging Lake Tunnel HLT 10.5-1, 2, 3 Segment 57 TAMU/TTI 10/2011
Apparent delamination extending 12.3" deep, originating from surface crack; possibly trying to meet another crack located approximately 35" east (right) of surface crack.	Severe cracking. Area also tested by BAM.	Possibly 27.6"	Hoop Reinf: 4.6"- 6.2" deep @ 15.7" O.C. Longitudinal Reinf: On top (and below?) HR @ 14.1" O.C.	



## Hanging Lake Tunnel, Glenwood Springs, CO

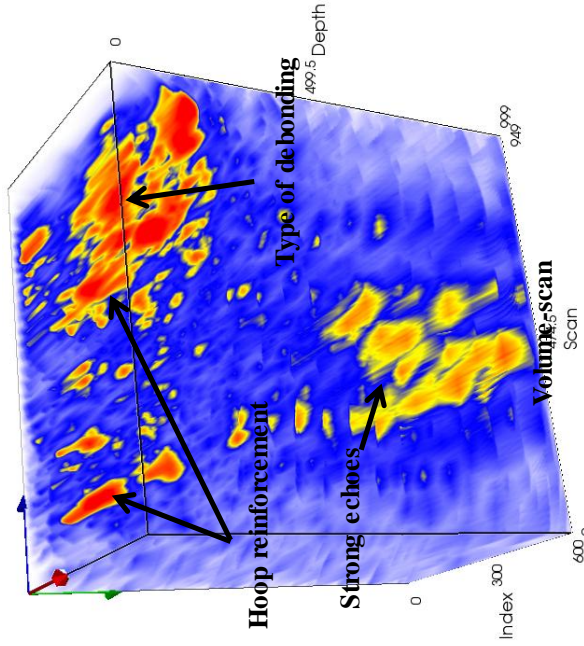
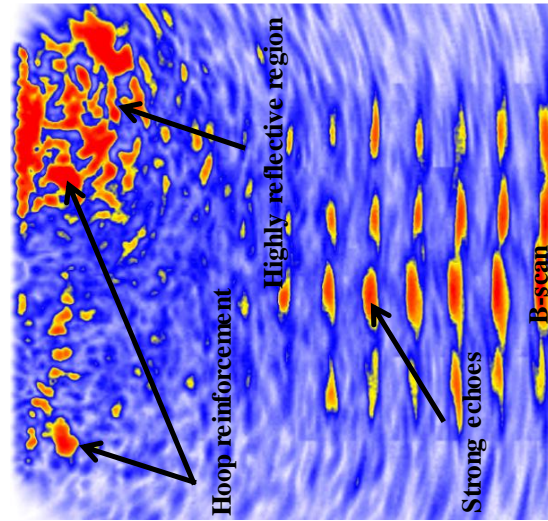


Defects	Notes	Backsurface	Reinf. Detail	V <sub>shear</sub> = 2159 m/s X-step: 150 mm Y-step: 50 mm Max Depth: 1000 mm Frequency: 50 kHz
<p>Suspected debonding around east (right) side of joint. Surface crack around area might support this.</p> <p>Suspected debonding extends a maximum of 9" deep.</p>	<p>Area tested because of natural joint. This map should be extended east to detail more of possible debonding.</p>	<p>Not detectable</p>	<p>Hoop Reinf. ~3.6" deep</p>	<p>Glenwood Springs, CO Hanging Lake Tunnel HLT 10.5-4 Segments 54/55 Joint TAMU/TTI 10/2011</p>



# Hanging Lake Tunnel, Glenwood Springs, CO

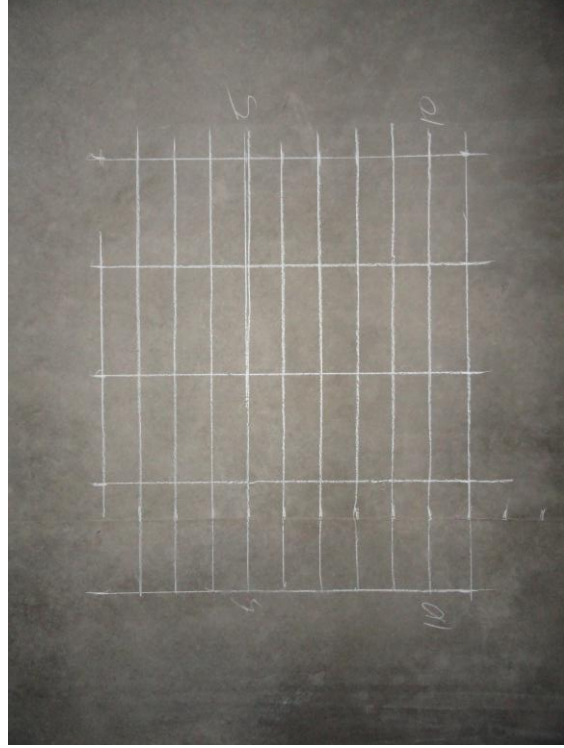
Defects	Notes	Backsurface	Reinf. Detail	$V_{shear} = 2159 \text{ m/s}$ X-step: 150 mm Y-step: 50 mm Max Depth: 1000 mm Frequency: 50 kHz
Suspected debonding around east (right) side of joint. Surface crack around area might support this. Suspected debonding extends a maximum of 9" deep.	Area tested because of natural joint. This map should be extended east to detail more of possible debonding.	Not detectable	Hoop Reinf. ~3.6" deep	Glenwood Springs, CO Hanging Lake Tunnel HLT 10.5-4 Segments 54/55 Joint TAMU/TTI 10/2011



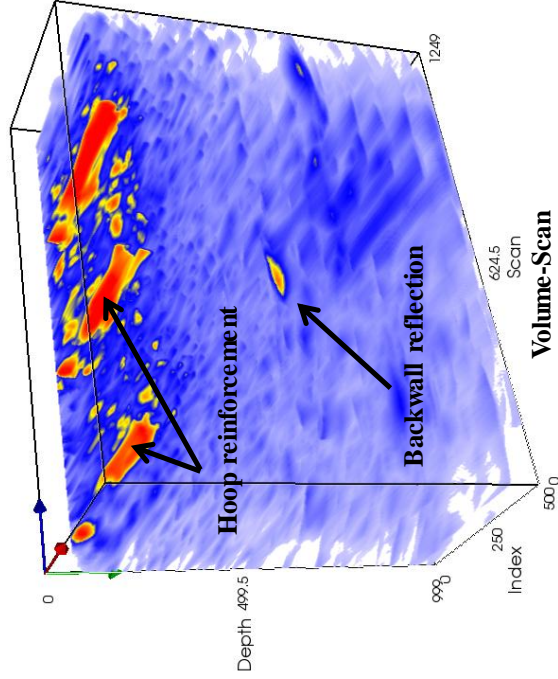
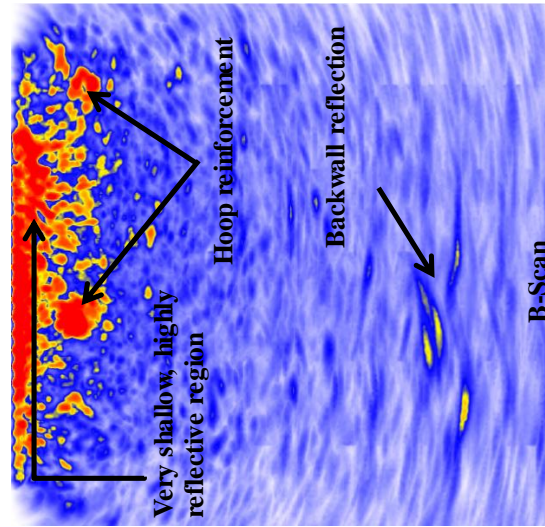
## Hanging Lake Tunnel, Glenwood Springs, CO



Defects	Notes	Backsurface	Reinf. Detail	V <sub>shear</sub> = 2159 m/s X-step: 150 mm Y-step: 50 mm Max Depth: 2500 mm Frequency: 50 kHz
No significant defect noticeable. Backwall reflection varies 2-3" in depth, so this may be lower reinforcement reflection or backwall delamination (see HLT 10.5-8,9)	Area tested as a representation of "sound concrete" - no apparent cracks, defects.	Possibly 29.6" - 32.4"	Hoop Reinf: ~4.3"-5.1" deep @ 16.6" O.C. Longitudinal Reinf: On top	Glenwood Springs, CO Hanging Lake Tunnel HLT 10.5-5, 6, 7 Segment 49 TAMU/TTI 10/2011



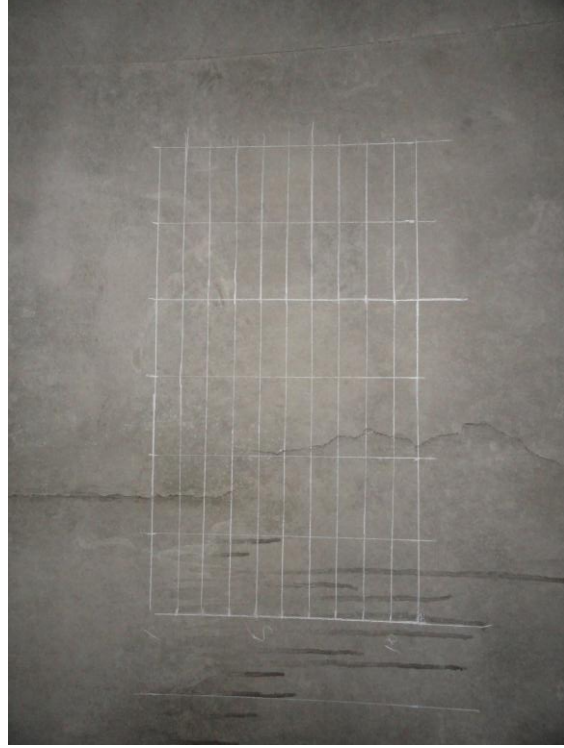
Defects	Notes	Backsurface	Reinf. Detail	$V_{shear} = 2159 \text{ m/s}$ X-step: 150 mm Y-step: 50 mm Max Depth: 2500 mm Frequency: 50 kHz
No significant defect noticeable. Backwall reflection varies 2-3" in depth, so this may be lower reinforcement reflection or backwall delamination (see HLT 10.5-8,9)	Area tested as a representation of "sound concrete" - no apparent cracks, defects.	Possibly 29.6" - 32.4"	Hoop Reinf: ~4.3"-5.1" deep @ 16.6" O.C. Longitudinal Reinf: On top	Glenwood Springs, CO Hanging Lake Tunnel HLT 10.5-5, 6, 7 Segment 49 TAMU/TTI 10/2011



## Hanging Lake Tunnel, Glenwood Springs, CO

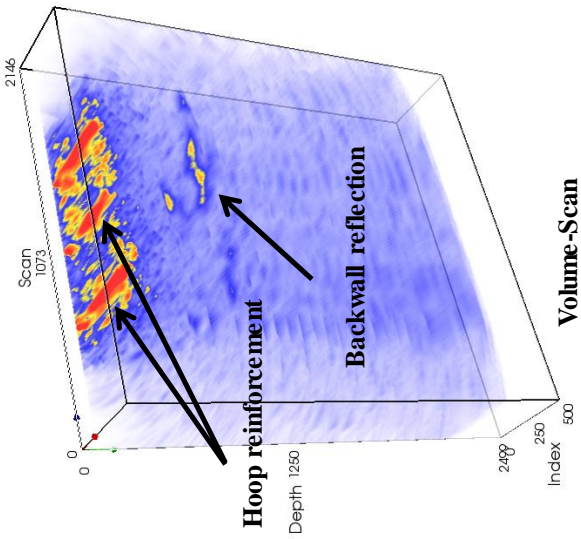
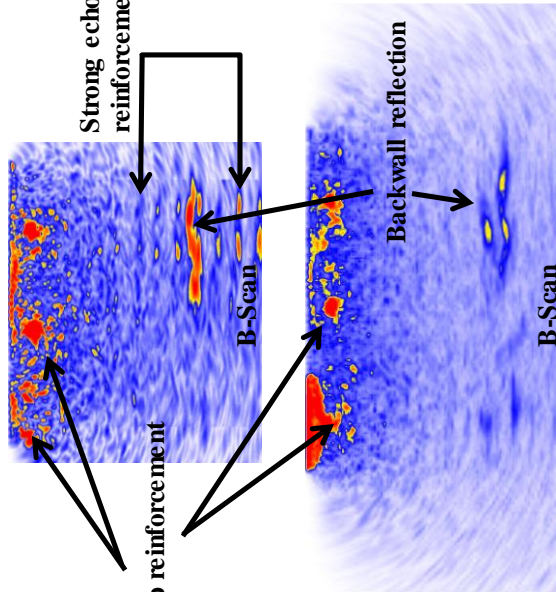


Defects	Notes	Backsurface	Reinf. Detail
No significant defect noticeable. Backwall reflection varies 2-3" in depth, so this may be lower reinforcement reflection or backwall delamination (see HLT 10.5-8,9).	Area tested because of single surface crack. Note strong echoes emanating from region of reinforcement. Sign of debonding?	Possibly 24.5" - 29.6"	Hoop Reinf. ~3.7" deep @ 15.9" O.C. Longitudinal Reinf: On bottom
		$V_{shear} = 2159 \text{ m/s}$ X-step: 150 mm Y-step: 50 mm Max Depth: 2500 mm Frequency: 50 kHz Glenwood Springs, CO Hanging Lake Tunnel HLT 10.5-8, 9 Segment 49 TAMU/TTI 10/2011	



# Hanging Lake Tunnel, Glenwood Springs, CO

<p><b>Defects</b></p> <p>No significant defect noticeable. Backwall reflection varies 2-3" in depth, so this may be lower reinforcement reflection or backwall delamination (see HLT 10.5-8,9).</p>	<p><b>Notes</b></p> <p>Area tested because of single surface crack. Note strong echoes emanating from region of reinforcement. Sign of debonding?</p>	<p><b>Backsurface</b></p> <p>Possibly 24.5" - 29.6"</p>	<p><b>Reinf. Detail</b></p> <p>Hoop Reinf. ~3.7" deep @ 15.9" O.C. Longitudinal Reinf: On bottom</p>	<p><math>V_{shear} = 2159</math> m/s          X-step: 150 mm          Y-step: 50 mm          Max Depth: 2500 mm          Frequency: 50 kHz          Glenwood Springs, CO          Hanging Lake Tunnel          HLT 10.5-8, 9          Segment 49          TAMU/TTI 10/2011</p>
---	---	---	--	--

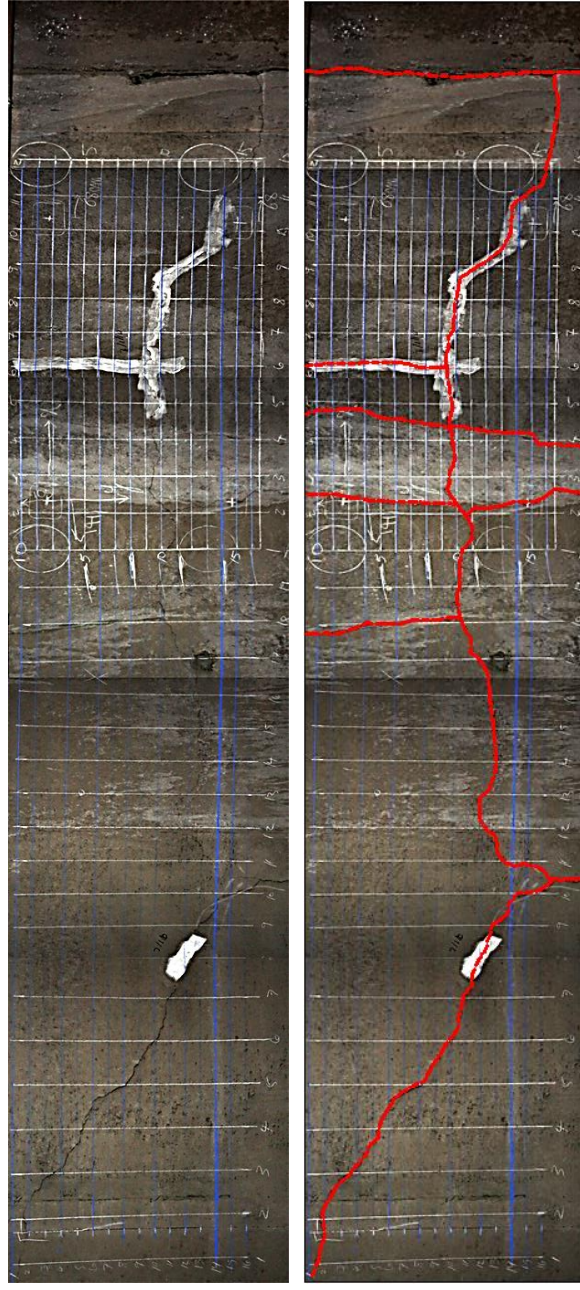




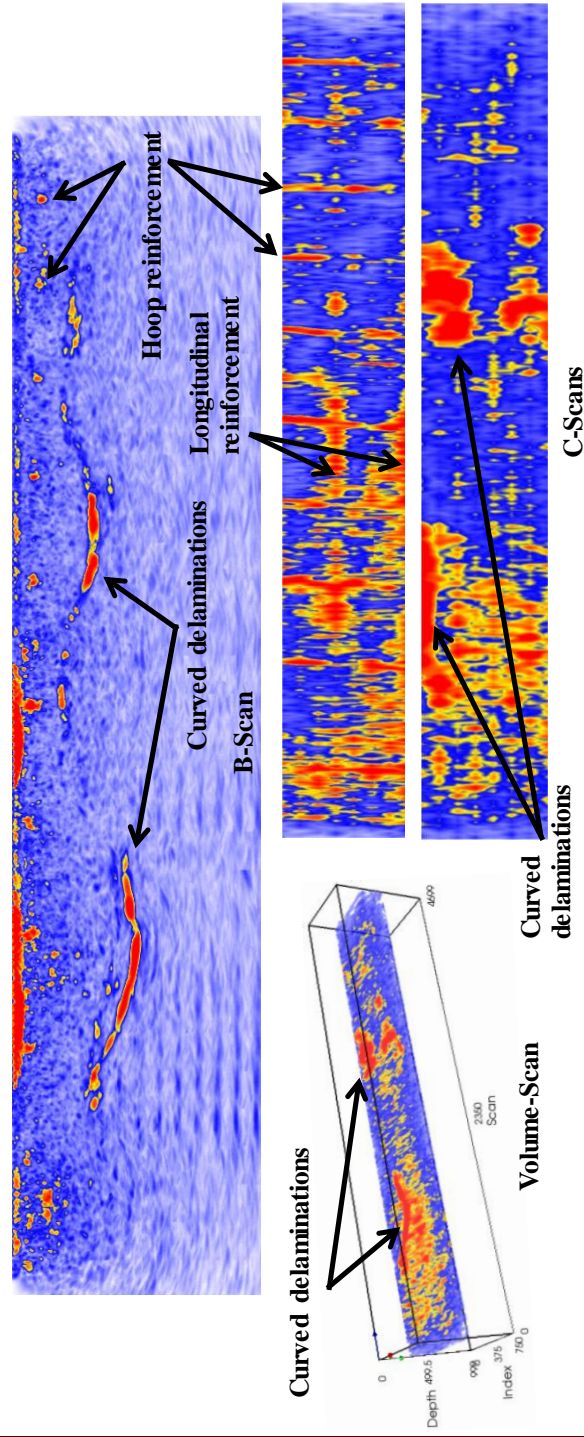
# Hanging Lake Tunnel, Glenwood Springs, CO



Defects	Notes	Backsurface	Reinf. Detail	Test Parameters
Significant delaminations discovered which stretched over 11', ranging from 8"-20" below the surface.	Area tested because of severe surface cracking.	Not discernible due to high presence of delaminations.	Hoop Reinf: ~2.9"-5.1" deep @ ~16.4" O.C. Longitudinal Reinf: On top	$V_{shear} = 2159 \text{ m/s}$ X-step: 150 mm Y-step: 50 mm Max Depth: 1000 mm Frequency: 50 kHz
Glenwood Springs, CO Hanging Lake Tunnel HLT 10.5-10, 11, 12 Segment 55 TAMU/TTI 10/2011				



Defects	Notes	Backsurface	Reinf. Detail	Test Parameters
Significant delaminations discovered which stretched over 11', ranging from 8"-20" below the surface.	Area tested because of severe cracking. The B-scan below shows variance in depth and the C-scans show the planar nature of the delaminations.	Not discernible due to high presence of delaminations.	Hoop Reinf: ~2.9"-5.1" deep @ ~16.4" O.C. Longitudinal Reinf: On top	$V_{shear} = 2159 \text{ m/s}$ X-step: 150 mm Y-step: 50 mm Max Depth: 1000 mm Frequency: 50 kHz
Glenwood Springs, CO Hanging Lake Tunnel HLT 10.5-10, 11, 12 Segment 55 TAMU/TTI 10/2011				



# Hanging Lake Tunnel, Glenwood Springs, CO

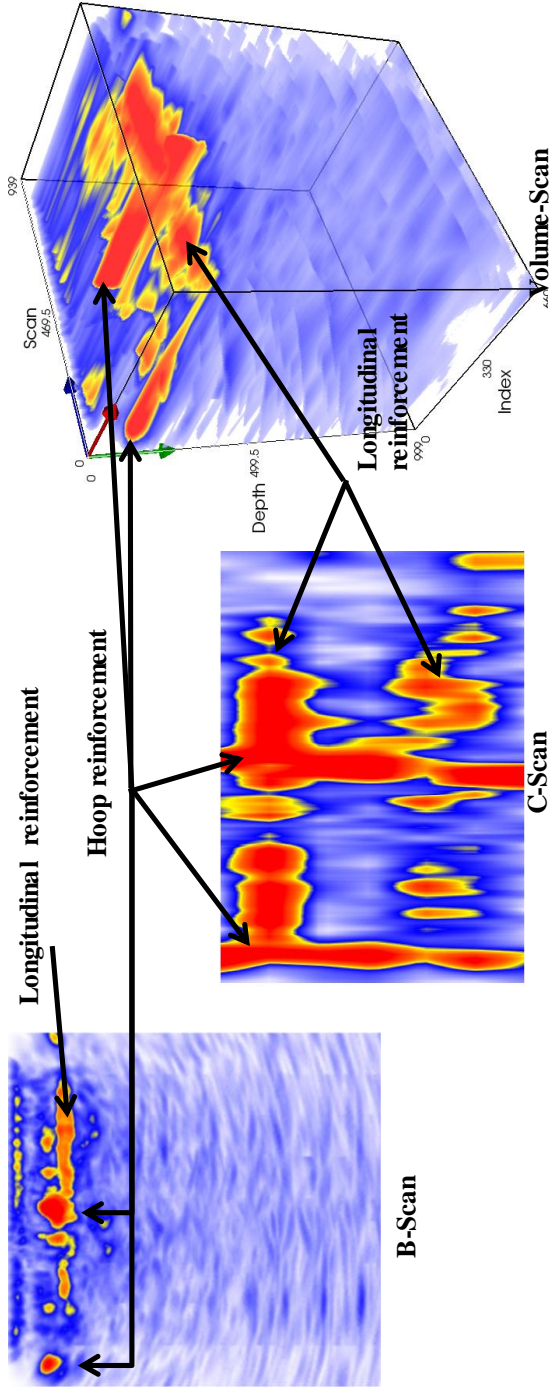


Defects	Notes	Backsurface	Reinf. Detail	$V_{shear} = 2159$ m/s X-step: 150 mm Y-step: 50 mm Max Depth: 1000 mm Frequency: 50 kHz
No significant defect noticed.	Area tested on surface of tile; hair-line crack.	Not discernible	Hoop Reinf. ~5.1" deep @ ~16.3" O.C. Longitudinal Reinf: On bottom (possibly on top as well) @ ~14.0" O.C.	Glenwood Springs, CO Hanging Lake Tunnel HLT 10.5-13 Interior Tile Lining TAMU/TTI 10/2011



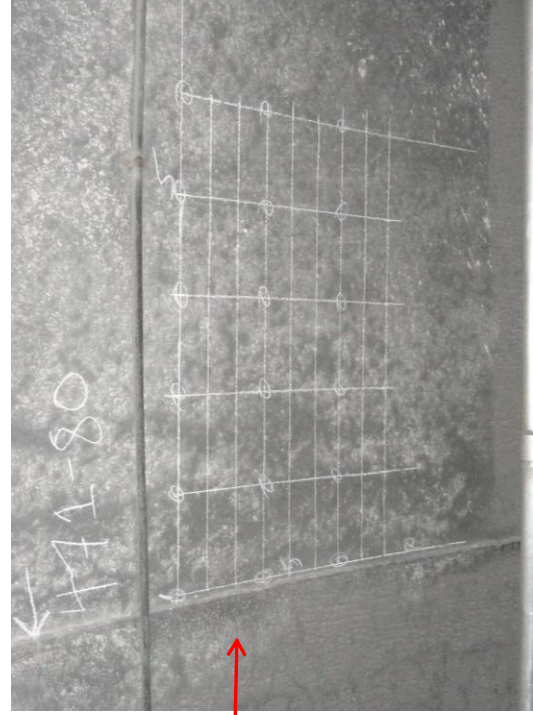
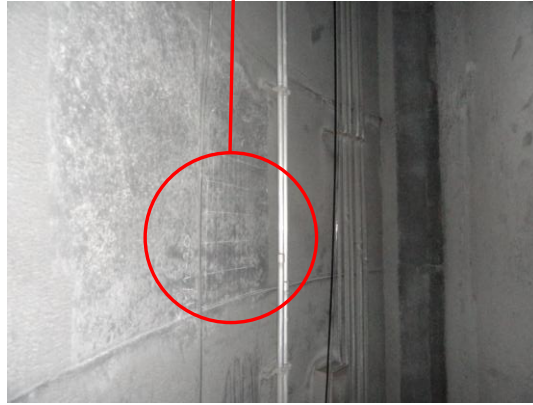
## Hanging Lake Tunnel, Glenwood Springs, CO

Defects	Notes	Backsurface	Reinf. Detail
No significant defect noticed.	Area tested on surface of tile; hair-line crack.	Not discernible	Hoop Reinf. ~5.1" deep @ ~16.3" O.C. Longitudinal Reinf: On bottom (possibly on top as well) @ ~14.0" O.C.
V <sub>shear</sub> = 2159 m/s X-step: 150 mm Y-step: 50 mm Max Depth: 1000 mm Frequency: 50 kHz Glenwood Springs, CO Hanging Lake Tunnel HLT 10.5-13 Interior Tile Lining TAMU/TTI 10/2011			



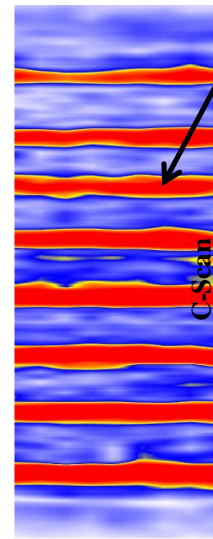
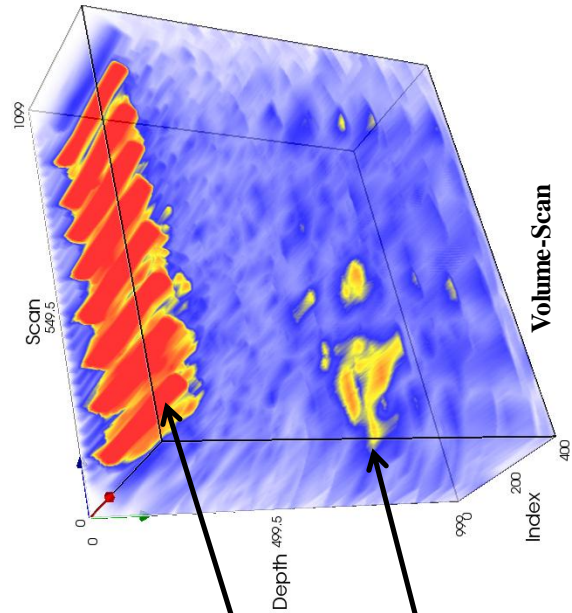
## Chesapeake Channel Tunnel, Norfolk, VA

Defects	Notes	Backsurface	Reinf. Detail	V <sub>shear</sub> = 2710 m/s X-step: 150 mm Y-step: 50 mm Max Depth: 1000 mm Frequency: 50 kHz
No significant defect noticed.	Area tested as representative of "sound" concrete. Also, GPR data revealed different steel composition (c.f. with CBBT 10.11-3,4).	~24.7"	Hoop Reinf. ~2.4" deep @ ~4.4" O.C. Longitudinal Reinf: On bottom	Norfolk, VA Chesapeake Tunnel CBBT 10.11-1, 2 Sta. 471+80 TAMU/TTI 10/2011

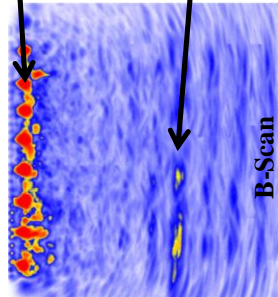


# Chesapeake Channel Tunnel, Norfolk, VA

Defects	Notes	Backsurface	Reinf. Detail	$V_{shear} = 2710 \text{ m/s}$ X-step: 150 mm Y-step: 50 mm Max Depth: 1000 mm Frequency: 50 kHz Norfolk, VA Chesapeake Tunnel CBBT 10.11-1, 2 Sta. 471+80 TAMU/TTI 10/2011
No significant defect noticed.	Area tested as representative of "sound" concrete. Also, GPR data revealed different steel composition (c.f. with CBBT 10.11-3,4).	~24.7"	Hoop Reinf. ~2.4" deep @ ~4.4" O.C. Longitudinal Reinf: On bottom	



Hoop reinforcement

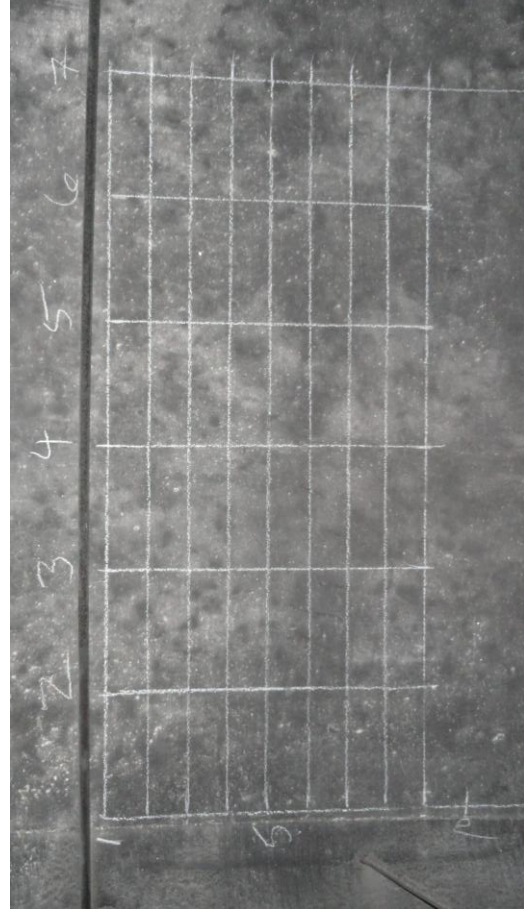


Backwall reflection

## Chesapeake Channel Tunnel, Norfolk, VA

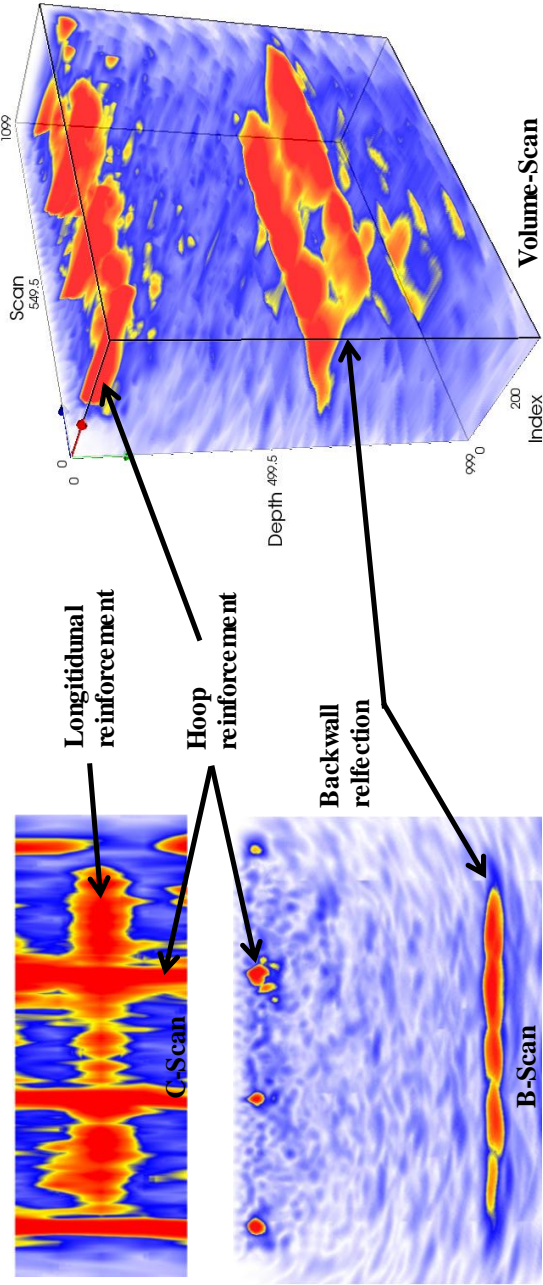
Defects	Notes	Backsurface	Reinf. Detail
<p>No significant defect noticed.</p>	<p>Area tested as representative of "sound" concrete. Also, GPR data revealed different steel composition (c.f. with CBBT 10.11-1, 2).</p>	<p>~24.4"</p>	<p>Hoop Reinf. ~2.3" deep @ ~11.8" O.C. Longitudinal Reinf: On bottom</p>

$V_{shear} = 2710 \text{ m/s}$   
 X-step: 150 mm  
 Y-step: 50 mm  
 Max Depth: 1000 mm  
 Frequency: 50 kHz  
 Norfolk, VA  
 Chesapeake Channel Tunnel  
 CBBT 10.11-3, 4  
 Sta. 473+56  
 TAMU/TTI 10/2011



# Chesapeake Channel Tunnel, Norfolk, VA

<p>Defects</p> <p>No significant defect noticed.</p>	<p>Notes</p> <p>Area tested as representative of "sound" concrete. Also, GPR data revealed different steel composition (c.f. with CBBT 10.11-1, 2).</p>	<p>Backsurface</p> <p>~24.4"</p>	<p>Reinf. Detail</p> <p>Hoop Reinf. ~2.3" deep @ ~11.8" O.C. Longitudinal Reinf: On bottom</p>	<p><math>V_{shear} = 2710</math> m/s  X-step: 150 mm  Y-step: 50 mm  Max Depth: 1000 mm  Frequency: 50 kHz  Norfolk, VA  Chesapeake Channel Tunnel  CBBT 10.11-3, 4  Sta. 473+56  TAMU/TTI 10/2011</p>
--	---	----------------------------------	--	--

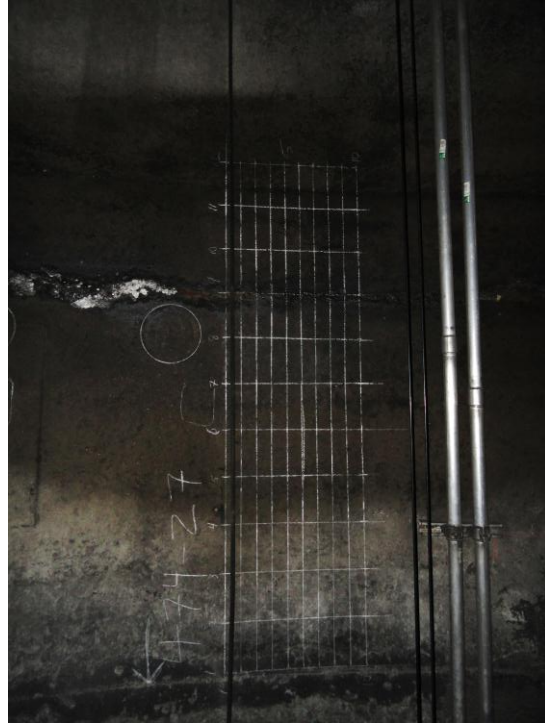




# Chesapeake Channel Tunnel, Norfolk, VA

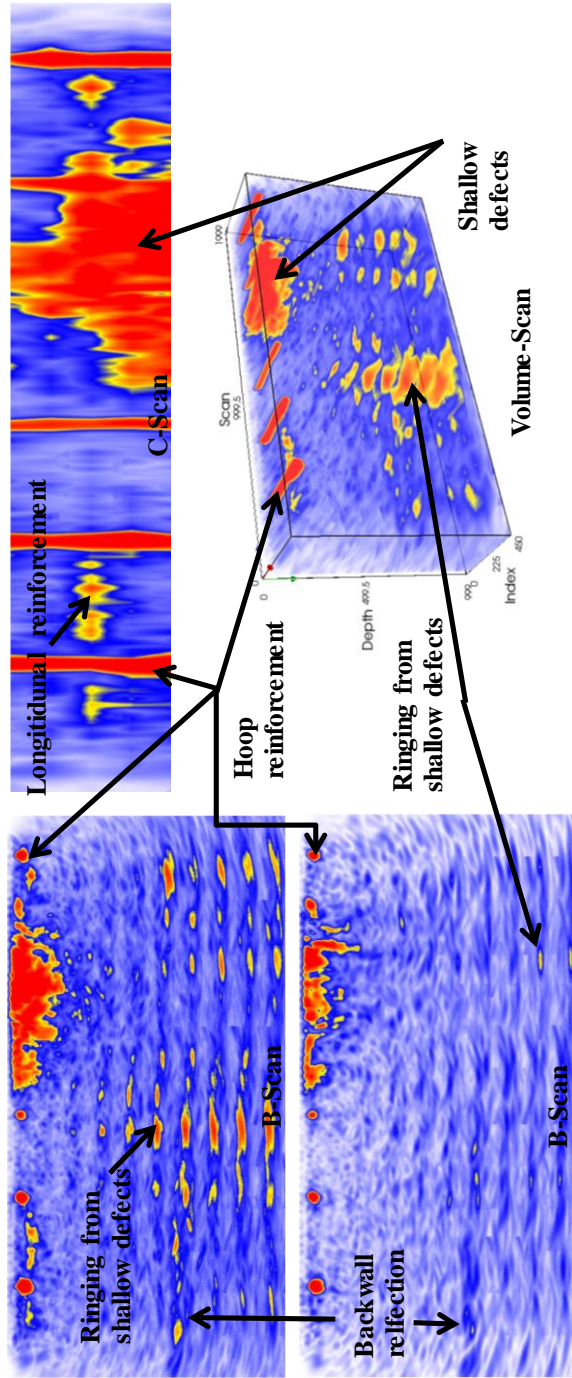


Defects	Notes	Backsurface	Reinf. Detail	$V_{shear} = 2710 \text{ m/s}$ X-step: 150 mm Y-step: 50 mm Max Depth: 1000 mm Frequency: 50 kHz Norfolk, VA Chesapeake Channel Tunnel CBBT 10.11-5 Sta. 474+27 TAMU/TTI 10/2011
Significant shallow defects, such as shallow cracks (~9" deep) and possibly shallow delaminations (~2" deep), which seem to produce the ringing.	Area tested because of "five" crack. Significant ringing may suggest debonding of longitudinal reinforcement.	~24.1"	Hoop Reinf: ~2.0"-2.6" deep @ ~12.0" O.C. Longitudinal Reinf: On bottom	



# Chesapeake Channel Tunnel, Norfolk, VA

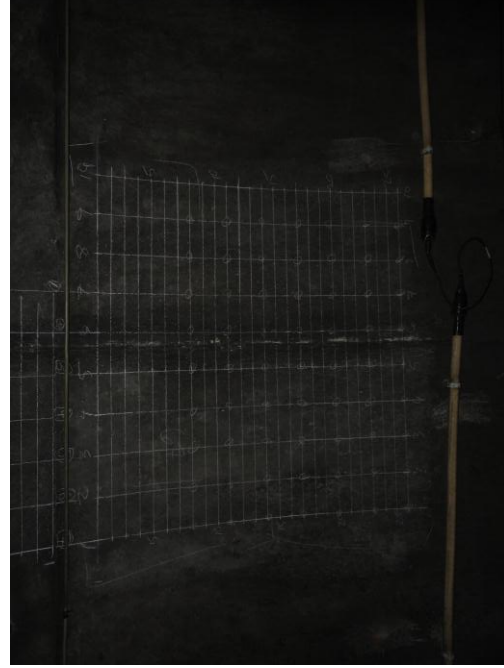
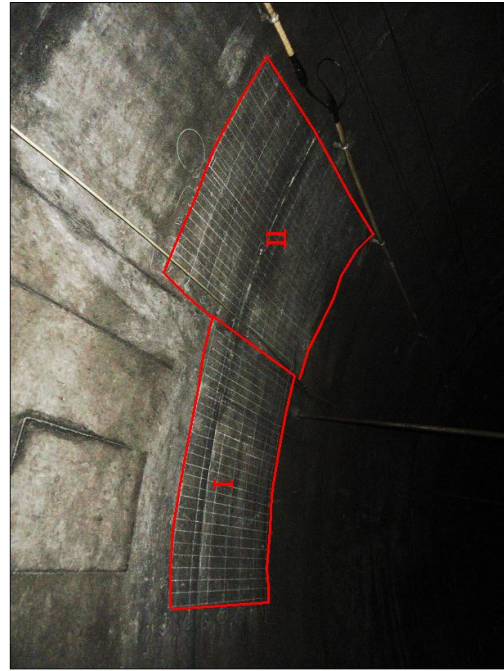
Defects	Notes	Backsurface	Reinf. Detail	$V_{shear} = 2710 \text{ m/s}$ X-step: 150 mm Y-step: 50 mm Max Depth: 1000 mm Frequency: 50 kHz Norfolk, VA Chesapeake Channel Tunnel CBBT 10.11-5 Sta. 474+27 TAMU/TTI 10/2011
Significant shallow defects, such as shallow cracks (~9" deep) and possibly shallow delaminations (~2" deep), which seem to produce the ringing.	Area tested because of "five" crack. Significant ringing may suggest debonding of longitudinal reinforcement.	~24.1"	Hoop Reinf: ~2.0"-2.6" deep @ ~12.0" O.C. Longitudinal Reinf: On bottom	



# Chesapeake Channel Tunnel, Norfolk, VA

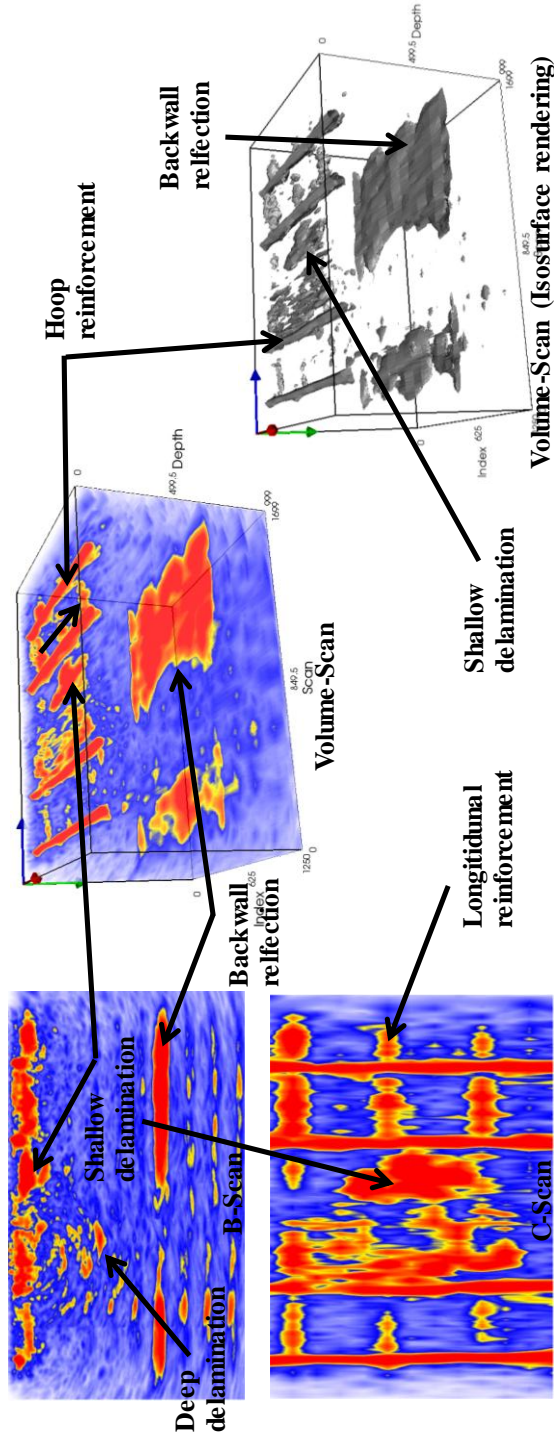


Defects	Notes	Backsurface	Reinf. Detail	$V_{shear} = 2710 \text{ m/s}$ X-step: 150 mm Y-step: 50 mm Max Depth: 1000 mm Frequency: 50 kHz Norfolk, VA Chesapeake Channel Tunnel CBBT 10.11-7, 8 (Region II) Sta. 486+67 TAMU/TTI 10/2011
Hammer tapping revealed hollow region as shown by shallow reflective region in the C and B-scans. Significant cupped-shaped delaminations as deep as 19.2"	Area tested because of high dielectric reading from GPR scan. No significant visual distress noticeable, but hammer sounding revealed shallow delamination in Region II.	24.1-26.0"	Hoop Reinf. ~2.2" deep @ ~12.1" O.C. Longitudinal Reinf: On bottom @ 16.2" O.C.	

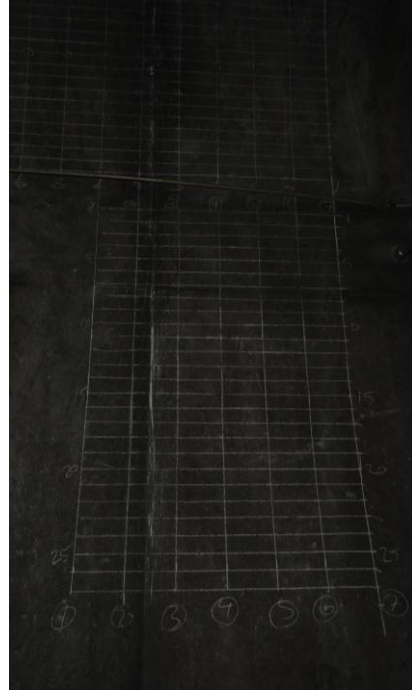
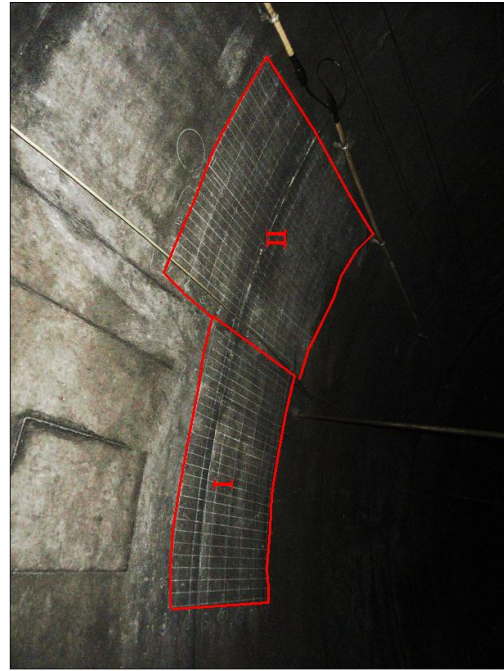


## Chesapeake Channel Tunnel, Norfolk, VA

Defects	Notes	Backsurface	Reinf. Detail	$V_{shear} = 2710 \text{ m/s}$ X-step: 150 mm Y-step: 50 mm Max Depth: 1000 mm Frequency: 50 kHz Norfolk, VA Chesapeake Channel Tunnel CBBT 10.11-7, 8 (Region II) Sta. 486+67 TAMU/TTI 10/2011
Hammer tapping revealed hollow region as shown by shallow reflective region in the C and B-scans. Significant cupped-shaped delaminations as deep as 19.2"	Area tested because of high dielectric reading from GPR scan. No significant visual distress noticeable, but hammer sounding revealed shallow delamination in Region II.	24.1-26.0"	Hoop Reinf. ~2.2" deep @ ~12.1" O.C. Longitudinal Reinf: On bottom @ 16.2" O.C.	

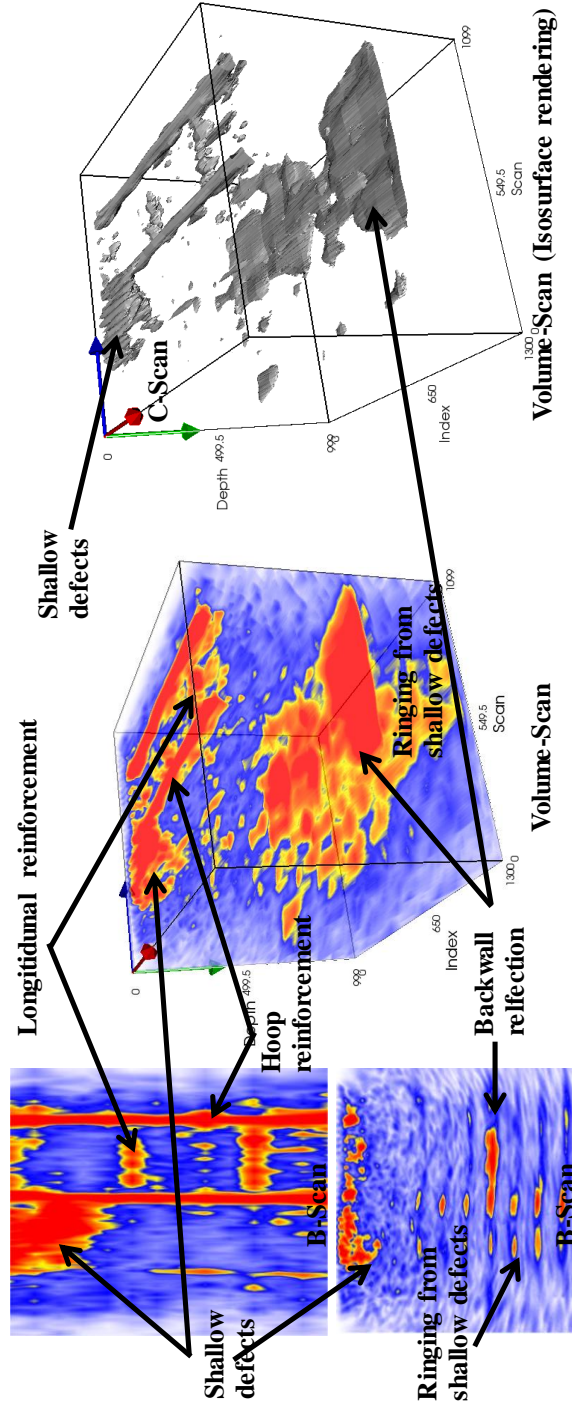


Defects	Notes	Backsurface	Reinf. Detail	$V_{shear} = 2710 \text{ m/s}$ X-step: 150 mm Y-step: 50 mm Max Depth: 1000 mm Frequency: 50 kHz Norfolk, VA Chesapeake Channel Tunnel CBBT 10.11-9 (Region I) Sta. 486+67 TAMU/TTI 10/2011
Significant cracks as deep as 8.6" deep.	Area tested because of high dielectric reading from GPR scan. No significant visual distress noticeable.	24.3-26.0"	Hoop Reinf: ~2.0"-3.0" deep @ ~12.2" O.C. Longitudinal Reinf: On bottom @ 19.8" O.C.	



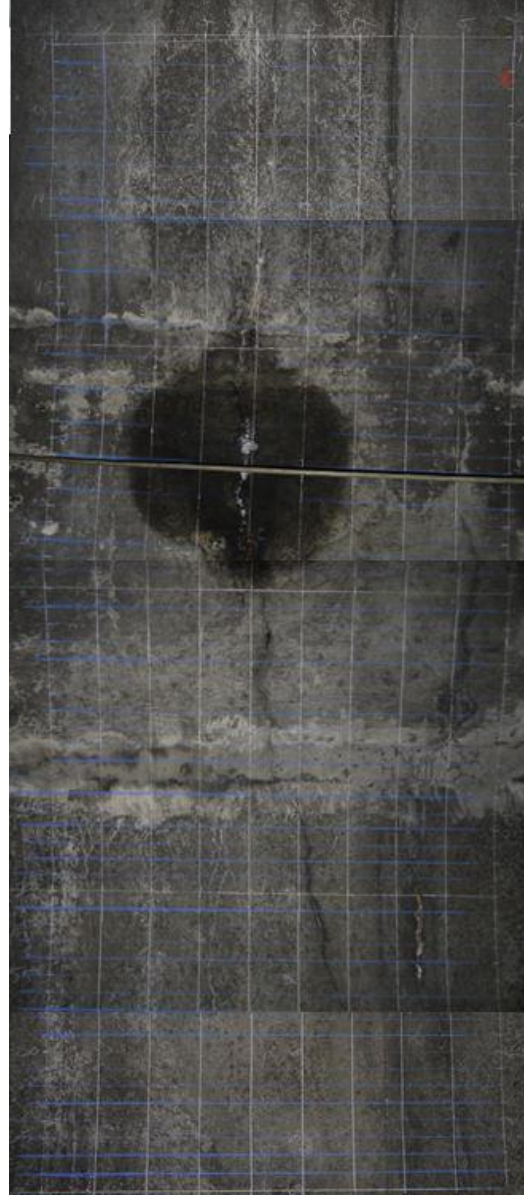
# Chesapeake Channel Tunnel, Norfolk, VA

Defects	Notes	Backsurface	Reinf. Detail	$V_{shear} = 2710 \text{ m/s}$ X-step: 150 mm Y-step: 50 mm Max Depth: 1000 mm Frequency: 50 kHz Norfolk, VA Chesapeake Channel Tunnel CBBT 10.11-9 (Region I) Sta. 486+67 TAMU/TTI 10/2011
Significant cracks as deep as 8.6" deep.	Area tested because of high dielectric reading from GPR scan. No significant visual distress noticeable.	24.3-26.0"	Hoop Reinf: ~2.0"-3.0" deep @ ~12.2" O.C. Longitudinal Reinf: On bottom @ 19.8" O.C.	



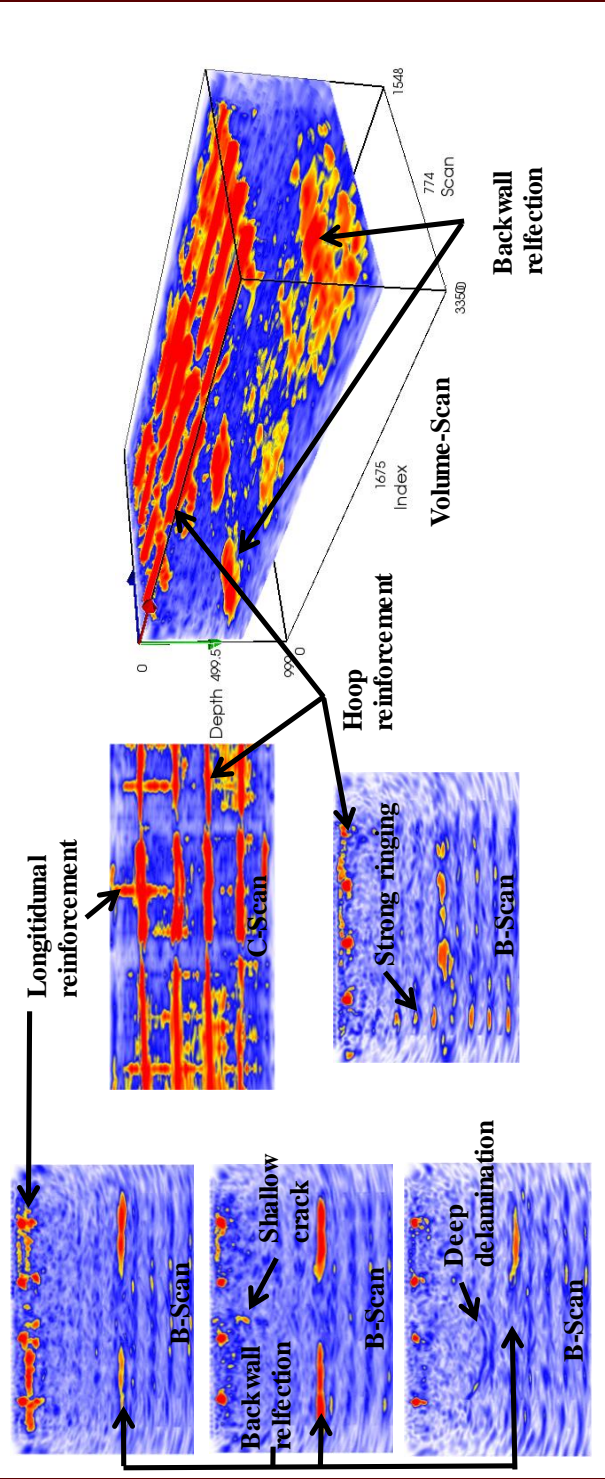
## Chesapeake Channel Tunnel, Norfolk, VA

Defects	Notes	Backsurface	Reinf. Detail	$V_{shear} = 2710 \text{ m/s}$ X-step: 150 mm Y-step: 50 mm Max Depth: 1000 mm Frequency: 50 kHz Norfolk, VA Chesapeake Channel Tunnel CBBT 10.11-10 Sta. 491+25 TAMU/TTI 10/2011
Heavy ringing made internal inspection difficult. Possible deep delamination (~17.7" deep and possibly 19" wide) and evidence of surface crack extending ~9.8" deep.	Area tested because of large surface crack and small area of water intrusion.	22.7-25.9"	Hoop Reinf: ~2.7"-3.2" deep @ ~11.7"-12.4" O.C. 2nd Layer of Hoop reinf. directly beneath top layer. Longitudinal Reinf: On bottom @ ~17.1" O.C.	



# Chesapeake Channel Tunnel, Norfolk, VA

<b>Defects</b> Heavy ringing made internal inspection difficult. Possible deep delamination (~17.7" deep and possibly 19" wide) and evidence of surface crack extending ~9.8" deep.	<b>Notes</b> Area tested because of large surface crack and small area of water intrusion.	<b>Backsurface</b> 22.7'-25.9"	<b>Reinf. Detail</b> Hoop Reinf: ~2.7"-3.2" deep @ ~11.7"-12.4" O.C. 2nd Layer of Hoop reinf. directly beneath top layer. Longitudinal Reinf: On bottom @ ~17.1" O.C.	V <sub>shear</sub> = 2710 m/s X-step: 150 mm Y-step: 50 mm Max Depth: 1000 mm Frequency: 50 kHz Norfolk, VA Chesapeake Channel Tunnel CBBT 10.11-10 Sta. 491+25 TAMU/TTI 10/2011
--	---	-----------------------------------	--	---





## Chesapeake Channel Tunnel, Norfolk, VA

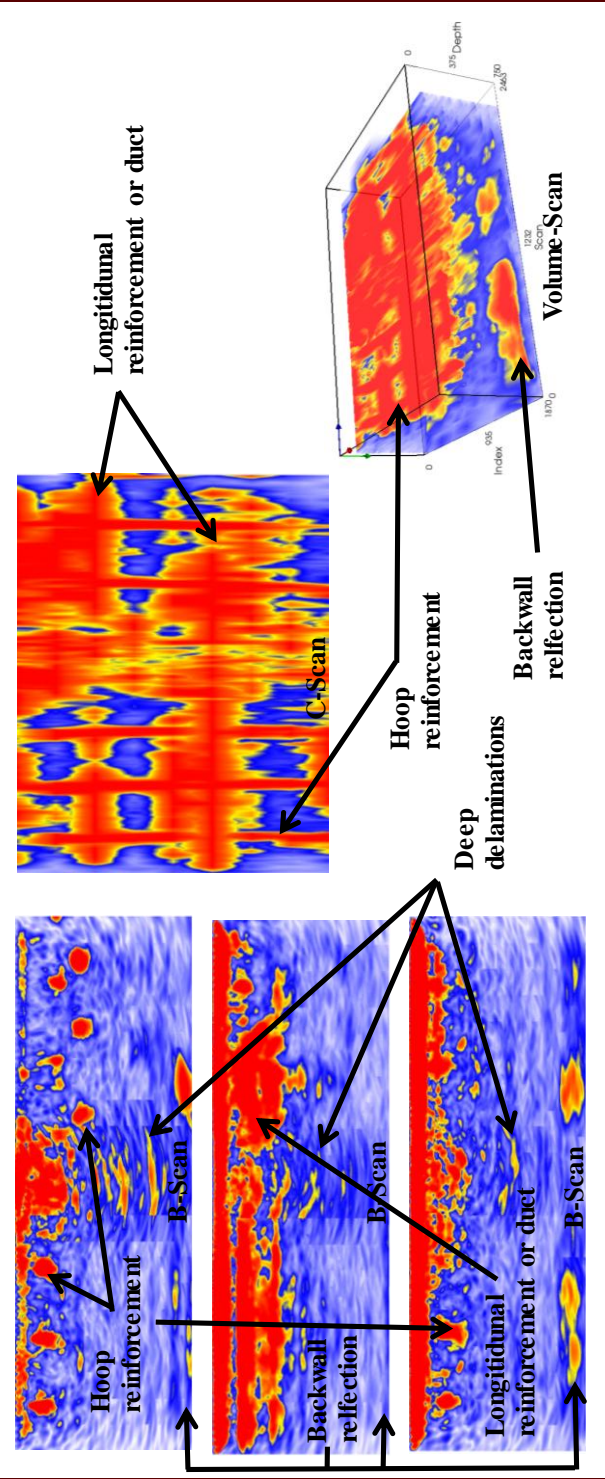


Defects	Notes	Backsurface	Reinf. Detail	V <sub>shear</sub> = 2710 m/s X-step: 110 mm Y-step: 110 mm Max Depth: 750 mm Frequency: 50 kHz Norfolk, VA Chesapeake Channel Tunnel CBBT TILE 10.11-11 Approx. Sta. 488 TAMU/TTI 10/2011
Heavy ringing made internal inspection difficult. Possible deep delamination (~15.7" deep and possibly 20.3" wide).	Area tested was tiled lining, over a joint where tile has debonded. Determined area via hammer sounding.	25.0-30.0"	Hoop Reinf: ~4.3"-7.7" deep @ ~12.1" O.C. 2nd layer of hoop reinf. seen briefly beneath top layer in one location, but this may be splice area. Longitudinal Reinf: On bottom @ ~13.0" O.C.	



# Chesapeake Channel Tunnel, Norfolk, VA

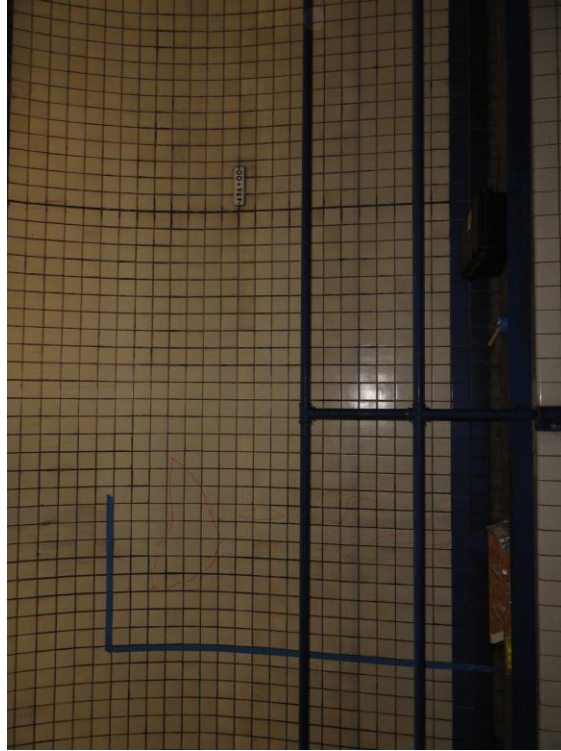
<b>Defects</b> Heavy ringing made internal inspection difficult. Possible deep delamination (~15.7" deep and possibly 20.3" wide).	<b>Notes</b> Area tested was tiled lining, over a joint where tile has debonded. Determined area via hammer sounding.	<b>Backsurface</b> 25.0-30.0"	<b>Reinf. Detail</b> Hoop Reinf: ~4.3"-7.7" deep @ ~12.1" O.C. 2nd layer of hoop reinf. seen briefly beneath top layer in one location, but this may be splice area. Longitudinal Reinf: On bottom @ ~13.0" O.C.	$V_{shear} = 2710 \text{ m/s}$ X-step: 110 mm Y-step: 110 mm Max Depth: 750 mm Frequency: 50 kHz Norfolk, VA Chesapeake Channel Tunnel CBBT TILE 10.11-11 Approx. Sta. 488 TAMU/TTI 10/2011
---	--	----------------------------------	---	--



## Chesapeake Channel Tunnel, Norfolk, VA

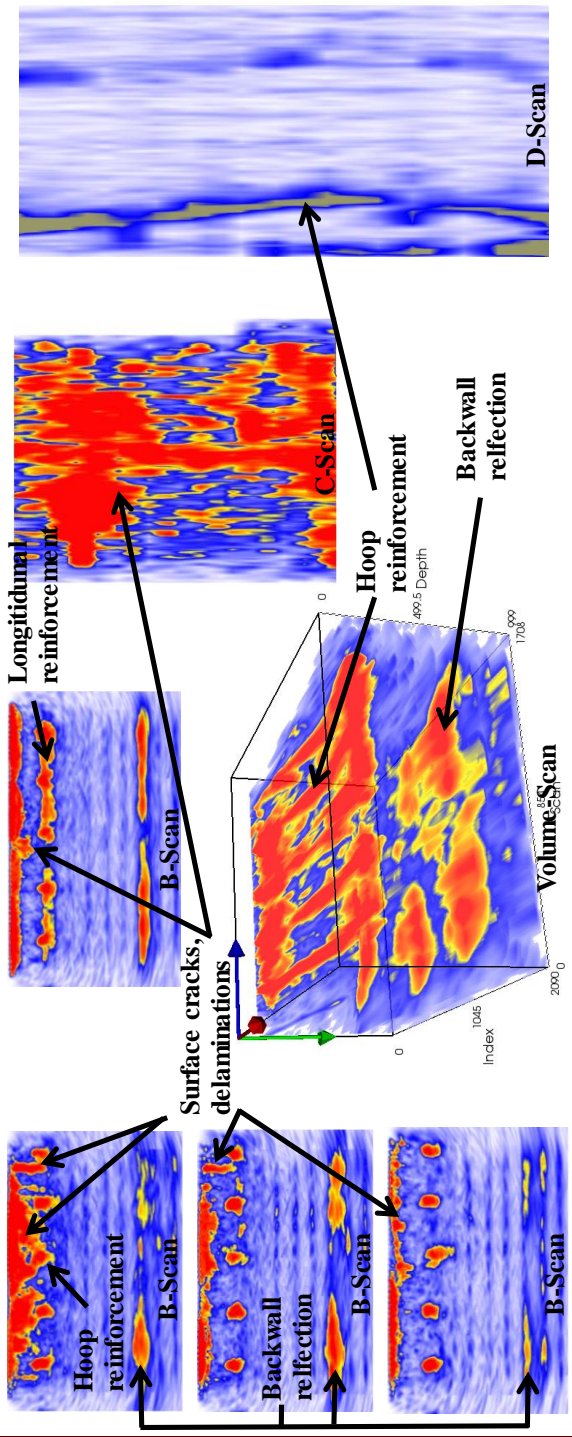


Defects	Notes	Backsurface	Reinf. Detail	V <sub>shear</sub> = 2710 m/s X-step: 110 mm Y-step: 110 mm Max Depth: 1000 mm Frequency: 50 kHz Norfolk, VA Chesapeake Channel Tunnel CBBT TILE 10.11-12 Sta. 486-09 TAMU/TTI 10/2011
Heavy ringing made internal inspection difficult. Possibly multiple cracks as deep as 8.6".	Area tested was tiled lining. Hammer sounding did not indicate debonding, but SPACETEC infrared scans showed area of question.	28.1-31.0"	Hoop Reinf: ~4.8"-9.4" deep @ ~11.7" O.C. Longitudinal Reinf: On bottom, possibly top as well, but may be duct.	



# Chesapeake Channel Tunnel, Norfolk, VA

<b>Defects</b> Heavy ringing made internal inspection difficult. Possibly multiple cracks as deep as 8.6".	<b>Notes</b> Area tested was tiled lining. Hammer sounding did not indicate debonding, but SPACETEC infrared scans showed area of question.	<b>Backsurface</b> 28.1-31.0"	<b>Reinf. Detail</b> Hoop Reinf: ~4.8"-9.4" deep @ ~11.7" O.C. Longitudinal Reinf: On bottom, possibly top as well, but may be duct.	$V_{shear} = 2710 \text{ m/s}$ X-step: 110 mm Y-step: 110 mm Max Depth: 1000 mm Frequency: 50 kHz Norfolk, VA Chesapeake Channel Tunnel CBBT TILE 10.11-12 Sta. 486-09 TAMU/TTI 10/2011
---	--	----------------------------------	--	--



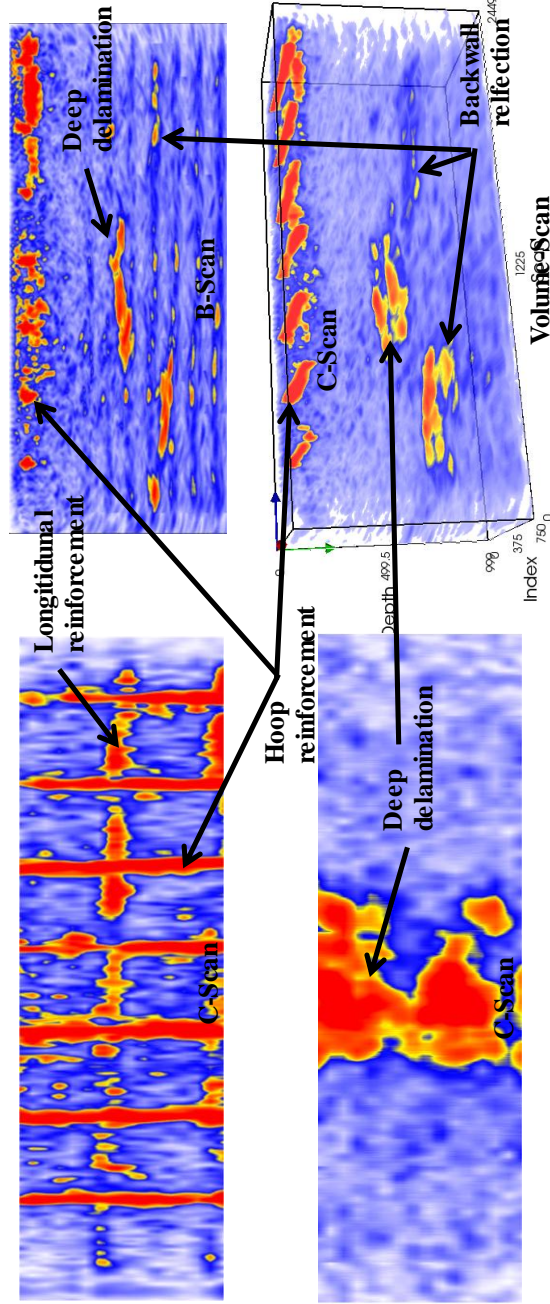
## Chesapeake Channel Tunnel, Norfolk, VA

Defects	Notes	Backsurface	Reinf. Detail
Apparent delamination 20.2" deep, and 27.4" wide.	Area tested because of surface crack and varying backwall reflections from single-point evaluations.	26.6"-28.4"	Hoop Reinf: ~2.0"-3.6" deep @ 12.1" O.C. Longitudinal Reinf: On bottom.
$V_{shear} = 2710 \text{ m/s}$ X-step: 150 mm Y-step: 50 mm Max Depth: 1000 mm Frequency: 50 kHz Norfolk, VA Chesapeake Channel Tunnel CBBT 10.11-13 Sta. 481-76 TAMU/TTI 10/2011			



## Chesapeake Channel Tunnel, Norfolk, VA

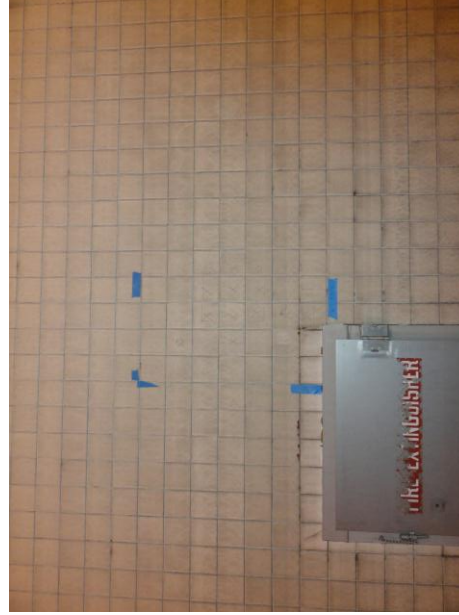
Defects	Notes	Backsurface	Reinf. Detail	V <sub>shear</sub> = 2710 m/s X-step: 150 mm Y-step: 50 mm Max Depth: 1000 mm Frequency: 50 kHz Norfolk, VA
Apparent delamination 20.2" deep, and 27.4" wide.	Area tested because of surface crack and varying backwall reflections from single-point evaluations.	26.6"-28.4"	Hoop Reinf: ~2.0"-3.6" deep @ 12.1" O.C. Longitudinal Reinf: On bottom.	Chesapeake Channel Tunnel CBBT 10.11-13 Sta. 481-76 TAMU/TTI 10/2011



# Washburn Tunnel, Houston, TX

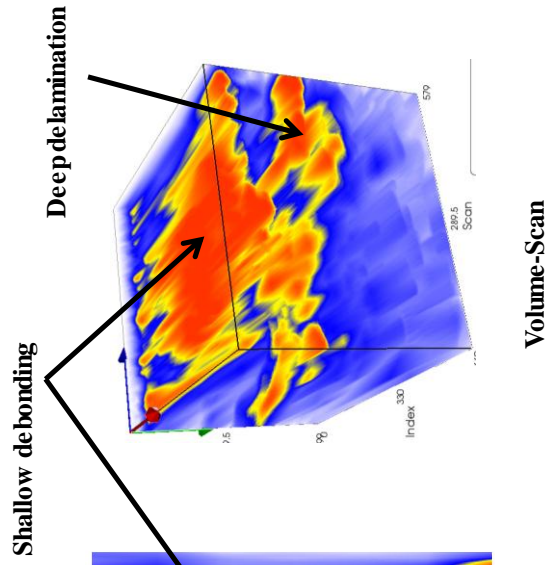
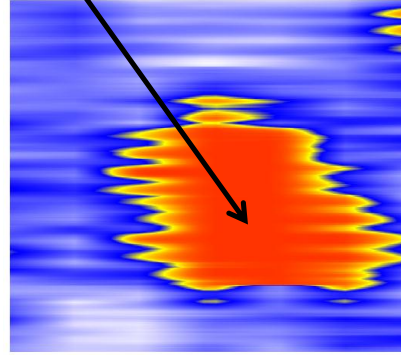
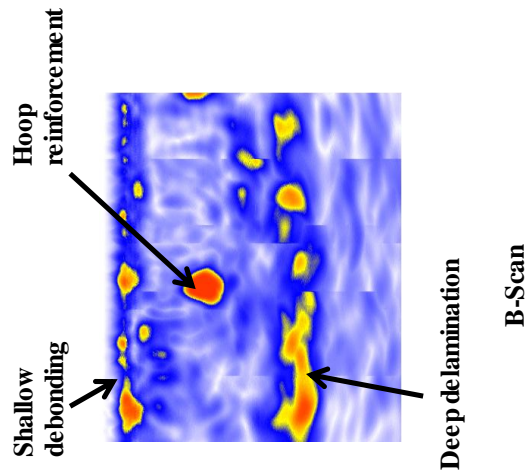


Defects	Notes	Backsurface	Reinf. Detail	$V_{shear} = 2710 \text{ m/s}$ X-step: 110 mm Y-step: 110 mm Max Depth: 500 mm Frequency: 50 kHz
Significant shallow debonding/delamination. Deep delamination approximately 1.3" deep (B-scan image)	Area tested because of debonding located via hammer sounding.	Not discernible	Hoop Reinf. ~6.8" deep	Houston, TX Washburn Tunnel WT 9.16-1 West Side TAMU/TTI 9/2011



## Washburn Tunnel, Houston, TX

Defects	Notes	Backsurface	Reinf. Detail	V <sub>shear</sub> = 2710 m/s X-step: 110 mm Y-step: 110 mm Max Depth: 500 mm Frequency: 50 kHz
Significant shallow debonding/delamination. Deep delamination approximately 13" deep (B-scan image)	Area tested because of debonding located via hammer sounding.	Not discernible	Hoop Reinf. ~6.8" deep	Houston, TX Washburn Tunnel WT 9.16-1 West Side TAMU/TTI 9/2011



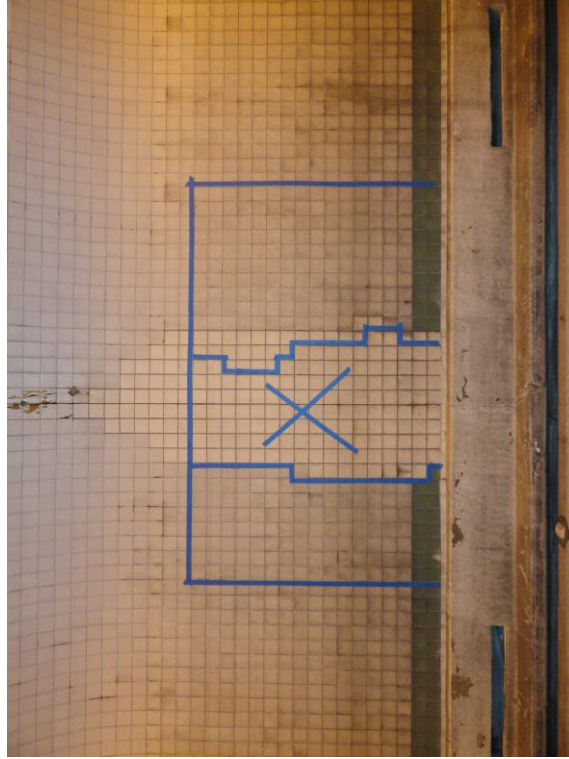


## Washburn Tunnel, Houston, TX



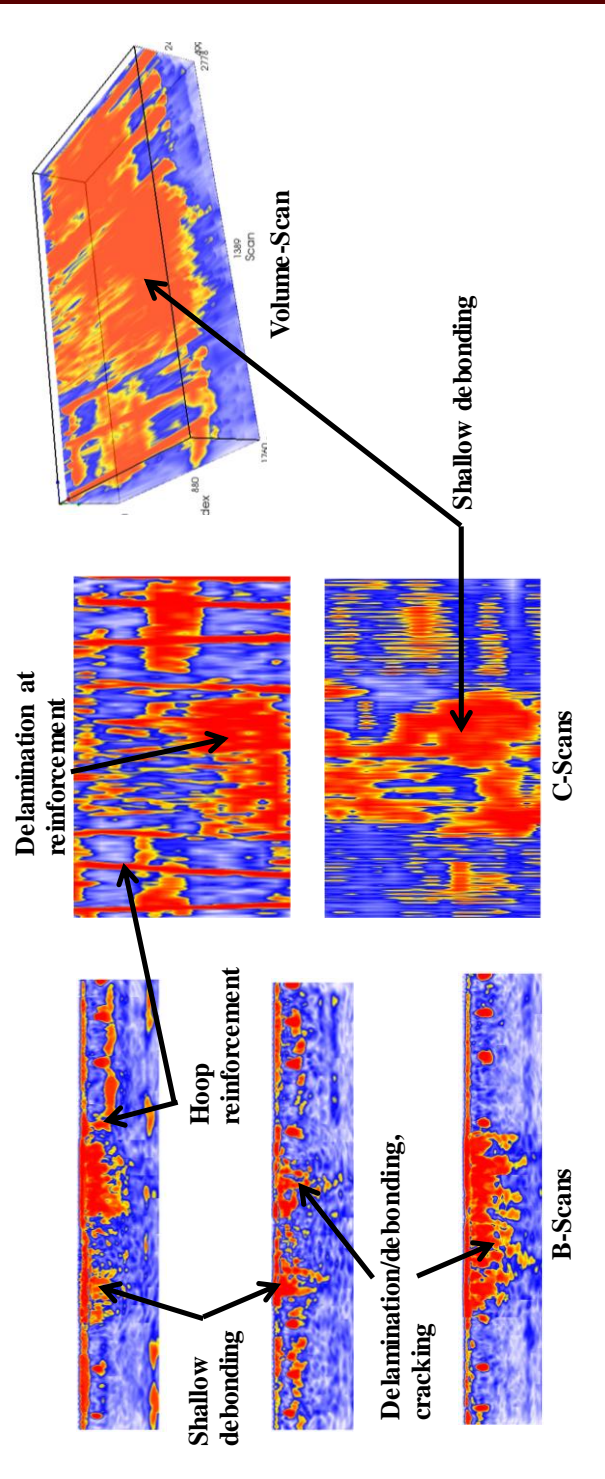
Defects	Notes	Backsurface	Reinf. Detail
<p>Significant shallow and deep debonding/delamination. Delaminations as deep as approximately 18" deep (B-scan image).</p>	<p>Area tested because of debonding located via hammer sounding.</p>	<p>Not discernible</p>	<p>Hoop Reinf: ~4.8"-5.2" deep @ 12.2 O.C. Longitudinal Reinf: On bottom</p>


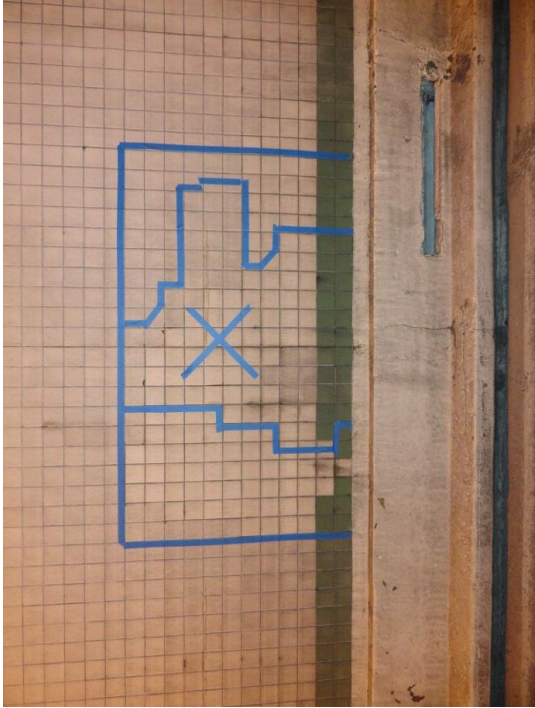
$V_{shear} = 2710 \text{ m/s}$   
 X-step: 110 mm  
 Y-step: 110 mm  
 Max Depth: 500 mm  
 Frequency: 50 kHz  
 Houston, TX  
 Washburn Tunnel  
 WT 9.16-2  
 West Side  
 TAMU/TTI 9/2011



# Washburn Tunnel, Houston, TX

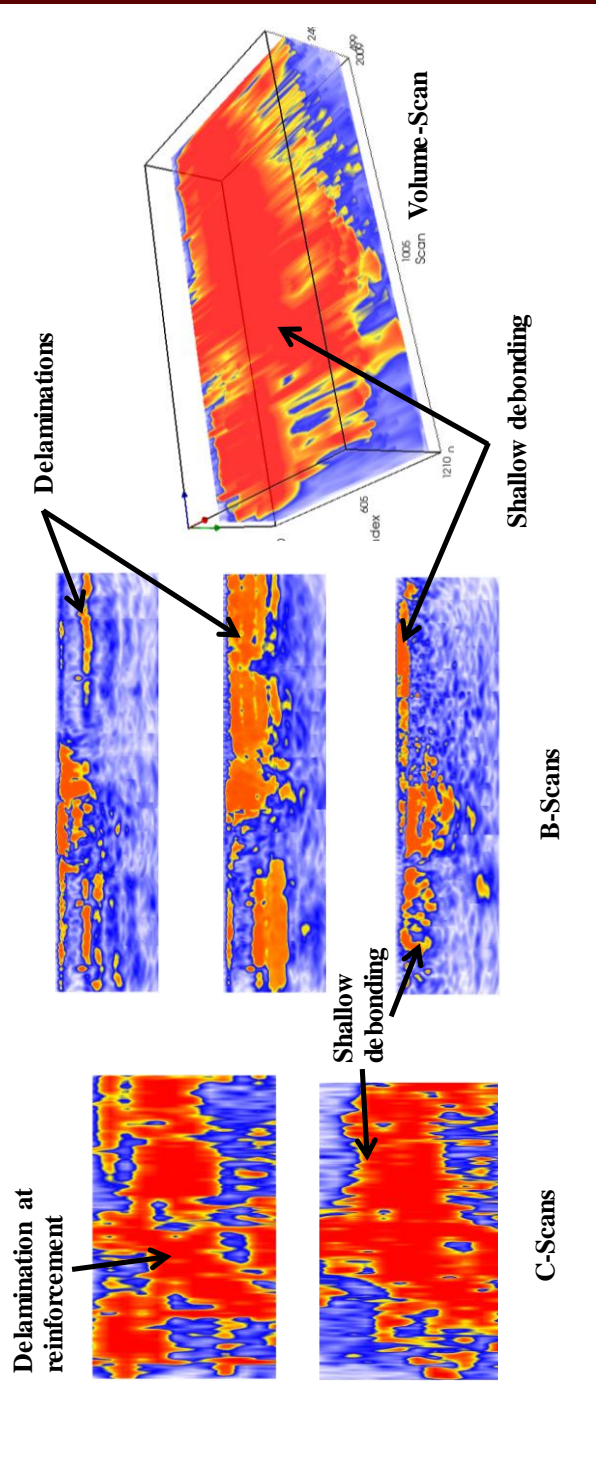
Defects	Notes	Backsurface	Reinf. Detail	$V_{shear} = 2710 \text{ m/s}$ X-step: 110 mm Y-step: 110 mm Max Depth: 500 mm Frequency: 50 kHz
Significant shallow and deep debonding/delamination. Delaminations as deep as approximately 18" deep (B-scan image).	Area tested because of debonding located via hammer sounding.	Not discernible	Hoop Reinf: ~4.8"-5.2" deep @ 12.2 O.C. Longitudinal Reinf: On bottom	Houston, TX Washburn Tunnel WT 9.16-2 West Side TAMU/TTI 9/2011



 <b>Washburn Tunnel, Houston, TX</b>			
Defects	Notes	Backsurface	Reinf. Detail
<p>Significant delaminations/debonding throughout. Delaminations as deep as 10.7" below surface.</p>	<p>Area tested because of delaminations determined by hammer sounding.</p>	<p>Not discernible</p>	<p>Hoop Reinf. ~4.9" deep @ 13.4" O.C. Longitudinal Reinf: On bottom</p>
		<p> <math>V_{shear} = 2710 \text{ m/s}</math>                      X-step: 110 mm                      Y-step: 110 mm                      Max Depth: 500 mm                      Frequency: 50 kHz                      Houston, TX                      Washburn Tunnel                      WT 9.16-3                      West Side                      TAMU/TTI 9/2011                 </p>	
			

# Washburn Tunnel, Houston, TX

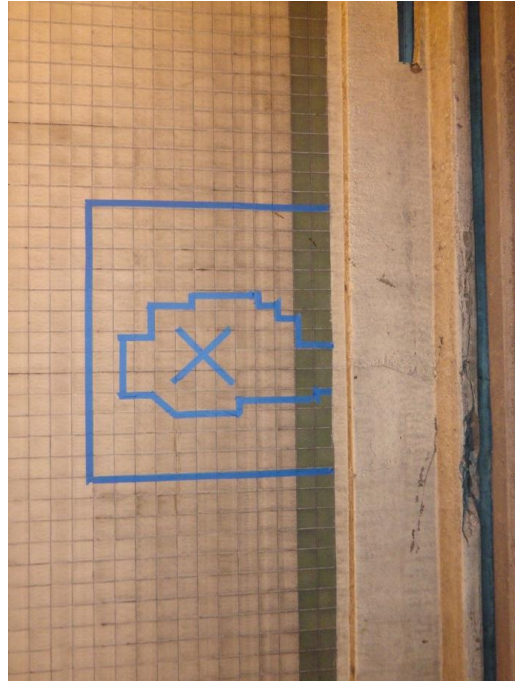
Defects	Notes	Backsurface	Reinf. Detail	$V_{shear} = 2710 \text{ m/s}$ X-step: 110 mm Y-step: 110 mm Max Depth: 500 mm Frequency: 50 kHz
Significant delaminations/debonding throughout. Delaminations as deep as 10.7" below surface.	Area tested because of delaminations determined by hammer sounding.	Not discernible	Hoop Reinf. ~4.9" deep @ 13.4" O.C. Longitudinal Reinf: On bottom	Houston, TX Washburn Tunnel WT 9.16-3 West Side TAMU/TTI 9/2011



## Washburn Tunnel, Houston, TX

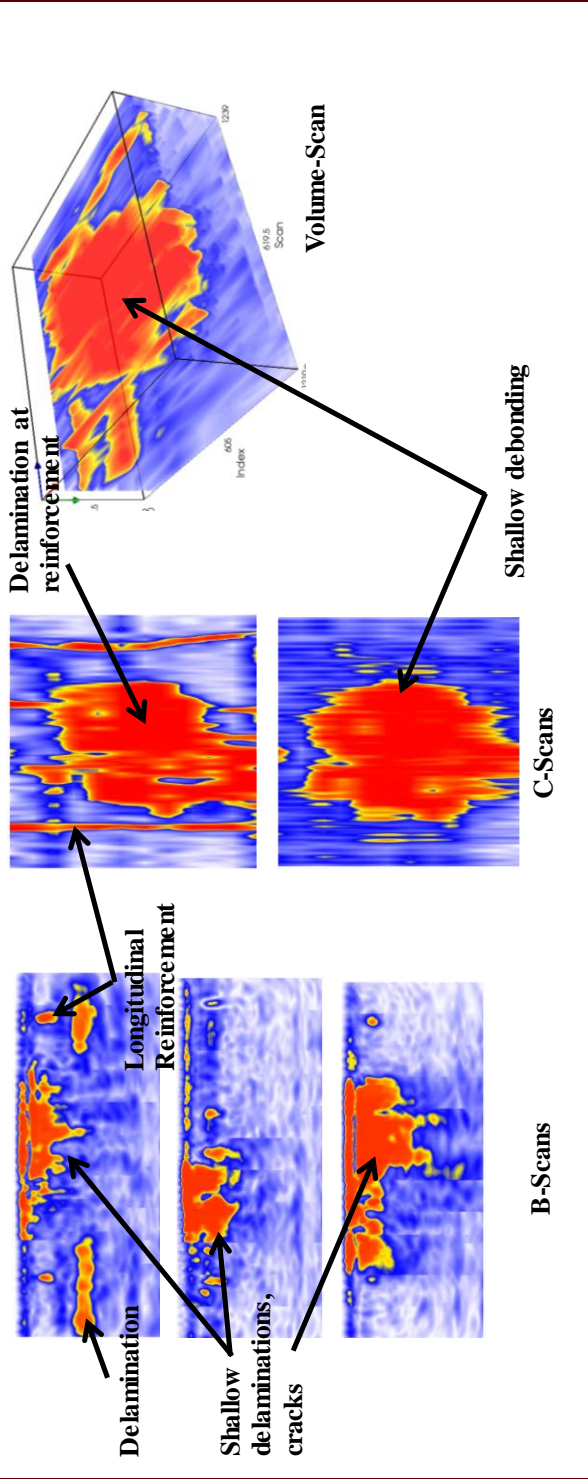


Defects	Notes	Backsurface	Reinf. Detail
Significant delaminations/debonding throughout. Possible delaminations 11.7" deep.	Area tested because of delaminations determined by hammer sounding.	Not discernible	Hoop Reinf. ~4.7" deep @ 11.7" O.C. Longitudinal Reinf: On bottom
		$V_{shear} = 2710 \text{ m/s}$ X-step: 110 mm Y-step: 110 mm Max Depth: 500 mm Frequency: 50 kHz Houston, TX Washburn Tunnel WT 9.16-4 West Side TAMU/TTI 9/2011	



## Washburn Tunnel, Houston, TX

Defects	Notes	Backsurface	Reinf. Detail	$V_{shear} = 2710 \text{ m/s}$ X-step: 110 mm Y-step: 110 mm Max Depth: 500 mm Frequency: 50 kHz
Significant delaminations/debonding throughout. Possible delaminations 11.7" deep.	Area tested because of delaminations determined by hammer sounding.	Not discernible	Hoop Reinf. ~4.7" deep @ 11.7" O.C. Longitudinal Reinf: On bottom	Houston, TX Washburn Tunnel WT 9.16-4 West Side TAMU/TTI 9/2011



## Interstate 20, Ft. Worth, TX

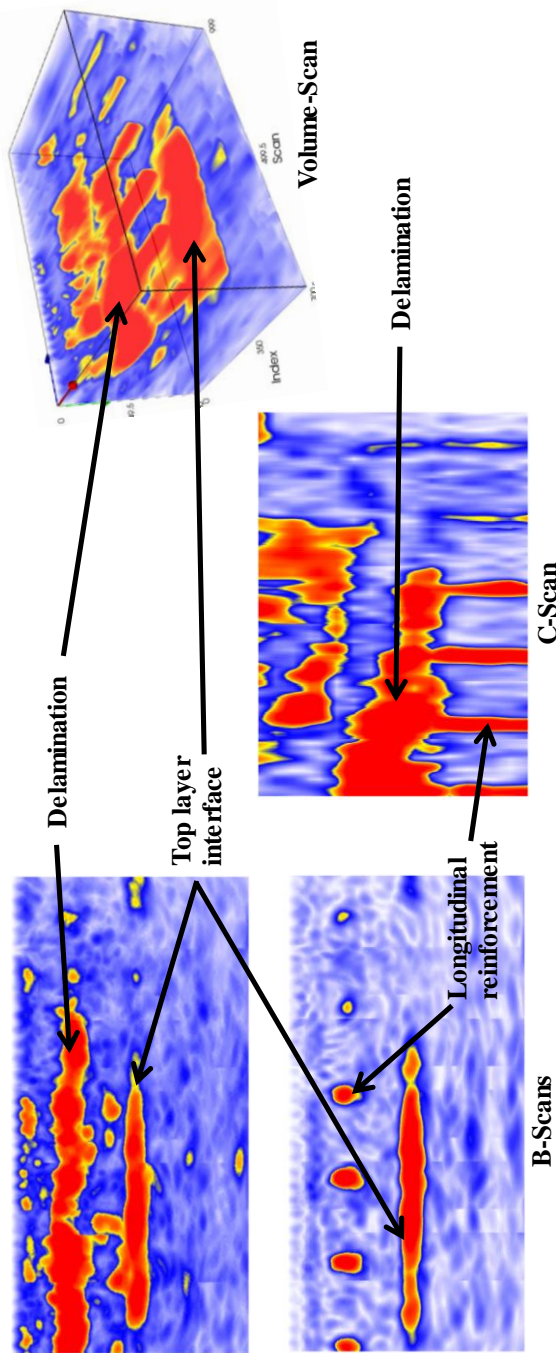


Defects	Notes	Backsurface	Reinf. Detail	V <sub>shear</sub> = 2770 m/s X-step: 150 mm Y-step: 50 mm Max Depth: 500 mm Frequency: 50 kHz Ft. Worth, TX I-20 IH20 9.27-1 MP 426 + 0.5, RM 2871 TAMU/TTI 9/2011
Significant delamination on both sides of surface crack, ranging from 4.2" - 5.0" from top surface.	Area tested because of transverse surface cracking. Pavement depth confirmed by 2 cores, both indicating 10.2" thickness and one indicating 5.0" reinf. depth.	Top layer of pavement approximately 10.2" below surface.	Longitudinal Reinf.: ~4.6" - 5.0" deep @ 5.6" O.C. No transverse reinforcement located in this area.	



## Interstate 20, Ft. Worth, TX

Defects	Notes	Backsurface	Reinf. Detail	V <sub>shear</sub> = 2770 m/s X-step: 150 mm Y-step: 50 mm Max Depth: 500 mm Frequency: 50 kHz
Significant delamination on both sides of surface crack, ranging from 4.2" - 5.0" from top surface.	Area tested because of transverse surface cracking. Pavement depth confirmed by 2 cores, both indicating 10.2" thickness and one indicating 5.0" reinf. depth.	Top layer of pavement approximately 10.2" below surface.	Longitudinal Reinf.: ~4.6" - 5.0" deep @ 5.6" O.C. No transverse reinforcement located in this area.	Ft. Worth, TX I-20 IH20 9.27-1 MP 426 + 0.5, RM 2871 TAMU/TTI 9/2011



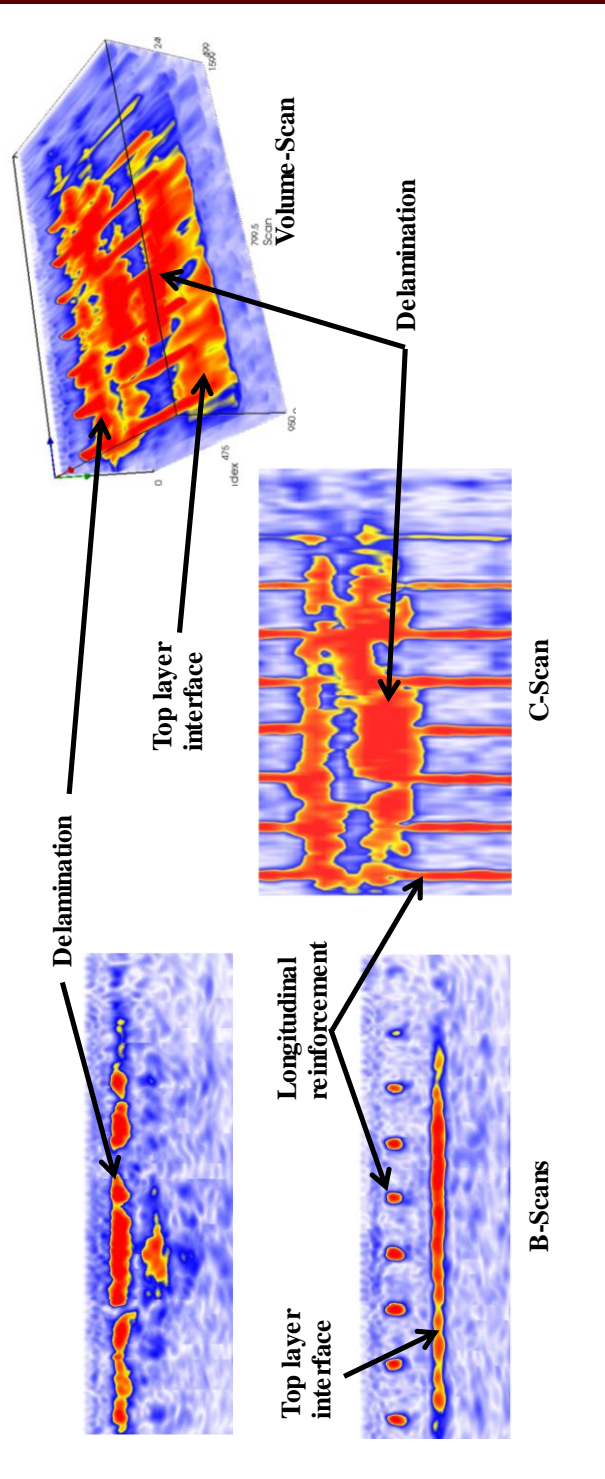


Defects	Notes	Backsurface	Reinf. Detail	$V_{shear} = 2770$ m/s X-step: 150 mm Y-step: 50 mm Max Depth: 500 mm Frequency: 50 kHz Ft. Worth, TX I-20 IH20 9.27-2 MP 426 + 0.5, RM 2871 TAMU/TTI 9/2011
Significant delamination on both sides of surface crack, ranging from 4.5" - 5.3" from top surface.	Area tested because of transverse surface cracking. Pavement depth confirmed by 2 cores, indicating 9.4" - 10.4" thickness.	Top layer of pavement approximately 10.4" below surface.	Longitudinal Reinf.: ~4.5" - 5.2" deep @ 7.1" O.C. No transverse reinforcement located in this area.	



## Interstate 20, Ft. Worth, TX

Defects	Notes	Backsurface	Reinf. Detail	$V_{shear} = 2770 \text{ m/s}$ X-step: 150 mm Y-step: 50 mm Max Depth: 500 mm Frequency: 50 kHz Ft. Worth, TX I-20 IH20 9.27-2 MP 426 + 0.5, RM 2871 TAMU/TTI 9/2011
Significant delamination on both sides of surface crack, ranging from 4.5" - 5.3" from top surface.	Area tested because of transverse surface cracking. Pavement depth confirmed by 2 cores, indicating 9.4" - 10.4" thickness.	Top layer of pavement approximately 10.4" below surface.	Longitudinal Reinf.: ~4.5" - 5.2" deep @ 7.1" O.C. No transverse reinforcement located in this area.	



## Interstate 20, Ft. Worth, TX

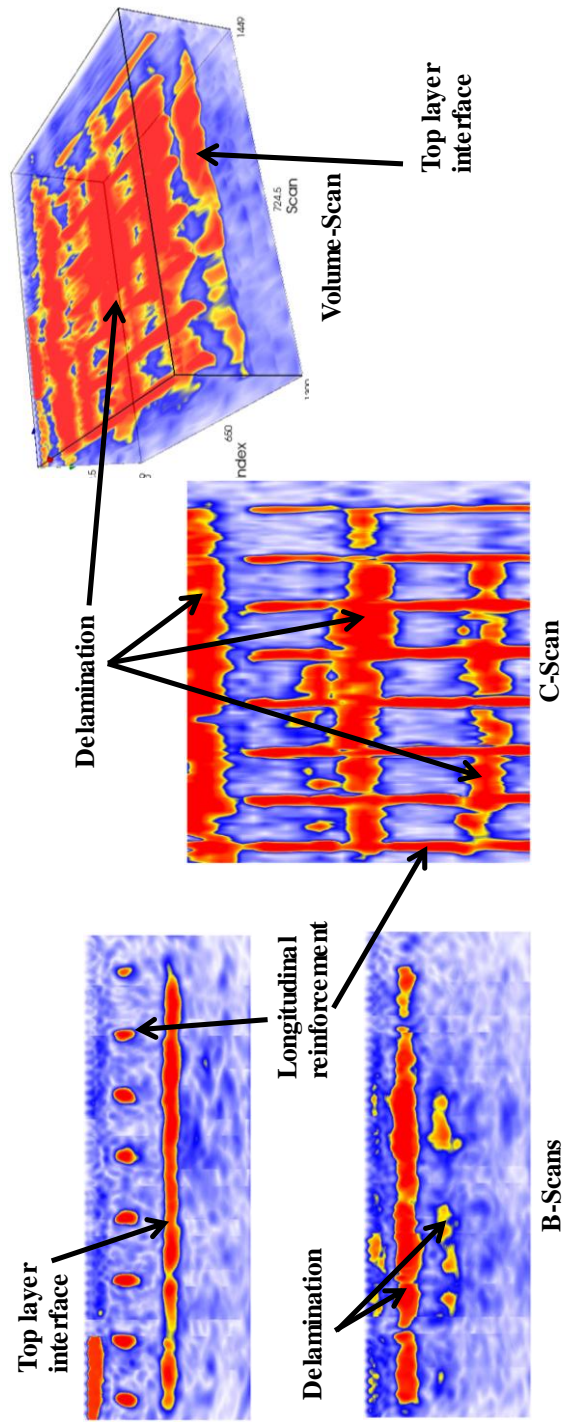





Defects	Notes	Backsurface	Reinf. Detail	V <sub>shear</sub> = 2770 m/s X-step: 150 mm Y-step: 50 mm Max Depth: 500 mm Frequency: 50 kHz Ft. Worth, TX I-20 IH20 9.27-3 MP 426 + 0.5, RM 2871 TAMU/TTI 9/2011
Significant delamination on both sides of surface crack, ranging from 4.6" - 5.1" from top surface.	Area tested because of transverse surface cracking. Pavement depth confirmed by 2 cores, indicating 10.2" thickness.	Top layer of pavement approximately 10.2" below surface.	Longitudinal Reinf.: ~4.8" - 5.0" deep @ 7.2" O.C. No transverse reinforcement located in this area.	



## Interstate 20, Ft. Worth, TX

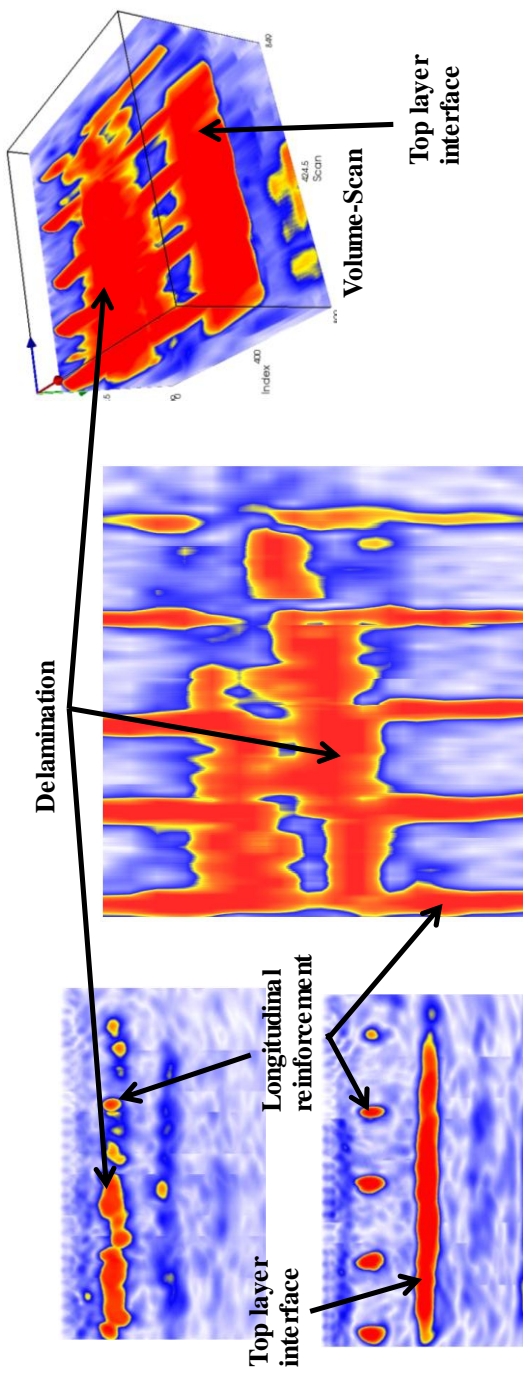
Defects	Notes	Backsurface	Reinf. Detail	V <sub>shear</sub> = 2770 m/s X-step: 150 mm Y-step: 50 mm Max Depth: 500 mm Frequency: 50 kHz
Significant delamination on both sides of surface crack, ranging from 4.6" - 5.1" from top surface.	Area tested because of transverse surface cracking. Pavement depth confirmed by 2 cores, indicating 10.2" thickness.	Top layer of pavement approximately 10.2" below surface.	Longitudinal Reinf.: ~4.8" - 5.0" deep @ 7.2" O.C. No transverse reinforcement located in this area.	Ft. Worth, TX I-20 IH20 9.27-3 MP 426 + 0.5, RM 2871 TAMU/TTI 9/2011



 <b>Interstate 20, Ft. Worth, TX</b>		 <b>Interstate 20, Ft. Worth, TX</b>	
<b>Defects</b> Significant delamination on both sides of surface crack, approximately 5.0" from top surface.	<b>Notes</b> Area tested because of transverse surface cracking. No cores taken in this location.	<b>Backsurface</b> Top layer of pavement approximately 10.1" below surface.	<b>Reinf. Detail</b> Longitudinal Reinf.: ~4.6"-5.2" deep @ 7.0" O.C. No transverse reinforcement located in this area.
			
		$V_{shear} = 2770 \text{ m/s}$ X-step: 150 mm Y-step: 50 mm Max Depth: 500 mm Frequency: 50 kHz Ft. Worth, TX I-20 IH20 9.27-5 MP 426 + 0.5, RM 2871 TAMU/TTI 9/2011	

## Interstate 20, Ft. Worth, TX

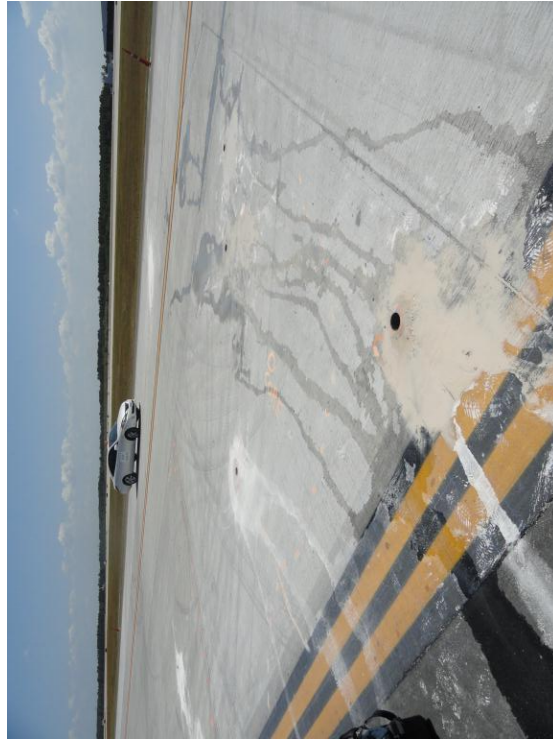
Defects	Notes	Backsurface	Reinf. Detail	V <sub>shear</sub> = 2770 m/s X-step: 150 mm Y-step: 50 mm Max Depth: 500 mm Frequency: 50 kHz Ft. Worth, TX I-20 IH20 9.27-5 MP 426 + 0.5, RM 2871 TAMU/TTI 9/2011
Significant delamination on both sides of surface crack, approximately 5.0" from top surface.	Area tested because of transverse surface cracking. No cores taken in this location.	Top layer of pavement approximately 10.1" below surface.	Longitudinal Reinf.: ~4.6"-5.2" deep @ 7.0" O.C. No transverse reinforcement located in this area.	



## George Bush International Airport, Houston, TX

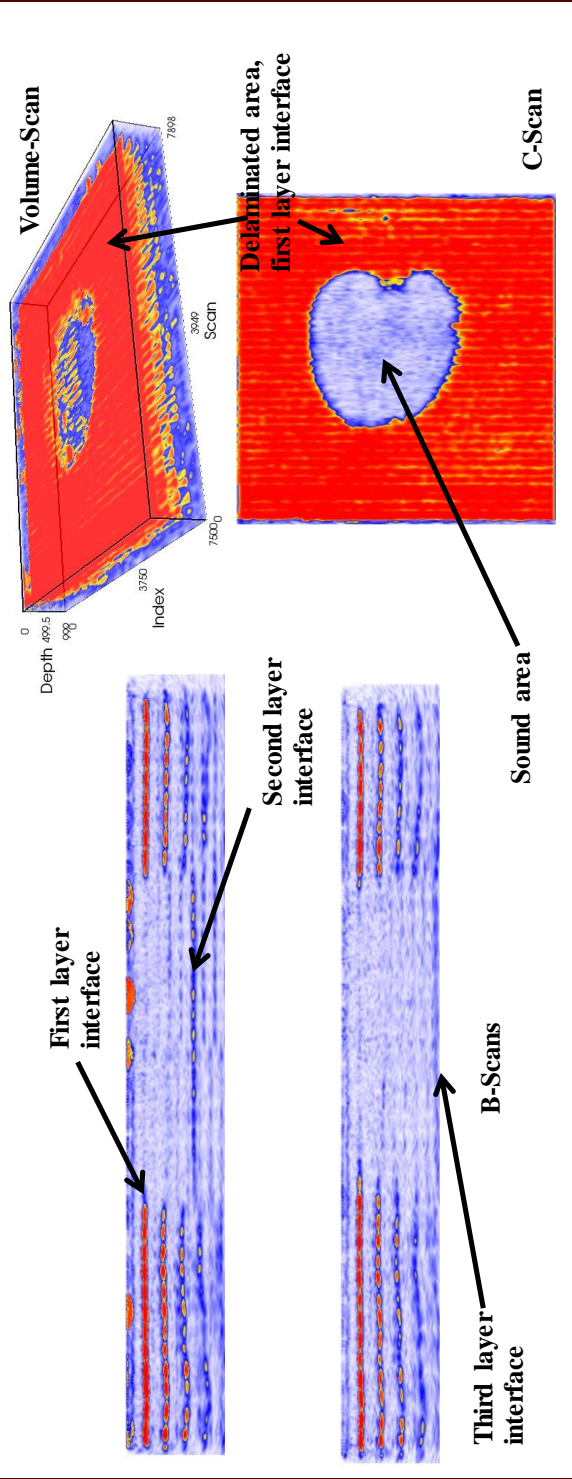


Defects	Notes	Backsurface	Reinf. Detail	V <sub>shear</sub> = 2885 m/s X-step: 200 mm Y-step: 100 mm Max Depth: 1000 mm Frequency: 50 kHz
Significant debonding at at runway/subbase (7.6"-8.1" deep), verified by coring. Possible further debonding in deeper layers (26.9" and 37.7" deep).	Area tested because of surface cracking, hammer sounding revealing possible delaminations. Image is of typical runway segment.	Top layer of pavement approximately 7.6"-8.1" below surface, second layer 26.9" below surface, third layer 37.7" below surface.	None	Houston, TX IAH IAH 6.9-1 Sta 83+00 T/W W A E TAMU/TTI 6/2011



George Bush International Airport, Houston, TX

Defects	Notes	Backsurface	Reinf. Detail	V <sub>shear</sub> = 2885 m/s X-step: 200 mm Y-step: 100 mm Max Depth: 1000 mm Frequency: 50 kHz
Significant debonding at at runway/subbase (7.6"-8.1" deep), verified by coring. Possible further debonding in deeper layers (26.9" and 37.7" deep).	Area tested because of surface cracking, hammer sounding revealing possible delaminations.	Top layer of pavement approximately 7.6"-8.1" below surface, second layer 26.9" below surface, third layer 37.7" below surface.	None	Houston, TX IAH IAH 6.9-1 Sta 83+00 T/W W A E TAMU/TTI 6/2011

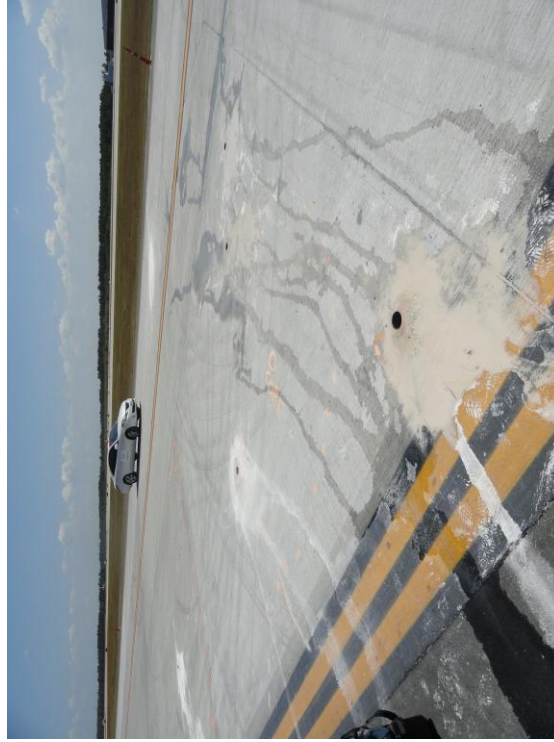




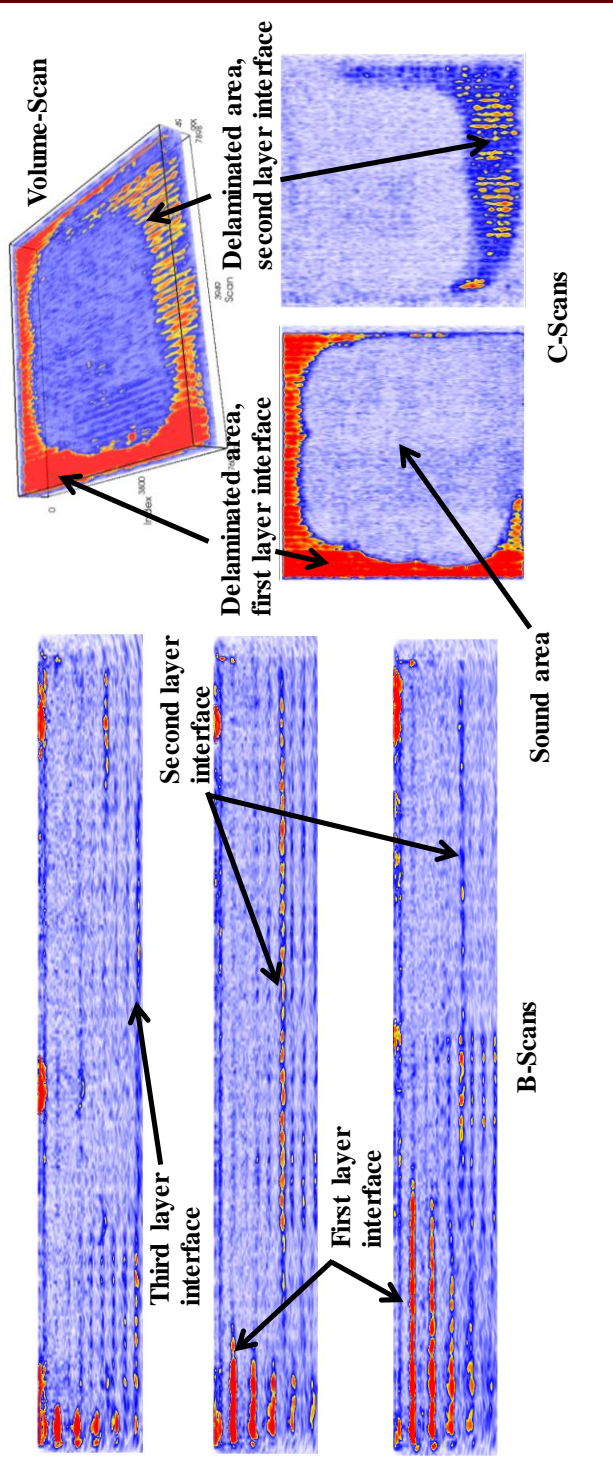
## George Bush International Airport, Houston, TX



Defects	Notes	Backsurface	Reinf. Detail	V <sub>shear</sub> = 2885 m/s X-step: 200 mm Y-step: 100 mm Max Depth: 1000 mm Frequency: 50 kHz Houston, TX IAH IAH 6.13-2 Sta 82+75 T/W W A E TAMU/TTI 6/2011
Significant debonding at at runway/subbase (7.1" deep), verified by coring. Possible further debonding in deeper layers (25.6" and 37.5" deep).	Area tested because of surface cracking, hammer sounding revealing possible delaminations. Image is of typical runway segment.	Top layer of pavement approximately 7.1" below surface, second layer 25.6" below surface, third layer 37.5" below surface.	None	



Defects	Notes	Backsurface	Reinf. Detail	V <sub>shear</sub> = 2885 m/s X-step: 200 mm Y-step: 100 mm Max Depth: 1000 mm Frequency: 50 kHz
Significant debonding at at runway/subbase (7.1" deep), verified by coring. Possible further debonding in deeper layers (25.6" and 37.5" deep).	Area tested because of surface cracking, hammer sounding revealing possible delaminations.	Top layer of pavement approximately 7.1" below surface, second layer 25.6" below surface, third layer 37.5" below surface.	None	Houston, TX IAH IAH 6.13-2 Sta 82+75 T/W W A E TAMU/TTI 6/2011



## VITA

Name: Joshua Benjamin White

Address: Zachry Department of Civil Engineering, Texas A&M University  
3136 TAMU, College Station, TX 77843, USA

Email Address: [joshwhite@tamu.edu](mailto:joshwhite@tamu.edu)

Education: B.S., Physics, Abilene Christian University, 2008  
M.S., Civil Engineering, Texas A&M University, 2012